THERMOELECTRIC PROPERTIES OF MAGNESIUM SILICIDE-STANNIDE SOLID SOLUTION OF VARIOUS PHASE STRUCTURES

A Dissertation

by

SUIN YI

Submitted to the Office of Graduate and Professional Studies of
Texas A&M University
in partial fulfillment of the requirements for the degree of

DOCTOR OF PHILOSOPHY

Chair of Committee,	Choongho Yu
Committee Members,	Raymundo Arróyave
	Tahir Çağin
	Haiyan Wang
Head of Department,	Andreas A. Polycarpou

December 2017

Major Subject: Mechanical Engineering

ABSTRACT

The thermoelectric properties of $Mg_2Sn_xSi_{1-x}$ solid solution with varying phase structure were investigated. Through the modeling of lattice thermal conductivity poor degree of mixing between Sn and Si with segregated phases as much as 60 % of the entire volume was deduced for the samples prepared by non-fully optimized solid state reaction. As per the proposed direction from the modeling, samples with better phase homogeneity were pursued. With the aid of successful sample preparation by high energy ball milling for heavily doped Mg_2Sn and Mg_2Si whose carrier concentrations are over 10^{20} cm^{-3} systematic studies with Sn:Si ratios from 3:7 to 7:3 were conducted for exploring the thermodynamic evolution of the constituent phases by various duration of annealing from 0 to 50 hours. Although the phase segregation into Sn-rich and Si-rich phases was observed after longer annealing, the lattice thermal conductivity was maintained as low as that of the idealized solid solution structure. Lastly the existence of the convergence between two valleys in conduction band at the certain Sn:Si ratio (~7:3) was demonstrated by controlling the degree of mixing. The maximum power factor was enhanced from 3.4 $mW/m\text{-}K^2$ to 4.3 $mW/m\text{-}K^2$ as the degree of mixing was improved. It was also found that the valley convergence accompanies the effective mass broadening so as to offset the improvement in power factor due to doubled number of valleys. The simulated effective mass enhancement by two-parabolic valley model demonstrated the strictly narrow range for Sn:Si ratio to obtain the effective convergence, suggesting the importance of best degree of mixing and phase homogeneity.

DEDICATION

This dissertation is dedicated to Jesus Christ, Heavenly Father, and my beloved and supportive wife, Yoohwa Cho, my adorable daughter, Joanna, and little son, Shiny, for their endless encouragement, unconditional trust, and true love.

ACKNOWLEDGEMENTS

First, I would like to sincerely thank my advisor, Prof. Choongho Yu, for his patient guidance, support, advice and inspiration to the thermoelectric research covering the wide range of aspects throughout my Ph.D. course. Prof. Yu's enthusiasm and commitment to the research is what I would like to carry on in my future career. I also truly appreciate the help and suggestions from my committee members, Prof. Raymundo Arróyave, Prof. Tahir Çağin, and Prof. Haiyan Wang.

Also, I appreciate the members of Nano Energy Lab, Woongchul, Suk Lae, Sangwon, Kyungwho, Jui-Hung, Gang, Jian, Abdullah, Liang, Xiong, and Hong for their friendship and support.

I would like to present my deep gratitude to my parents, Youngsaeng and Sunhui, for their numerous supports and sacrifices. Words cannot express how grateful I am for the love and trust they have shown me.

CONTRIBUTORS AND FUNDING SOURCES

Contributors

This work was supervised by a dissertation committee consisting of Professor Choongho Yu, Professor Raymundo Arróyave of the Department of Mechanical Engineering, Professor Tahir Çağin of the Department of Materials Science and Engineering, and Professor Haiyan Wang of the Department of Materials Engineering in Purdue University.

The experimental works in Chapter III were conducted by Abdullah Tazebay of the Department of Mechanical Engineering and were published in 2016.

All other work conducted for the dissertation was completed by the student, under the advisement of Professor Choongho Yu of the Department of Mechanical Engineering.

Funding Sources

This work was made possible by the financial support from the U.S. Air Force Office of Scientific Research (Grant No. FA9550-13-1-0085) under the auspices of Dr. Charles Lee, the Pioneer Research Center Program through the National Research Foundation of Korea (Grant No. 2011-0001645) funded by the Ministry of Education, Science and Technology, and the U.S. National Science Foundation (Grant No. CMMI 1030958).

TABLE OF CONTENTS

LIST OF FIGURES

LIST OF TABLES

CHAPTER I

INTRODUCTION*

1.1 Current status of thermoelectric conversion

Thermoelectric (TE) effect, which produces voltage from the temperature difference of a material, is one of the promising research fields in view of the growing necessity in environment-friendly sustainable energy.[1-5] Due to the promise of thermoelectric conversion, there are several companies around the world that manufacture TE modules of various sizes. For example a commercial TE device,[6] of which size is about 1 cm^2, produces about 5 mV when it is attached to human's arm, harvesting body heat as shown in Figure 1a. Alternative arrangement of n-type and p-type semiconductors connected in series electrically and in parallel thermally is the main component of typical TE devices, of which schematic is Figure 1b.[5]

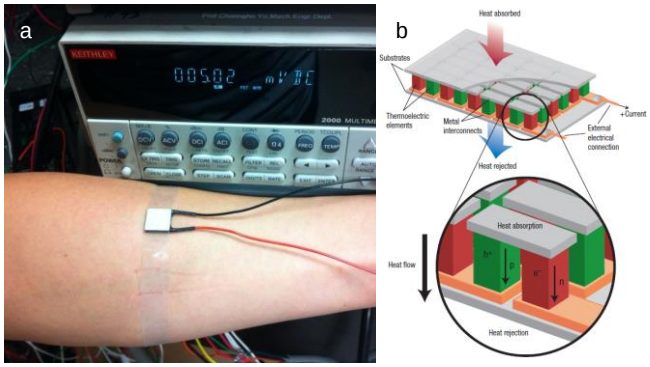

Figure 1. (a) Demonstration of voltage generation from body (arm) heat using thermoelectric device, (b) schematic of thermoelectric device. (reprinted from [5])

*Part of this chapter is reprinted with permission from G. J. Snyder and E. S. Toberer, Complex thermoelectric materials, Nature Materials, 7, 105-114, Copyright 2008 by Nature Publishing Group.

As shown in Figure 2, thermoelectric effect constitutes a consequence of average energy difference in free electrons at hot side and cold side of a material. Due to Fermi-Dirac distribution that rules the energy distribution of Fermions such as electrons, free electrons at hot side have higher energies in average so that voltage, which is the potential energy difference of electron, is generated at two ends. There are various applications which utilize thermoelectric effect such as thermoelectric power generation (space mission, automobile, etc.), Peltier cooling (small scale refrigerator in cars), and sensing purposes (thermocouple). Moreover due to the recent advances in portable electronics with less energy consumption, self-powering of those electronics can be foreseen.

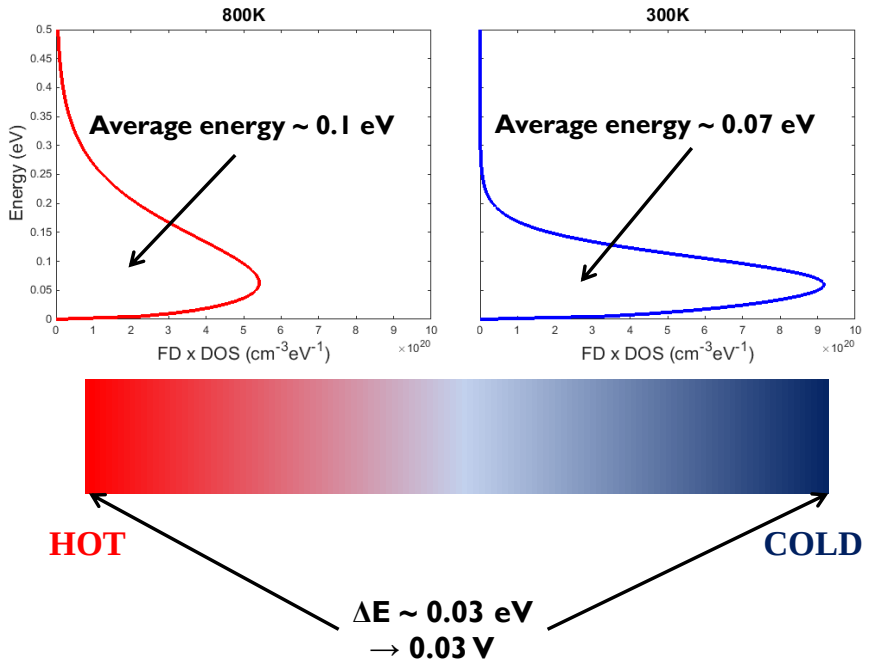

Figure 2. Principle of thermoelectric effect with the exemplary numbers of 800 K at hot side, 300 K at cold side.

Figure 3a demonstrates the amplified voltage of about 45 mV from body heat with sufficiently large copper heat sink to maximize the temperature difference across TE module. Considering the module's resistance, 1.54 Ω,[6] 330 μW per TE device can be obtained with matched load resistance. This corresponds to the generation of 200 mW,[7] which can operate smart phones, with 606 cm^2 in body area schematically represented in Figure 3b. Other personal electronics such as smart watch,[8] and sports band consume less energy,[8] making the thermoelectric energy harvesting from body heat very promising. The advance of thermoelectric conversion efficiency can potentially reduce the required body area to harvest enough thermoelectric energy so that thermoelectric conversion becomes the necessary ingredient for portable electronic devices in the near future.

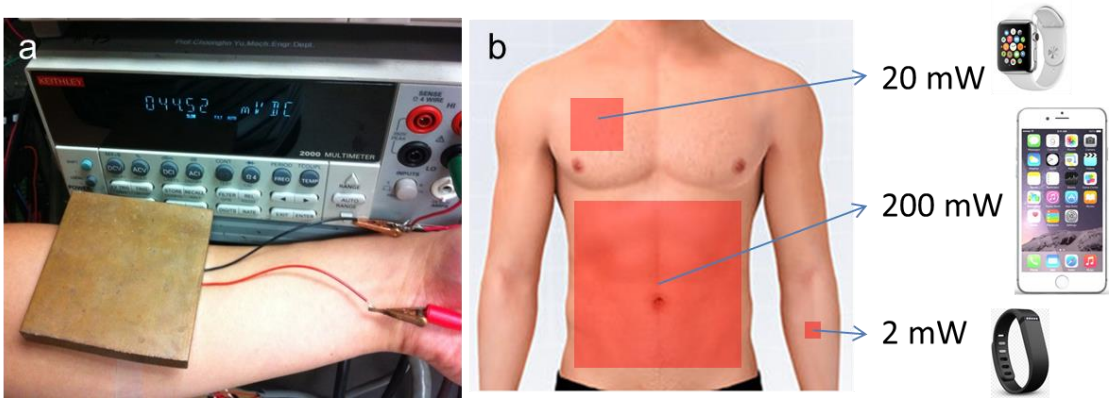

Figure 3. (a) Maximized voltage generation (45 mV) using copper heat sink, (b) required body area through body heat thermoelectric harvesting to operate smart watch, smart phone, and sports band.

1.2 Overview of thermoelectric research

Table 1 shows the hierarchy of thermoelectric research that spans from engineering to scientific aspects with mathematical expressions. The thermoelectric power generation efficiency is a function of ZT, thermoelectric figure of merit, and becomes Carnot efficiency as ZT goes to infinity obeying the laws of thermodynamics. Material's ZT depends on thermopower (voltage per temperature difference of two sides), electrical conductivity, thermal conductivity, and absolute temperature. Most effort was put in improving ZT in the field of thermoelectrics in the recent 20 years as nano-technology emerges. Although Dresselhaus predicted the improvement in thermopower when the material undergoes the quantum confinement effect[9] theoretically in 1993, the concept is yet to be experimentally realized. Rather the most achievement has come from the reduction in thermal conductivity mainly due to nanostructures' phonon scattering mechanism. This is related to the scattering rates by boundaries in nanostructure ($\tau_{boundary}^{-1}$)[10-14] and nanoparticles (τ_{NP}^{-1})[15, 16] rather than material's intrinsic heat capacity or sound velocity in Eq (1.4).

Item		Mathematical representation	
Thermoelectric power generation efficiency (P_{OUT} / P_{IN})	Engineering ↕ Science	$\eta = \left(1 - \frac{T_C}{T_H}\right)\frac{\sqrt{1+ZT}-1}{\sqrt{1+ZT}+T_C/T_H}$ $\eta \rightarrow$ Carnot efficiency w/ ZT=∞	(1.1)
Thermoelectric Figure of Merit		$ZT = \frac{S^2\sigma}{k}T$	(1.2)
Thermal conductivity ($Wm^{-1}K^{-1}$)		$k = k_{ph} + k_{el} + k_{bi}$	(1.3)
Lattice thermal conductivity ($Wm^{-1}K^{-1}$)		$k_{ph} = \frac{1}{3}Cv^2\tau_{ph}$	(1.4)
Phonon relaxation time (s)		$\tau_{ph} = \left(\tau_{Umklapp}^{-1} + \tau_{electron}^{-1} + \tau_{alloy}^{-1} + \tau_{boundary}^{-1} + \tau_{NP}^{-1}\right)^{-1}$	(1.5)

Table 1. Hierarchy of thermoelectric research with mathematical expressions. Where T_C, T_H, S, σ, T, k_{el}, k_{bi}, C, and v are absolute temperature of cold side, absolute temperature of hot side, thermopower (Seebeck coefficient), electrical conductivity, average absolute temperature, electronic thermal conductivity, bipolar thermal conductivity, heat capacity, and sound velocity, respectively.

CHAPTER II

LITERATURE REVIEW*

2.1 Thermal conductivity reduction

Phonon dispersion contains necessary information for material's lattice thermal conductivity such as heat capacity, sound velocity, and anharmonicity, which dominates

*Part of this chapter is reprinted with permission from (a) S.-I. Yi and C. Yu, Modeling of thermoelectric properties of SiGe alloy nanowires and estimation of the best design parameters for high figure-of-merits, Journal of Applied Physics, 117, 035105, Copyright 2015 by AIP Publishing LLC.; (b) A. S. Tazebay, S.-I. Yi, J. K. Lee, H. Kim, J.-H. Bahk, S. L. Kim, S.-D. Park, H. S. Lee, A. Shakouri, and C. Yu, Thermal Transport Driven by Extraneous Nanoparticles and Phase Segregation in Nanostructured Mg2(Si,Sn) and Estimation of Optimum Thermoelectric Performance, ACS Applied Materials & Interfaces, 8, 7003-7012, Copyright 2016 by American Chemical Society.; (c) H. Wang, J.-H. Hsu, S.-I. Yi, S. L. Kim, K. Choi, and C. Yu, Thermally driven large N-type voltage responses from hybrids of carbon nanotubes and poly(3,4-ethylenedioxythiophene) with Tetrakis(dimentylamino)ethylene, Advanced Materials, 27, 6855-6861, Copyright 2015 by John Wiley and Sons.; (d) H. Wang, S.-I. Yi, and C. Yu, Engineering electrical transport at the interface of conjugated carbon structures to improve thermoelectric properties of their composites, Polymer, 97, 487-495, Copyright 2016 by Elsevier.; (e) Y. Pei, X. Shi, A. Lalonde, H. Wang, L. Chen, and G. J. Snyder, Convergence of electronic bands for high performance bulk thermoelectrics, Nature, 473, 66-69, Copyright 2011 by Nature Publishing Group.; (f) Y. Tang, Z. M. Gibbs, L. A. Agapito, G. Li, H.-S. Kim, and M. B. Nardelli, Convergence of multi-valley bands as the electronic origin of high thermoelectric performance in $CoSb_3$ skutterudites, Nature Materials, 14, 1223–1228, Copyright 2015 by Nature Publishing Group.; (g) L.-D. Zhao, G. Tan, S. Hao, J. He, Y. Pei, H. Chi, H. Wang, S. Gong, H. Xu, V. P. Dravid, C. Uher, G. J. Snyder, C. Wolverton, M. G. Kanatzidis, Ultrahigh power factor and thermoelectric performance in hole-doped single-crystal SnSe, Science, 351, 141-144, Copyright 2016 by The American Association for the Advancement of Science.; (h) Y. Pei, A. D. Lalonde, H. Wang, and G. J. Snyder, Low effective mass leading to high thermoelectric performance, Energy & Environmental Science, 5, 7963-7969, Copyright 2012 by Royal Society of Chemistry.; (i) Q. Zhang, L. Cheng, W. Liu, Y. Zheng, X. Su, H. Chi, H. Liu, Y. Yan, X. Tang, and C. Uher, Low effective mass and carrier concentration optimization for high performance p-type $Mg_{2(1-x)}Li_{2x}Si_{0.3}Sn_{0.7}$ solid solutions, Physical Chemistry Chemical Physics, 16, 23576-23583, Copyright 2014 by Royal Society of Chemistry.

intrinsic Umklapp scattering. The eigenvalues of dynamical matrix (*e.g.*, 3-dimensional 2-basis atom system) as shown in Eq. (2.6) at each wave vector constitute the frequencies of the phonon modes, constructing the entire phonon dispersion by discretely mapping the frequency and wave vector in Brillouin zone. Figure 4a shows the phonon dispersion of silicon assuming that only the first neighbor atoms can affect the interatomic potential. The average phonon group velocity in (100) can be calculated from the phonon dispersion as 7800 m/s, which is within 10 % in error compared to typically used values in Boltzmann transport equations (BTE).[12] Figure 4b shows the dependence of phonon dispersion on atom's mass and force constant. The mass and force constant were changed in dynamical matrix calculation by a factor of 2 to describe lighter atom, heavier atom, stronger bonding, and weaker bonding. It can be seen that the frequency, hence the phonon group velocity, is proportional to $(K/m)^{1/2}$, where K and m are force constant and atomic mass. This is the main reason that heavy atoms such as tellurium, lead, and bismuth, of which atomic numbers are 52, 82, and 83, respectively, are main constituent for low sound velocity materials. Also heavy atoms typically have longer bond length so that the number of atoms per volume tends to be small, resulting in low heat capacity as well. Due to this intrinsic characteristics of heavy atom materials Bi_2Te_3 or PbTe have been of the main interest in the field of thermoelectrics and progress to further decrease the thermal conductivity by phonon scattering from extrinsic source has been made by researchers.[11,15]

$$\begin{bmatrix} D_{11,xx} & D_{11,xy} & D_{11,xz} & D_{21,xx} & D_{21,xy} & D_{21,xz} \\ D_{11,yx} & D_{11,yy} & D_{11,yz} & D_{21,yx} & D_{21,yy} & D_{21,yz} \\ D_{11,zx} & D_{11,zy} & D_{11,zz} & D_{21,zx} & D_{21,zy} & D_{21,zz} \\ D_{21,xx} & D_{21,xy} & D_{21,xz} & D_{22,xx} & D_{22,xy} & D_{22,xz} \\ D_{21,yx} & D_{21,yy} & D_{21,yz} & D_{22,yx} & D_{22,yy} & D_{22,yz} \\ D_{21,zx} & D_{21,zy} & D_{21,zz} & D_{22,zx} & D_{22,zy} & D_{22,zz} \end{bmatrix} \quad \text{where } D_{ij,kl} = \frac{\sum_{\vec{c}} K_{ijkl\vec{c}} e^{i\vec{k}\cdot\vec{c}}}{\sqrt{m_i m_j}} \tag{2.6}$$

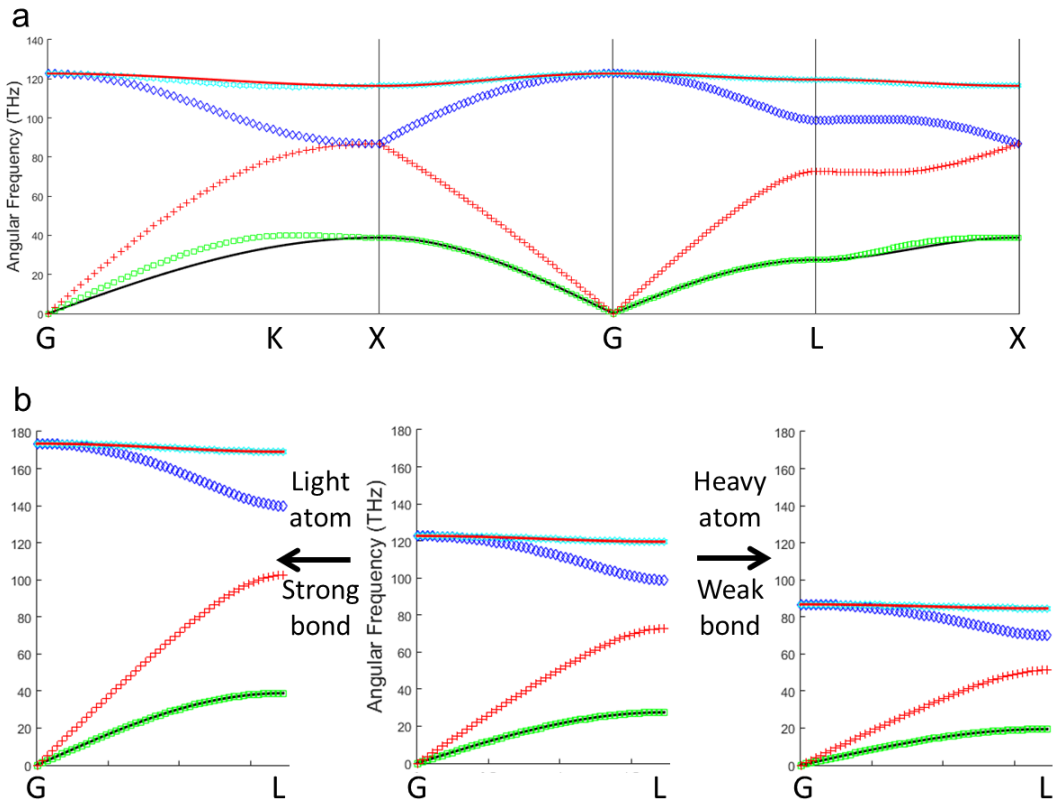

Figure 4. (a) Calculated phonon dispersion of silicon, (b) change in phonon dispersion with artificially changed atomic mass (m) or bonding strength (K).

2.1.1 Theoretical work

2.1.1.1 Boltzmann transport equation for lattice thermal conductivity

To model the experimentally observed thermal conductivities of various materials in our group lattice thermal conductivity was calculated using Boltzmann transport equation. As shown in Eq. (2.7) the lattice thermal conductivity is the integration of differential lattice thermal conductivity from 0 to ω_C in phonon frequency. Phonon energy, phonon density of states, temperature derivative of Bose-Einstein distribution, sound velocity, and scattering relaxation time, denoted as $\hbar\omega$, $D(\omega)$, df_{BE}/dT, v, and $\tau_{ph}(\omega)$, respectively in Eq. (2.8) are the building units of differential lattice thermal conductivity. Eq. (2.9) can be obtained after changing the variable from ω, to reduced energy x. In my calculations Eq. (2.10), Callaway model,[16,17] was used instead, which contains a corrective additional term, I_2^2/I_3.

$$k_{ph} = \int_0^{\omega_D} k_d(\omega) d\omega \tag{2.7}$$

$$k_d(\omega) = \frac{1}{3}\hbar\omega \times D(\omega) \times \frac{df_{BE}}{dT} \times v^2 \times \tau_{ph}(\omega) \tag{2.8}$$

$$k_{ph} = \frac{k_B^4 T^3}{2\pi^2 \hbar^3}\left(\frac{1}{v}\right)\int_0^{\theta_D/T} \tau_{ph}(x) \frac{x^4 e^x}{(e^x - 1)^2} dx \tag{2.9}$$

$$k_{ph} = \frac{k_B^4 T^3}{2\pi^2 \hbar^3}\left(\frac{1}{v}\right)\left(I_1 + \frac{I_2^{\,2}}{I_3}\right) \tag{2.10}$$

2.1.1.2 Thermal conductivity modeling in polycrystalline bulk $Mg_2Si_{0.4}Sn_{0.6}$ pellets[18]

In our group $Mg_2Si_{0.4}Sn_{0.6}$ solid solution thermoelectric material was synthesized and thermoelectric properties as a function of temperature were measured. Figure 5a

shows the thermal conductivity with different amount of TiO_2 nanoparticles which introduce additional scattering events to lower the lattice thermal conductivity. The thermal conductivity of the sample with 5% TiO_2 nanoparticle showed about 20% reduction in thermal conductivity mainly from the lattice portion. In my BTE model the thermal conductivity of various samples were successfully fitted with equivalent scattering relaxation time by Matthiessen's rule, as shown in Eq. (2.11), and introducing the scattering relaxation time τ_{NP}, which is a function of nanoparticles' concentration as denoted in Eq. (2.12).

$$\tau_{ph} = \left(\tau_{Umklapp}^{-1} + \tau_{alloy}^{-1} + \tau_{electron}^{-1} + \tau_{boundary}^{-1} + \tau_{NP}^{-1}\right)^{-1} \tag{2.11}$$

where $\tau_{Umklapp}$, τ_{alloy}, $\tau_{electron}$, $\tau_{boundary}$, and τ_{NP} denote scattering relaxation time of Umklapp process, randomly located alloy, free electron, grain boundary, and nanoparticles, respectively.

$$\tau_{NP} = \frac{2D_{NP}^4\omega^4 + 32v^4}{\pi v N_{NP} D_{NP}^6 \omega^4} \tag{2.12}$$

where ω, D_{NP}, and N_{NP} represent phonon frequency, average diameter of nanoparticles, and concentration of nanoparticles, respectively.

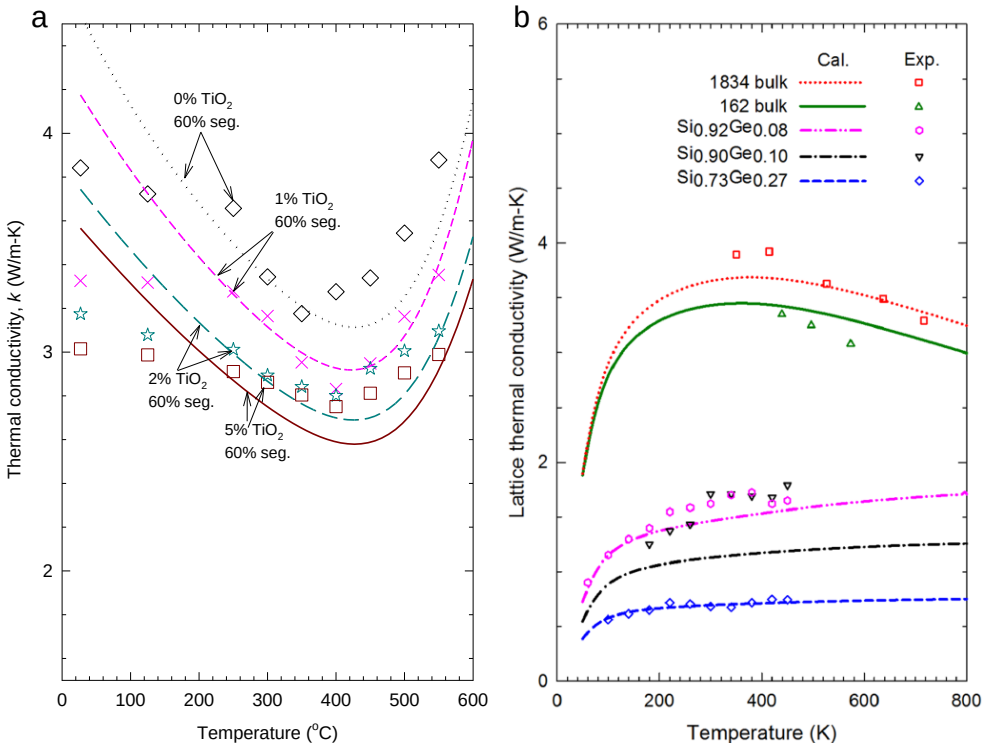

Figure 5. Experimentally measured (symbols) and calculated (lines) thermal conductivities of (a) polycrystalline bulk $Mg_2Si_{0.4}Sn_{0.6}$,[18] and (b) $Si_{1-x}Ge_x$ nanowire.[12,19] (reprinted from [12] and [18])

2.1.1.3 Thermal conductivity modeling in $Si_{1-x}Ge_x$ alloy nanowires[12]

$Si_{1-x}Ge_x$ nanowires, which showed significant reduction in thermal conductivity, were also investigated for thermoelectric applications in our group. Figure 5b shows the lattice thermal conductivity of nanowires compared to that of SiGe bulk samples. $Si_{0.73}Ge_{0.27}$ nanowire with the smallest diameter (26 nm) showed the lowest thermal conductivity, 5 times lower than that of bulk sample. In this calculation Eq. (2.13) was used to describe the phonon scattering at nanowire boundaries.

$$\tau_{boundary} = \frac{d}{v}\left(\frac{1+\alpha}{1-\alpha}\right) \tag{2.13}$$

where d is the diameter of nanowire and α is specularity parameter, respectively.

2.1.2. Experimental work

The characterization of material's thermoelectric properties is not trivial procedure, especially for thermal conductivity because of heat radiation inevitable during the measurement. These days, for this reason, laser flash methods are frequently employed rather than the conventional method, which is vulnerable to errors due to radiation. Nevertheless various nano-materials, which are of interest due to additional scattering or carrier confinement effect, such as polymer thin film or nanowires still have difficulties to be characterized due to their small sizes. Following is the thermal conductivity measurement technique using microdevice, which had been used for measuring thermal conductivity of aforementioned $Si_{1-x}Ge_x$ nanowires,[19] and thermoelectric polymer thin films.[20,21] Figure 6a shows the schematic of thermal conductivity measurement apparatus using microdevice. A sample is to be placed such that it bridges two suspended silicon nitrate membranes, on which serpentine platinum patterns are deposited. The platinum pattern plays a role of Joule heater to produce a heat flow through the sample as well as a role of thermometer utilizing linearly increasing resistivity of platinum as temperature increases. Through the obtained temperature gradient and flowing heat the thermal conductance, hence the thermal conductivity can be calculated. Figure 6b demonstrates the measured thermal conductivity of our thermoelectric composite thin film, which consists of Poly-ethylenedioxythiophene (PEDOT) and carbon nanotube (CNT). Although 10% of CNT was added it was found that the thermal conductivity was negligibly affected so that it

remains below 0.7 W/m-K resulting in anomalously high ZT about 0.5, the best value for the organic thermoelectric material ever reported.

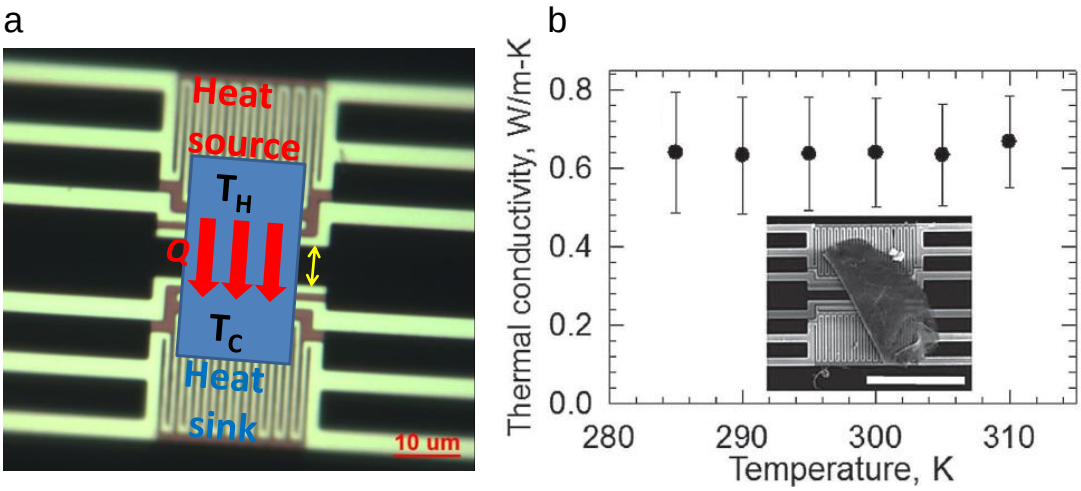

Figure 6. (a) Schematic of thermal conductivity measurement of nano-materials using microdevice, (b) measured thermal conductivity of PEDOT-CNT composite.[20] (reprinted from [20])

2.2 Electrical property improvement

As described so far most effort in improving ZT has been made through thermal conductivity reduction. However as lattice thermal conductivity converges to amorphous limit like most polymers, it is necessary to enhance electrical properties as well especially for organic thermoelectric materials, which already have low thermal conductivity. In this sense it is important to understand the charge transport mechanism first, through the modeling of electrical properties using BTE analogous to lattice thermal conductivity modeling as shown in Eq. (2.14), (2.15), and (2.16).

$$\sigma = \int \sigma_d(E) dE \tag{2.14}$$

$$S = \int \frac{\sigma_d(E)}{\sigma}\left(\frac{E-\mu}{eT}\right)dE \tag{2.15}$$

$$\sigma_d(E) = \frac{1}{3}e^2 \times D(E) \times \left(-\frac{df}{dE}\right) \times \{v(E)\}^2 \times \tau(E) \tag{2.16}$$

where e, $D(E)$, df/dE, $v(E)$, $\tau(E)$, and μ are electron charge, electron density of states, energy derivative of Fermi-Dirac distribution, free electron's velocity, electron scattering relaxation time, and chemical potential, respectively.[12,18,22]

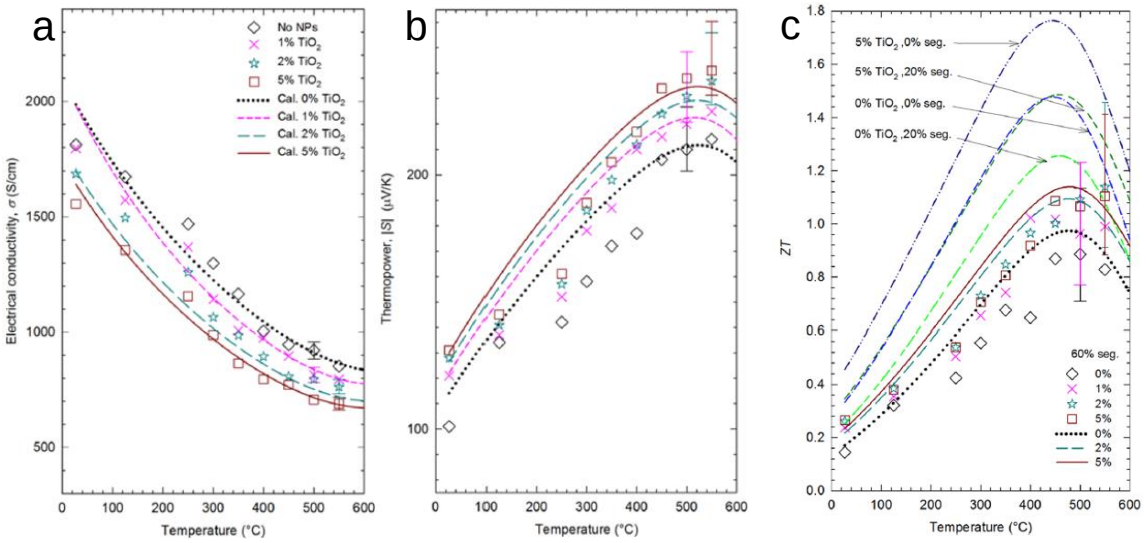

Figure 7. (a) Experimentally measured (symbols) and calculated (lines) (a) electrical conductivities, (b) thermopower, and (c) thermoelectric figure of merit of polycrystalline bulk $Mg_2Si_{0.4}Sn_{0.6}$ pellets.[18] (reprinted from [18])

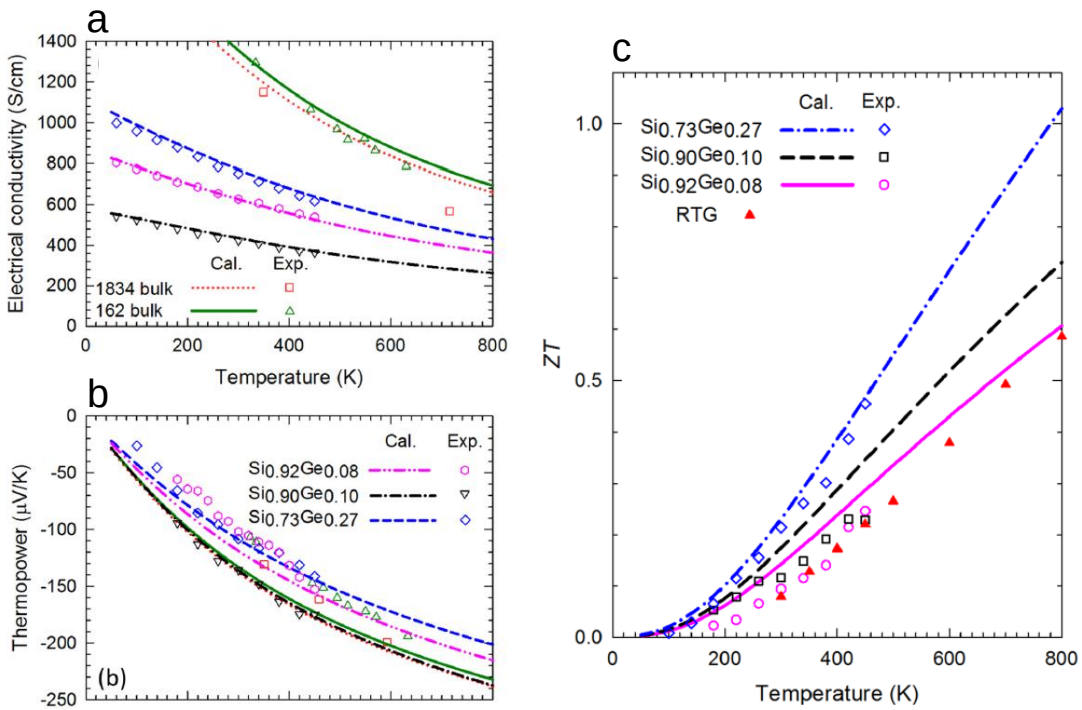

Figure 8. (a) Experimentally measured (symbols) and calculated (lines) (a) electrical conductivities, (b) thermopower, and (c) thermoelectric figure of merit of $Si_{1-x}Ge_x$ nanowires.[12] (reprinted from [12])

The experimentally measured electrical conductivity and thermopower of $Mg_2Si_{0.4}Sn_{0.6}$ were successfully fitted using the model as shown in Figure 7a and 7b. Also ZT was fitted in good agreement with experimental data (Figure 7c). Using the model even higher ZT was proposed when phase segregation is reduced. Figure 8a and 8b also show the calculation results of electrical conductivity, thermopower, and ZT (Figure 8c) of $Si_{1-x}Ge_x$ nanowire in good agreement with experimental measurement.

In recent several years researchers started focusing on electrical properties mainly in two ways: i) increase thermopower through high valley degeneracy, and ii) increase the mobility of carriers by reducing the effective mass. With the assumption of

acoustic phonon dominated scattering the thermoelectric power factor $S^2\sigma$ can be simplified to Eq. (2.17).

$$S\sigma^2 = \left[\frac{S^2 e^2 \hbar C_l}{\pi k_B T D_a^2} \int f(E) dE \right] \frac{N_V}{m^*} \tag{2.17}$$

where C_l, k_B, D_a, N_V, and m^* are elastic constant, Boltzmann constant, deformation potential, valley degeneracy, and effective mass of carrier, respectively. The term in bracket is constant as long as the chemical potential is kept constant. Therefore thermoelectric power factor is concluded to be proportional to N_V and inversely proportional to m^*.

2.2.1 Valley degeneracy

Three figures in the bottom of Figure 9 show the nature of multiple valleys in good thermoelectric materials such as lead telluride, skutterudite, and tin selenide. Due to the multiple valleys (large N_V), the thermopower can be elevated with fixed carrier concentration while preserving the carrier mobility as long as intervalley scattering is negligible.[23] As a result power factor proportionally increases with N_V, consistent to mathematical derivation in Eq. (2.17).

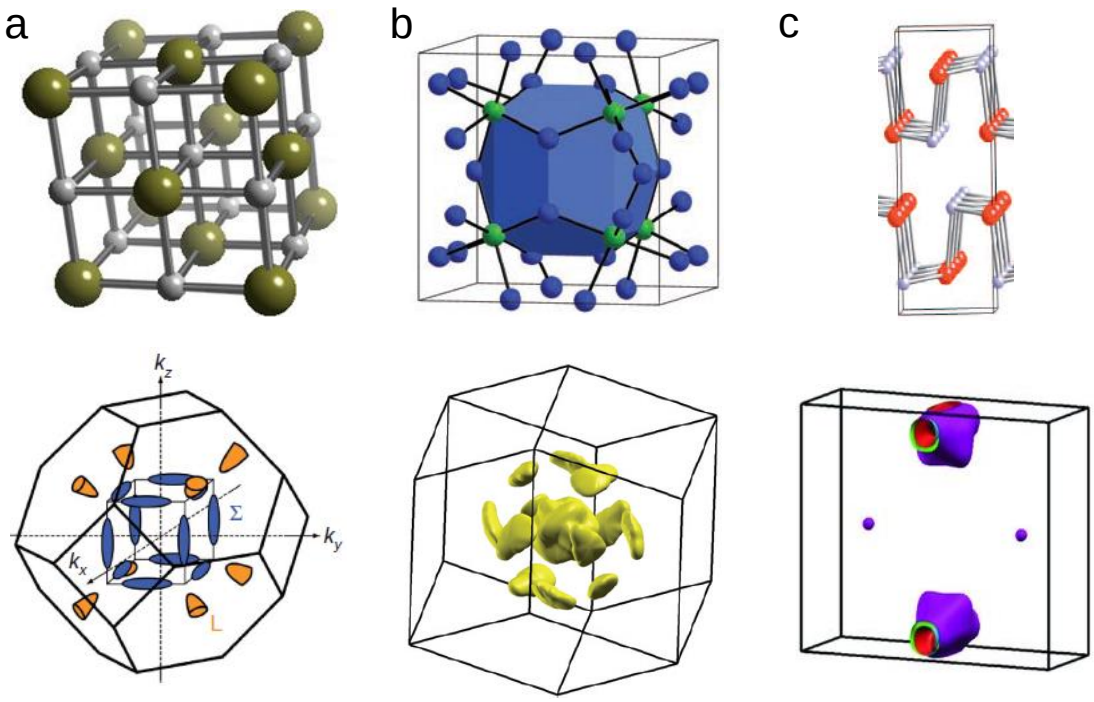

Figure 9. Crystal structure (top) and Brillouin zone (bottom) together with the representation of multiply valleys of (a) lead telluride (PbTe),[23] (b) skutterudie ($CoSb_3$),[24] and (c) tin selenide (SnSe).[25] (reprinted from [23], [24], and [25])

2.2.2 Mobility by lower effective mass

Figure 10a shows the examples of improved mobility by reducing carrier's effective mass through different dopants. In n-type PbTe, iodine doped samples resulted in higher mobility than that of lanthanum doped samples.[26] The analogous demonstration in p-type material was recently made in lithium doped $Mg_2Si_{0.3}Sn_{0.7}$ solid solution samples.[27] (Figure 10b) As a result power factor proportionally increased with $1/m^*$, consistent to mathematical derivation in Eq. (2.17).

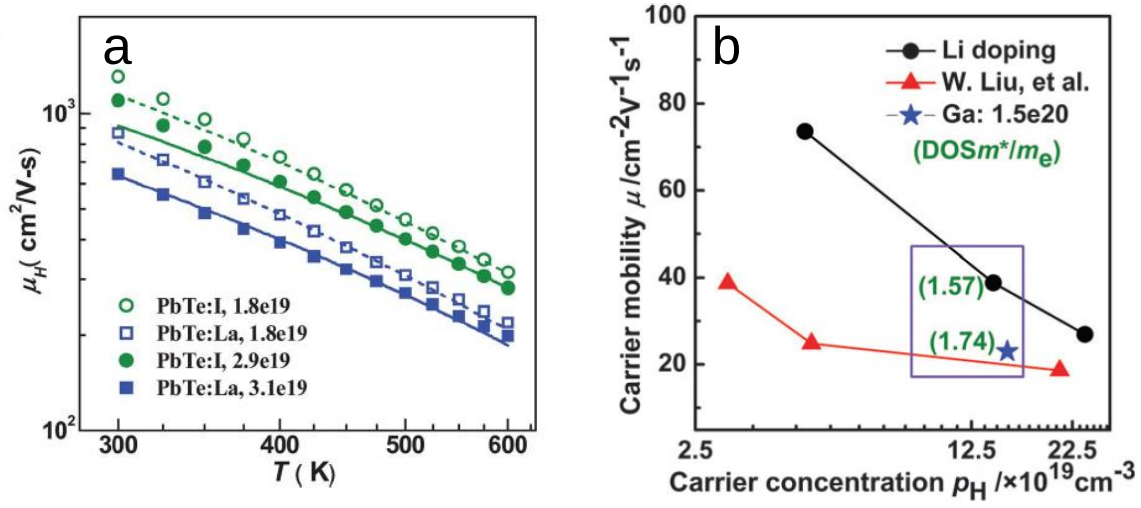

Figure 10. Improved carrier mobility with different dopants in (a) n-type PbTe,[26] and (b) p-type $Mg_2Si_{0.3}Sn_{0.7}$.[27] (reprinted from [26] and [27])

2.2.3 Energy filtering

In our group the main focus to improve the electrical properties has been implemented through junctions among different materials in heterogeneous composites, mainly conducting polymer and CNT.[22] Figure 11a shows the experimental results in our composite sample composed of polyanline (PANI) and CNT. It should be noted that the electrical conductivity enhancement is tremendous (700%) with the cost of 10% sacrifice in thermopower. As a result the enhancement power factor turned out to be 600%. Through the implementation of energy barrier between PANI and CNT combined with BTE model, the enhancement in thermopower with marginal sacrifice in electrical conductivity was simulated. The average energy of free carrier in PANIeb became 28.3 meV higher than that of pure CNT film, noted as "No barrier" in the Figure 11b. As a result thermopower increased to 124 μV/K from 30 μV/K (Figure 11c) of pure CNT film

since thermopower is defined as carriers' average energy divided by electron charge and temperature, described in Eq. (2.15).

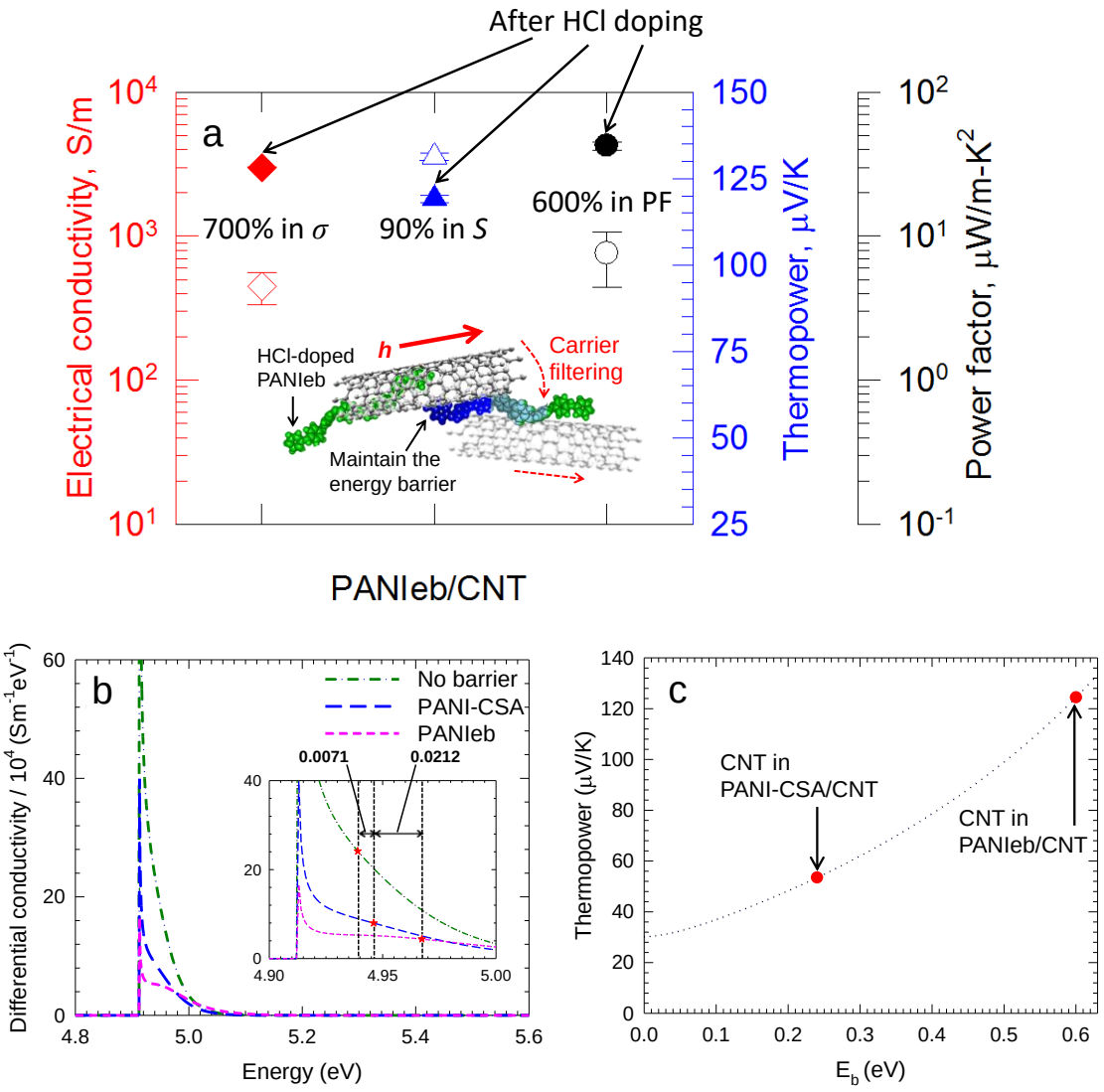

Figure 11. (a) Electrical conductivity, thermopower, and power factor of PANIeb/CNT composite before (hollow symbols) and after (filled symbols) HCl doping, (b) calculated differential conductivity as a function of carrier energy for CNT networks with no barrier, PANI-CSA, and PANIeb at junctions, (c) calculated thermopower enhancement as a function of barrier height (E_b).[22] (reprinted from [22])

2.2.4 Charge carrier conduit

Another methodology employed in our group is utilizing CNT as high mobility conduit so that mobility of sample can be significantly increased. The schematic of our polymer (PEDOT) + CNT composite film and the carrier injection from PEDOT to CNT due to band edge difference is shown in Figure 12a.[21] As a result a huge power factor, ~1000 $\mu Wm^{-1}K^{-2}$ (Figure 12b) which never has been achieved in polymer thermoelectric material was measured.[20]

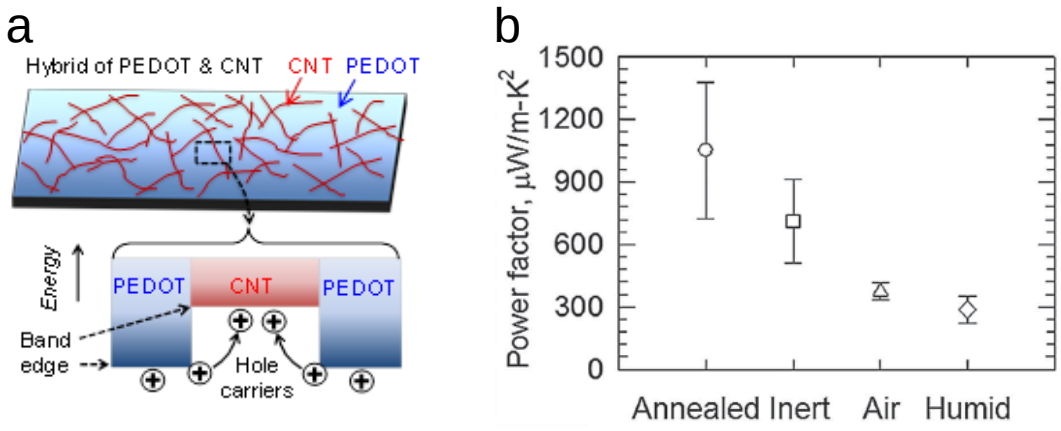

Figure 12. (a) Schematic of PEDOT-CNT composite thin film and carrier injection from PEDOT to CNT,[21] (b) power factor in PEDOT-CNT composite with different post treatment conditions.[20] (reprinted from [20])

CHAPTER III

THERMAL TRANSPORT DRIVEN BY PHASE SEGREGATION IN NANOSTRUCTURED $Mg_2(Si,Sn)$ AND ESTIMATION OF OPTIMUM THERMOELECTRIC PERFORMANCE[*]

3.1 Introduction

Recent intense demand for sustainable and environmentally-friendly energy usage has driven significant efforts to develop new techniques for improving energy utilization. A substantial amount of energy extracted from energy sources is rejected from energy-consuming systems to the environment due to the inefficiency of the systems.[28] Considering popular energy-consuming systems have been optimized over many years, the recovery of wasted energy could be a viable option to improve their overall performance. Over the last decade, thermoelectric energy conversion has attracted considerable interest due to the significant performance enhancement of thermoelectric materials.[29]

In particular, thermoelectric materials whose optimum operating temperatures are 300~500 °C have many application areas such as exhaust manifolds of automobiles[29] since this grade of energy, despite relatively large exergy, is not readily usable in many conventional systems such as turbines. For the intermediate temperatures, $Mg_2(Si,Sn)$

[*] Reprinted with permission from A. S. Tazebay, S.-I. Yi, J. K. Lee, H. Kim, J.-H. Bahk, S. L. Kim, S.-D. Park, H. S. Lee, A. Shakouri, and C. Yu, Thermal Transport Driven by Extraneous Nanoparticles and Phase Segregation in Nanostructured Mg2(Si,Sn) and Estimation of Optimum Thermoelectric Performance, ACS Applied Materials & Interfaces, 8, 7003-7012, Copyright 2016 by American Chemical Society.

solid solutions are one of the best candidates owing to non-toxic inexpensive low-density raw materials with relatively high performance.[30-42]

Thermoelectric performance is often indicated by the thermoelectric figure-of-merit (*ZT*):

$$ZT = \frac{S^2\sigma}{k_e + k_l + k_{bi}}T \tag{3.1}$$

where S, σ, k_e, k_l and, k_l are thermopower (or the Seebeck coefficient), electrical conductivity, electronic thermal conductivity, lattice thermal conductivity, and bipolar thermal conductivity respectively. It has been proven that suppression of lattice thermal conductivity is very effective in increasing *ZT*.[19,32,33,39,42-44] It has been found that the thermal conductivity values of $Mg_2(Si,Sn)$ reported so far are still higher than those of other state-of-the-art thermoelectric materials, which may leave room for further improvement by suppressing thermal conductivity. Therefore the most promising near-term strategy would be to identify how to effectively reduce thermal conductivity of $Mg_2(Si,Sn)$. In literature, both the temperature-dependent behavior of thermal conductivity and the lowest thermal conductivity values reported are quite spread, but *ZT* values much higher than 1 were found unanimously from the papers reporting low thermal conductivity.

However, it is still unclear why the thermal conductivity of the high *ZT* samples is so low although the material is composed of relatively light elements. There have been quite a few papers[33,36,38,45] reporting segregated Mg_2Si and Mg_2Sn phases, and some of them[33,36,38] "conjectured" phase segregation caused the low lattice thermal conductivity

as a result of additional phonon scattering. Although the extent of miscibility gap is different depending on literature,[46,47] phase segregation for $Mg_2Si_xSn_{1-x}$ is inevitable in the range of $0.4<x<0.6$, and the segregation may significantly vary depending on synthesis conditions such as sintering temperature and time.[46] Phase segregation may also come from incomplete diffusion of raw materials considering the short reaction time of typical current-assisted sintering and spark plasma sintering methods. There is consensus that the phase segregation affects lattice thermal conductivity, but it has never been well studied if it has positive or negative influence on thermoelectric performance and the correlation of thermoelectric properties and the amount of segregated phases.

Here we found that the phase segregation "increased" lattice thermal conductivity, in opposition to the previous speculation, as a result of weaker phonon alloy scattering. We incorporated extraneous materials (TiO_2 nanoparticles were chosen due to availability and inertness) into the host $Mg_2(Si,Sn)$ material as a means of further reducing the lattice thermal conductivity. According to our experimental results, addition of 1, 2, and 5 vol% TiO_2 nanoparticles noticeably reduced both lattice and bipolar thermal conductivity values. We also fitted our experimental results to obtain necessary parameters to predict the upper bound of *ZT* and the optimum conditions.

3.2 Experimental

3.2.1 Material synthesis

We prepared 12 different kinds of solid solutions of magnesium silicide and magnesium stannide with arsenic and antimony dopants and TiO_2 nanoparticles. Table 4 lists atomic ratios of the elements as well as vol% of TiO_2 nanoparticles in the solid solutions. We added 10% excess magnesium to compensate magnesium loss during solid state reactions.[48] An arsenic-doped silicon wafer was used to avoid an additional step to dope silicon. Antimony, which dopes tin more than silicon at our reaction temperatures, was also used to further control the doping level. The expected composition is $Mg_2(Si_{0.4-x}Sn_{0.6})_{1-y}As_xSb_y$ with x=0.008. We started with antimony doping level (y) of 0.015 with eight different TiO_2 nanoparticle concentrations (0, 0.1, 0.2, 0.5, 1, 2, 5, and 10 vol%). Then, to increase thermopower, we reduced Sb doping to 0.0075 along with the high four concentrations of TiO_2 nanoparticles (0, 1, 2, and 5 vol%) since the low concentrations of nanoparticles had negligible influence on thermoelectric properties.

Our samples were synthesized by using a two-step solid state reaction process followed by current-assisted sintering and then a densification process. Magnesium (99.0%, Alfa aesar), arsenic-doped silicon (resistivity < 0.003 ohm-cm, University wafers), tin (99.9%, Alfa aesar), antimony (99.0%, Strem chemicals) with atomic ratios listed in Table S1 were mixed in a planetary ball miller (75-mL container with 3~4 g of raw materials, 15 stainless steel balls whose diameter is 6 mm, ~30 rpm for 24 h. The mixed powder was transferred to a graphite container that was encapsulated by a sealed

stainless steel container. The above processes were carried out in a glove box (O_2 < 0.1 ppm and H_2O < 0.1 ppm) to prevent oxidation of the raw powder.

The first solid state reaction was performed by increasing temperature of the container to 550 °C with a ramping rate of ~6 °C/min and maintaining the temperature for 16 h, and then naturally cooling it down to room temperature. The cooling rate was as high as 10 °C/min at temperatures above 200 °C, and decreased to 1°C/min or lower below 200 °C. The resultant product was ground by using an agate mortar and pestle, and then the powder was cold-pressed at 400 MPa (Carver laboratory press) into a 0.5-inch diameter disk. The second solid state reaction was carried out with the disk sample in a sealed graphite-lined container at 700 °C for 4 h with 8 °C/min ramping.

The disk sample was again ground with the mortar and pestle in the glove box. The powder (3~4 g) was further pulverized for homogenization and wide size distributions with 3 stainless steel balls (0.25-inch diameter) in a high energy ball miller (inner diameter and length of the cylindrical container are 1.5 inch and 3 inch, respectively) at 1200 rpm for 30 min. The powder was mixed with TiO_2 nanoparticles (anatase, 5 nm in nominal diameter, Alfa Aesar, see Table 2 for vol%) by the mortar and pestle, and then the mixture was loaded into a graphite die (0.5-inch inner diameter and 1.5-inch outer diameter). Finally the sample was sintered by passing current (maximum 900~1100 A) for 5 min to reach a maximum temperature of ~650 °C (3~4 min out of total 5 min) at 70 MPa, and then an additional densification process at 700 °C for 2 h with a slow temperature ramping (2 h) was carried out in a sealed graphite-lined container. Samples had 95% of the theoretical density or higher.

Table 2. Parameters used for the calculations. Ionized impurity concentration (N_{II}), non-ionized impurity concentration (N_{NI}), electron deformation potential (D_a), hole deformation potential (D_{ah}), ratio of segregated volume to total volume (f, 0~1), specularity parameter (α) corresponding to the boundary scattering, and a multiplication factor (β) in bipolar thermal conductivity to account for additional scattering of the minority carriers (holes). Majority carrier (electron) concentrations by Hall measurements were also listed next to the theoretically obtained N_{II} for easy comparison. (reprinted from [18])

Sample #	TiO_2 (vol%)	N_{II} (10^{20} cm^{-3})	Hall carrier concentration (10^{20} cm^{-3})	N_{NI} (10^{18} cm^{-3})	D_a (eV)	D_{ah} (eV)	f	α	β
1	0	1.8	1.62	1.0	7	1	0.6	0.65	1
2	1	1.5	1.67	0.5				0.60	0.8
3	2	1.4	1.51	0.8				0.55	0.6
4	5	1.3	1.40	0.7				0.50	0.5

3.2.2 Thermoelectric property characterization

The thermal diffusivity of the disk samples (typically 0.5 inch in diameter and 0.75~1.1 mm in thickness) was measured by using a flash apparatus (Flashline3000, TA Instrument) at 27~550 °C. We repeated the experiments for some of the samples, but noticeable hysteresis was not identified (less than ~4% differences), indicating negligible densification or material losses during the temperature cycle. Thermal conductivity (k) was calculated from the formula, $k = c\rho\alpha$, where c, ρ, and α are specific heat, mass density, and thermal diffusivity, respectively. Temperature-dependent specific heat data was obtained from Liu *et al.*,[33] and the density was obtained by measuring volume and

mass. The disk sample was cut into a rectangular shape (typically 5 mm × 12 mm) by using a diamond saw for electrical property measurements. Electrical conductivity and thermopower were measured by using a custom-built setup from room temperature to 550 °C. Electrical resistance was sought from the slope of a four-probe linear current-voltage sweeping data (~20 data points between –0.1 A and 0.1 A), and electrical conductivity was obtained by multiplying geometrical factors. Thermopower was obtained by taking the slope from the linear relationship of temperature and voltage differences between hot and cold ends.[49] Voltage data was taken at temperature differences ranging from 1 to 10 °C. The majority carrier concentration and Hall mobility data were determined at room temperature under 1-T magnetic field with a van der Pauw sample geometry (typically 8 mm × 8 mm).

3.3 Modeling using Boltzmann transport equation

3.3.1 Electrical conductivity and thermopower calculation

Electron (or majority) carrier concentration (N_e) and hole (or minority) carrier concentration (N_h) can be calculated with the Fermi levels as input parameters:

$$N_e = N_{V,X3}\int_0^\infty \frac{\sqrt{2E}\left(m_{X3}^*\right)^{1.5}/\left(\pi^2\hbar^3\right)}{\exp\left[\left(E-E_{F,X3}\right)/\left(k_BT\right)\right]+1}dE + N_{V,X1}\int_0^\infty \frac{\sqrt{2E}\left(m_{X1}^*\right)^{1.5}/\left(\pi^2\hbar^3\right)}{\exp\left[\left(E-E_{F,X1}\right)/\left(k_BT\right)\right]+1}dE \tag{3.2}$$

$$N_h = N_{V,HH}\int_0^\infty \frac{\sqrt{2E}\left(m_{HH}^*\right)^{1.5}/\left(\pi^2\hbar^3\right)}{\exp\left[\left(E-E_{F,HH}\right)/\left(k_BT\right)\right]+1}dE + N_{V,LH}\int_0^\infty \frac{\sqrt{2E}\left(m_{LH}^*\right)^{1.5}/\left(\pi^2\hbar^3\right)}{\exp\left[\left(E-E_{F,LH}\right)/\left(k_BT\right)\right]+1}dE \tag{3.3}$$

Here we considered two X-valleys in the conduction band (labeled as X1 and X3) and two Γ-valleys in the valence band (labeled as HH, and LH), as shown in Figure 13.[50] Each integral was calculated with respect to the band edge of each valley (*i.e.*, E = 0 at the band edge). For convenience, we used the band edge of X3 valley as a reference, the four valleys can be expressed with the Fermi level (E_F) as:

$$E_{F,X3} = E_F \tag{3.4}$$

$$E_{F,X1} = E_F - E_0 \tag{3.5}$$

$$E_{F,HH} = E_{F,LH} = -\left(E_G + E_F\right) \tag{3.6}$$

where E_0 is the energy offset ($E_{Edge,X1} - E_{Edge,X3}$) and E_G is the band gap as shown in Figure 13.

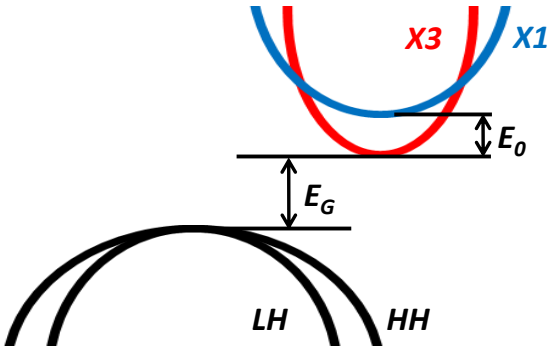

Figure 13. Multi valley schematic of $Mg_2Si_{0.4}Sn_{0.6}$. (reprinted from [18])

Table 3. Detailed parameters used for calculation.[50,51] The atomic concentration of Sn is y. (reprinted from [18])

Parameters	Values
m^*_{X3} (m_0)	0.38
m^*_{X1} (m_0)	$0.49+2.0\times10^{-4}\times T$
m^*_{HH} (m_0)	1.5
m^*_{LH} (m_0)	1.0
E_G (eV)	$(0.78-4.0\times10^{-4}\times T)\times(1-y) + (0.38-2.8\times10^{-4}\times T)\times y$
E_0 (eV)	$(0.4)\times(1-y) + (-0.165)\times y$
ε_0 (F/m)	$(20\times(1-y) + 23.75\times y)\times8.85\times10^{-12}$
ε_∞ (F/m)	$(13.3\times(1-y) + 17\times y)\times8.85\times10^{-12}$
$\hbar\omega_0$ (meV)	$40\times(1-y)+28.8\times y$
ρ_{NP} (g/cm^3)	3.78
d (nm)	11
ρ_M (g/cm^3)	$1.88\times(1-y)+3.59\times y$
D_e (eV)	7
D_h (eV)	1
C_l (N/m^2)	$(4.15\times(1-y)+3.22\times y)\times10^{10}$
$\omega_{C,L}$ (THz)	$52.3\times(1-y)+ 22.4\times y$
$\omega_{C,T}$ (THz)	$29.7\times(1-y)+ 13.9\times y$
v_L (m/s)	$7700\times(1-y)+ 4900\times y$
v_T (m/s)	$4900\times(1-y)+ 3000\times y$
γ	$2.5\times(1-y)+ 1.7\times y$
α for TiO_2 0%, 1%, 2%, 5%	Respectively 0.65, 0.60, 0.55, 0.50
β for TiO_2 0%, 1%, 2%, 5%	Respectively 1, 0.8, 0.6, 0.5
$N_{V,X3}$, $N_{V,X1}$	3
$N_{V,HH}$, $N_{V,LH}$	1

With the effective mass (m^*) in Table 3, N_e and N_h were found, and then ionized impurity concentration (N_{II}) was calculated by:

$$N_{II} = N_e - N_h \tag{3.7}$$

Thermopower (S) can be calculated with electrical conductivity (σ) by:

$$S = \sum_j S_j \frac{\sigma_j}{\sigma} \tag{3.8}$$

$$S_j = \int_0^\infty \frac{\sigma_{d,j}(E)}{\sigma_j}\left(\frac{E - E_{F,j}}{qT}\right)dE \tag{3.9}$$

$$\sigma_{d,j}(E) = q^2 \times D_j(E) \times \left(-\frac{df_j(E)}{dE}\right) \times \tau_j(E) \times \left\{v_j(E)\right\}^2 \tag{3.10}$$

$$D_j(E) = \frac{\sqrt{2}(m_j^*)^{1.5}}{\pi^2\hbar^3}\sqrt{E} \tag{3.11}$$

$$f_j(E) = \frac{1}{\exp\left[\left(E - E_{F,j}\right)/\left(k_B T\right)\right] + 1} \tag{3.12}$$

$$\tau_j(E) = \left(\tau_{AC,j}^{-1}(E) + \tau_{II,j}^{-1}(E) + \tau_{POP,j}^{-1}(E) + \tau_{NI,j}^{-1}(E)\right)^{-1} \tag{3.13}$$

$$v_j(E) = \sqrt{\frac{2E}{3m_j^*}} \tag{3.14}$$

$$\sigma_j = N_{V,j}\int_0^\infty \sigma_{d,j}(E)dE \tag{3.15}$$

$$\sigma = \sum_j \sigma_j \tag{3.16}$$

where q, T, E, m^*, N_V are electron charge, absolute temperature, carrier energy with respect to band edge, carrier effective mass, and valley degeneracy, respectively. The index j indicates valley (X1, X3, HH, and LH). The subscripts *AC*, *POP*, *II*, and *NI* in scattering relaxation time represent acoustic phonon, ionized impurity, polar optical phonon, non-ionized impurity, respectively. The material parameters employed are summarized in Table 3.

The mobility of electron (μ_e) and hole (μ_h) carriers can be obtained by:

$$\mu_e = \frac{\sigma_{X1} + \sigma_{X3}}{qN_e} \tag{3.17}$$

$$\mu_h = \frac{\sigma_{HH} + \sigma_{LH}}{qN_h} \tag{3.18}$$

The mean free path of electronic carrier (l_j) as a function of energy in valley j can be obtained by:

$$l_j = \sqrt{\frac{2E}{m_j^*}} \times \tau_j \tag{3.19}$$

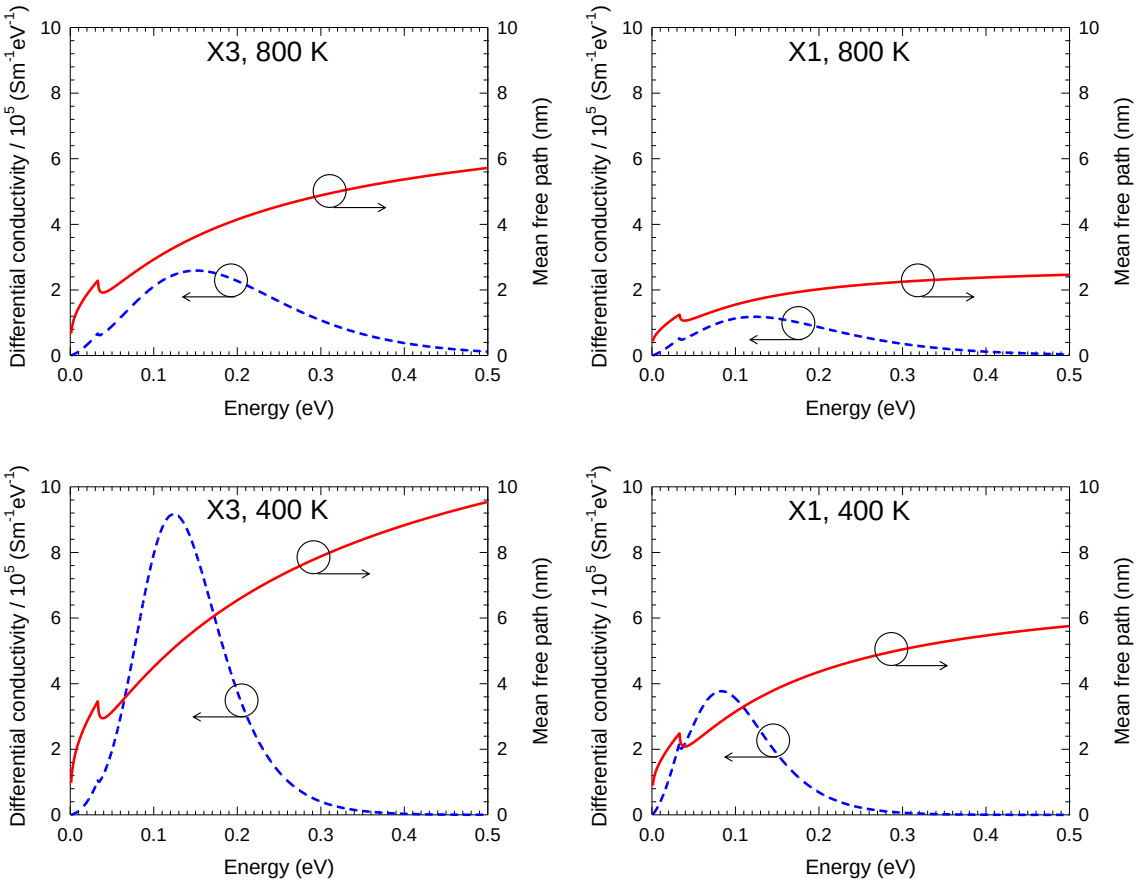

Figure 14. Calculated mean free path of electron carriers in X3 and X1 valley as a function of energy for no TiO_2 nanoparticle sample at 800 K and 400 K using the velocity and relaxation time. (reprinted from [18])

3.3.2 Thermal conductivity calculation

Electronic thermal conductivity (k_e) and bipolar thermal conductivity (k_{bi}) can be calculated by:

$$k_e = \sum_j L_j \sigma_j T \tag{3.20}$$

The Lorenz number is expressed as:

$$L_j = \int_0^\infty \frac{\sigma_{d,j}(E)}{\sigma_j}\left(\frac{E - E_{F,j}}{qT}\right)^2 dE - \left\{\int_0^\infty \frac{\sigma_{d,j}(E)}{\sigma_j}\left(\frac{E - E_{F,j}}{qT}\right)dE\right\}^2 \tag{3.21}$$

$$k_{bi} = \frac{\sigma_e \sigma_h}{\sigma_e + \sigma_h}(S_e - S_h)^2 T \tag{3.22}$$

where

$$\sigma_e = \sigma_{X1} + \sigma_{X3}; \quad \sigma_h = \sigma_{HH} + \sigma_{LH} \tag{3.23}$$

$$S_e = \frac{\sigma_{X1} S_{X1} + \sigma_{X3} S_{X3}}{\sigma_e}; \; S_h = \frac{\sigma_{HH} S_{HH} + \sigma_{LH} S_{LH}}{\sigma_h} \tag{3.24}$$

Lattice thermal conductivity was calculated by using a modified Callaway model that separately considered longitudinal and transverse modes of phonons.

$$k_l = \frac{1}{3}(k_L + 2k_T) \tag{3.25}$$

$$k_i = \frac{k_B^4 T^3}{2\pi^2 \hbar^3}\left(\frac{1}{v_i}\right)\left(I_{i1} + \frac{I_{i2}^{\;2}}{I_{i3}}\right) \tag{3.26}$$

The subscript i stands for either longitudinal mode (L) or transverse mode (T).

$$I_{i1} = \int_0^{\theta_i/T} \tau_{p,i} \frac{x^4 e^x}{(e^x - 1)^2} dx \tag{3.27}$$

$$I_{i2} = \int_0^{\theta_i/T} \frac{\tau_{p,i}}{\tau_{pN,i}} \frac{x^4 e^x}{(e^x - 1)^2} dx \tag{3.28}$$

$$I_{i3} = \int_0^{\theta_i/T} \frac{\tau_{p,i}}{\tau_{pN,i}\tau_{pR,i}} \frac{x^4 e^x}{(e^x - 1)^2} dx \tag{3.29}$$

where $x=\hbar\omega/(k_B T)$ is the reduced energy of phonon and Θ_i is the Debye temperature.

$$\frac{1}{\tau_{p,i}} = \frac{1}{\tau_{pN,i}} + \frac{1}{\tau_{pR,i}} \tag{3.30}$$

The relaxation time corresponding to the normal scattering is described as:[12]

$$(\tau_{pN,L})^{-1} = \frac{k_B^5 \gamma^2 V}{M v_L^5 \hbar^4} x^2 T^5 \tag{3.31}$$

$$(\tau_{pN,T})^{-1} = \frac{k_B^5 \gamma^2 V}{M v_T^5 \hbar^4} x T^5 \tag{3.32}$$

where k_B, γ, V, M, v_L, v_T, $\hbar$ and T are Boltzmann constant, Grüneisen parameter, average volume of an atom, average mass of an atom, longitudinal sound velocity, transverse sound velocity, reduced Planck constant, and absolute temperature, respectively.

Umklapp scattering is expressed as:

$$(\tau_{pU,i})^{-1} = \frac{\hbar\gamma^2}{M v_i^2 \theta_i} \left(\frac{k_B}{\hbar}\right)^2 x^2 T^3 e^{-\theta_i/3T} \tag{3.33}$$

where θ_i is the Debye temperature which is equal to $\hbar\omega_C/k_B$. The scattering due to random alloy between Si and Sn is

$$(\tau_{pA,i})^{-1} = \Gamma \frac{V}{4\pi v_i^3} \left(\frac{k_B T}{\hbar}\right)^4 x^4 \tag{3.34}$$

$$\Gamma = 3\left(\frac{M_{Si,Sn}}{2M_{Mg} + M_{Si,Sn}}\right)^2 \left((1-y)\left(\frac{M_{Si} - M_{Si,Sn}}{M_{Si,Sn}}\right)^2 + y\left(\frac{M_{Sn} - M_{Si,Sn}}{M_{Si,Sn}}\right)^2\right) \tag{3.35}$$

$$M_{Si,Sn} = (1-y)M_{Si} + yM_{Sn} \tag{3.36}$$

where y is the atomic ratio of Sn, which is 0.6 for $Mg_2Si_{0.4}Sn_{0.6}$, and $M_{Si,Sn}$ is the average atomic mass of Si and Sn accordingly with the ratio y.

Phonon scattering by electronic carriers was considered by using:

$$(\tau_{pE,i})^{-1} = (\tau_{pE,i,X3})^{-1} + (\tau_{pE,i,X1})^{-1} \tag{3.37}$$

$$(\tau_{pE,i,j})^{-1} = N_{V,j}\frac{D_e^2(m_j^*)^3 v_i}{4\pi\hbar^4\rho\beta_{i,j}}\left\{x - \ln\left[\frac{1+e^{(\beta_{i,j}-\frac{E_{F,j}}{k_BT}+x^2/(16\beta_{i,j})+x/2)}}{1+e^{(\beta_{i,j}-\frac{E_{F,j}}{k_BT}+x^2/(16\beta_{i,j})-x/2)}}\right]\right\} \tag{3.38}$$

$$\beta_{i,j} = \frac{m_j^* v_i^2}{2k_BT} \tag{3.39}$$

where D_e and ρ are electron deformation potential and density of $Mg_2Si_{0.4}Sn_{0.6}$, respectively. We ignored phonon scattering due to holes (minority carriers) since its influence on the total relaxation time is very small.

Phonon scattering by nanoparticles was considered by using:

$$(\tau_{pNP,i})^{-1} = \varsigma\frac{\pi v_i N_{NP} D_{NP}^6 k_B^4 x^4 T^4}{2k_B^4 D_{NP}^4 x^4 T^4 + 32\hbar^4 v_i^4} \tag{3.40}$$

$$\varsigma = 1 - \exp\left(-\frac{\rho_{NP} - \rho_M}{\rho_M}\right) \tag{3.41}$$

where N_{NP} is the concentration of nanoparticles and D_{NP} is the diameter of nanoparticles with the assumption of a sphere shape. λ accounts for the density difference between the matrix material and TiO_2 nanoparticles. λ approaches 1 when the density difference is infinity. N_{NP} and D_{NP} are related each other since the volume percent of TiO_2 nanoparticles is given.

$$N_{NP} = \frac{X/100}{\frac{4\pi}{3}\left(\frac{D_{NP}}{2}\right)^3} \tag{3.42}$$

where X is the volume percent of TiO_2. N_{NP} was found to be 1.5×10^{17}, 3.1×10^{17}, and 2.8×10^{16} cm^{-3} respectively for samples with 1%, 2%, and 5% TiO_2 nanoparticles.

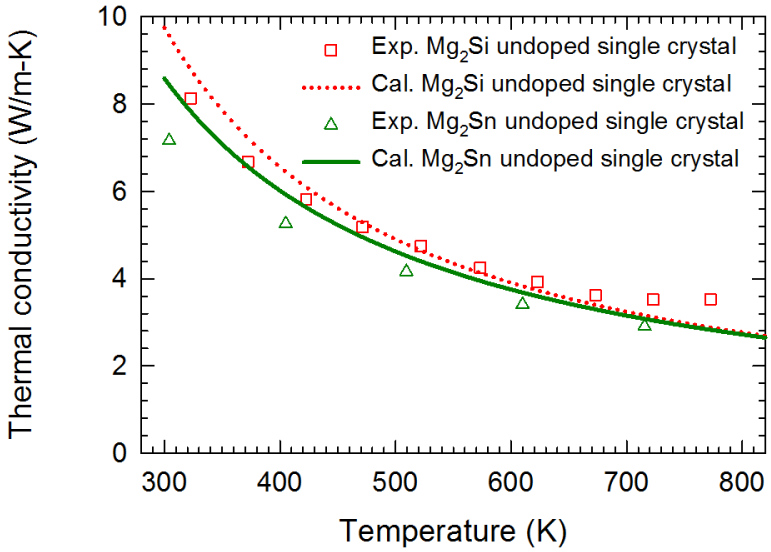

Figure 15. Undoped single crystalline Mg_2Si and Mg_2Sn data[52,53] was fitted to find the Grüneisen parameters (2.5 and 1.7) by considering normal scattering and Umklapp scattering. (reprinted from [18])

Phase segregation was calculated by using the area percentage of Mg_2Sn (A_{Mg2Sn}) obtained from ImageJ software.[54] The segregated Mg_2Si (A_{Mg2Si}) phase was calculated by multiplying A_{Mg2Sn} and both atomic ratio (0.6:0.4 for Sn:Si) and areal ratio (square of lattice constant).

$$A_{Mg_2Si} = A_{Mg_2Sn}\left(\frac{a^2_{Mg_2Si}}{a^2_{Mg_2Sn}} \times \frac{0.6}{0.4}\right) \tag{3.43}$$

where a_{Mg2Si} and a_{Mg2Sn} are lattice constants of Mg_2Si and Mg_2Sn, respectively. The total segregated portion was obtained by adding the two segregated areas.

$$A_{Total} = A_{Mg_2Si} + A_{Mg_2Sn} \tag{3.44}$$

It should be noted that the areal ratio for the two phases is the same as the volumetric ratio, assuming that the thickness is the same for both.

The relaxation time of holes (minority carriers) was adjusted with a multiplying factor β, ranging from 0 to 1 in order to consider the reduction of bipolar thermal conductivity due to the minority carrier scattering by TiO_2 nanoparticles. For the sample without TiO_2 nanoparticles, β=1.

$$\tau_{HH}(E) = \beta\left(\tau_{AC,HH}^{-1}(E) + \tau_{II,HH}^{-1}(E) + \tau_{POP,HH}^{-1}(E) + \tau_{NI,HH}^{-1}(E)\right)^{-1} \tag{3.45}$$

$$\tau_{LH}(E) = \beta\left(\tau_{AC,LH}^{-1}(E) + \tau_{II,LH}^{-1}(E) + \tau_{POP,LH}^{-1}(E) + \tau_{NI,LH}^{-1}(E)\right)^{-1} \tag{3.46}$$

3.4 Results and discussion

3.4.1 Structural characterization

X-ray diffraction (XRD) patterns of Mg_2Si (Figure 16a)[41,55] and Mg_2Sn (Figure 16b)[41,48,55] (for comparison) were plotted together with those of Sample 1 ($Mg_2(Si_{0.4-x}Sn_{0.6})_{1-y}As_xSb_y$ (x=0.008 and y=0.075) without TiO_2) prior to the current assisted sintering process (Figure 16c), TiO_2 nanoparticles only (Figure 16d), Sample 3 (2 vol% TiO_2; Figure 16e), and Sample 4 (5 vol% TiO_2; Figure 16f). Major XRD peaks in Figure 16c are located between those of Mg_2Si and Mg_2Sn such as (111) at 2θ = 23.3° (middle point), (200) at 2θ = 27.0°, (220) at 2θ = 38.5°, (311) at 2θ = 45.3°, and (400) at 2θ =

55.4°. Negligible MgO impurity peak is located at 2θ = 43.1°, which is common in literature.[33,36,48] Sample numbers and corresponding elemental concentrations are listed in Table 4.

Table 4. Atomic ratios of raw elements and volume fractions of TiO_2 nanoparticles in 12 different kinds of solid solutions made of magnesium silicide and magnesium stannide. Note that 10% excessive magnesium was used to compensate loss during synthesis processes. (reprinted from [18])

Sample no.	**Volume fraction**	**Atomic ratio**				
	TiO_2	**Sn**	**Sb**	**Si**	**As**	**Mg**
1	0%	0.5925	0.0075	0.392	0.008	2.2
2	1%					
3	2%					
4	5%					
5	0%	0.585	0.015			
6	0.1%					
7	0.2%					
8	0.5%					
9	1%					
10	2%					
11	5%					
12	10%					

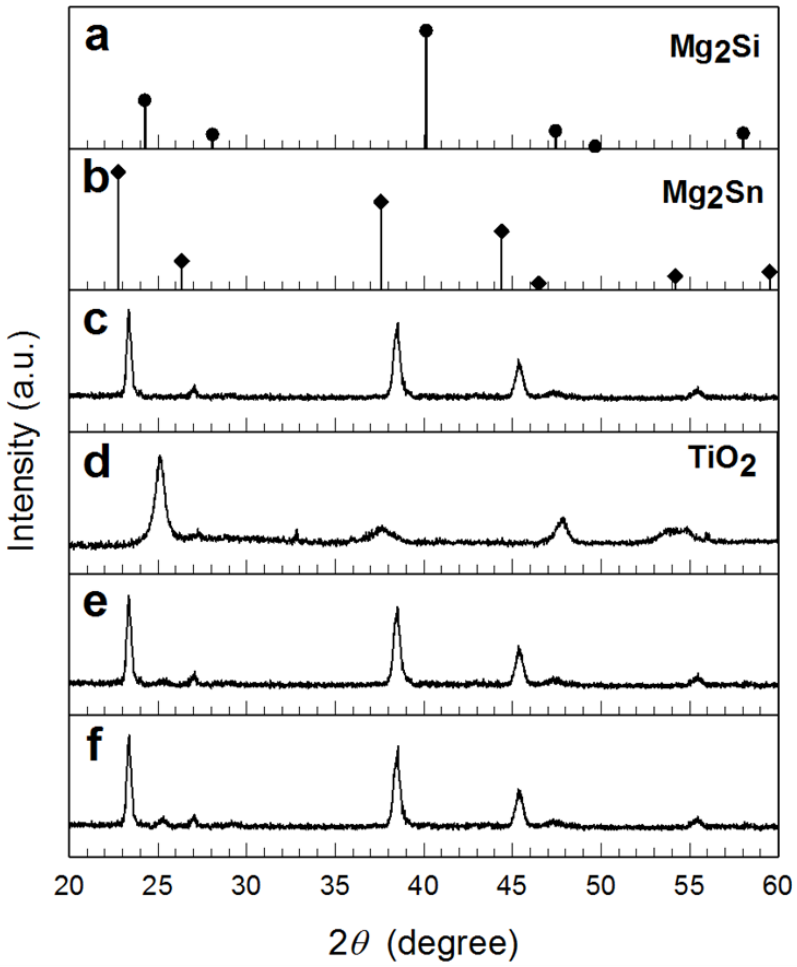

Figure 16. X-Ray powder diffraction spectra of Mg_2Si (JCPDS#: 00-035-0773) (a), Mg_2Sn (JCPDS#: 00-007-0274) (b), Sample 1 (no TiO_2) prior to the current assisted sintering process (c), TiO_2 nanoparticles (d), Sample 3 (2 vol% TiO_2) (e), and Sample 4 (5 vol% TiO_2) (f). (reprinted from [18])

A scanning electron microscope (SEM) image (Figure 17a) of Sample 1 shows two distinct bright and dark regions, which correspond to Mg_2Si-rich and Mg_2Sn-rich locations according to energy dispersive spectroscopy (EDS) results (Figure 18). Figure 17b and c display transmission electron microscope (TEM) images of Sample 1, showing nanograins whose diagonal lengths are mainly in the range of 6~15 nm (from multiple TEM images: see Figure 19). The size distribution of the nanograins is shown in Figure 17d. The nanoscale grain boundaries were clearly observed, suggesting phonon scattering at the interface. A portion of Sample 3 (Figure 17e) along with EDS mapping results (Mg for Figure 17f, Si for Figure 17g, and Sn for Figure 17h) indicates that Mg_2Si and Mg_2Sn were segregated presumably due to the miscibility gap in the phase diagram of $Mg_2(Si,Sn)$ solid solution. The percentage of Mg_2Sn-rich regions was estimated to be 60%±12% from multiple SEM images (Figure 20). We also identified that TiO_2 nanoparticles were homogeneously distributed from EDS results of Sample 3 (Figure 21).

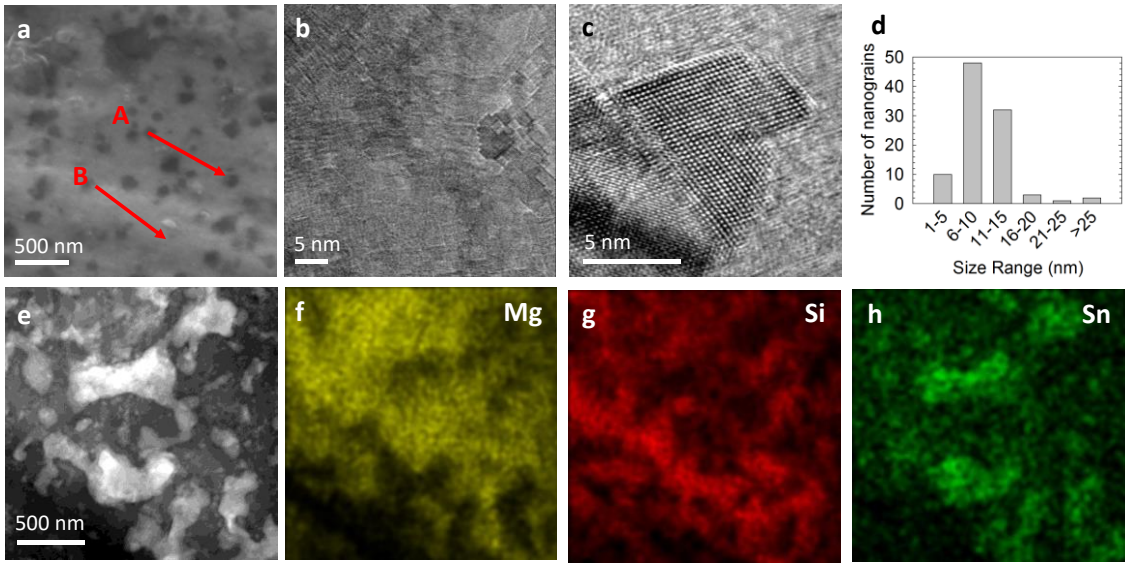

Figure 17. (a) SEM image of a fractured surface of Sample 1. The dark region indicated by 'A' is Sn rich and the brighter region indicated by 'B' is Si rich according to EDS results (see Figure 18). (b) TEM image showing nanograin features with different sizes. (c) TEM image showing crystalline nanograins. (d) Size distribution of nanograins obtained from multiple TEM images (see Figure 19). (e) TEM image with EDS element mapping of Mg (f), Si (g), and Sn (h), respectively. (reprinted from [18])

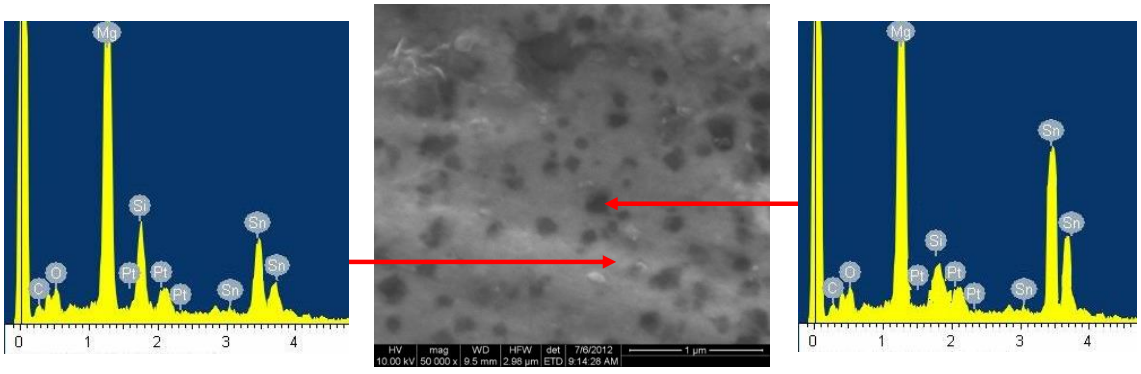

Figure 18. Scanning electron microscope (SEM) image with energy dispersive spectroscopy (EDS) results on dark and grey regions. (reprinted from [18])

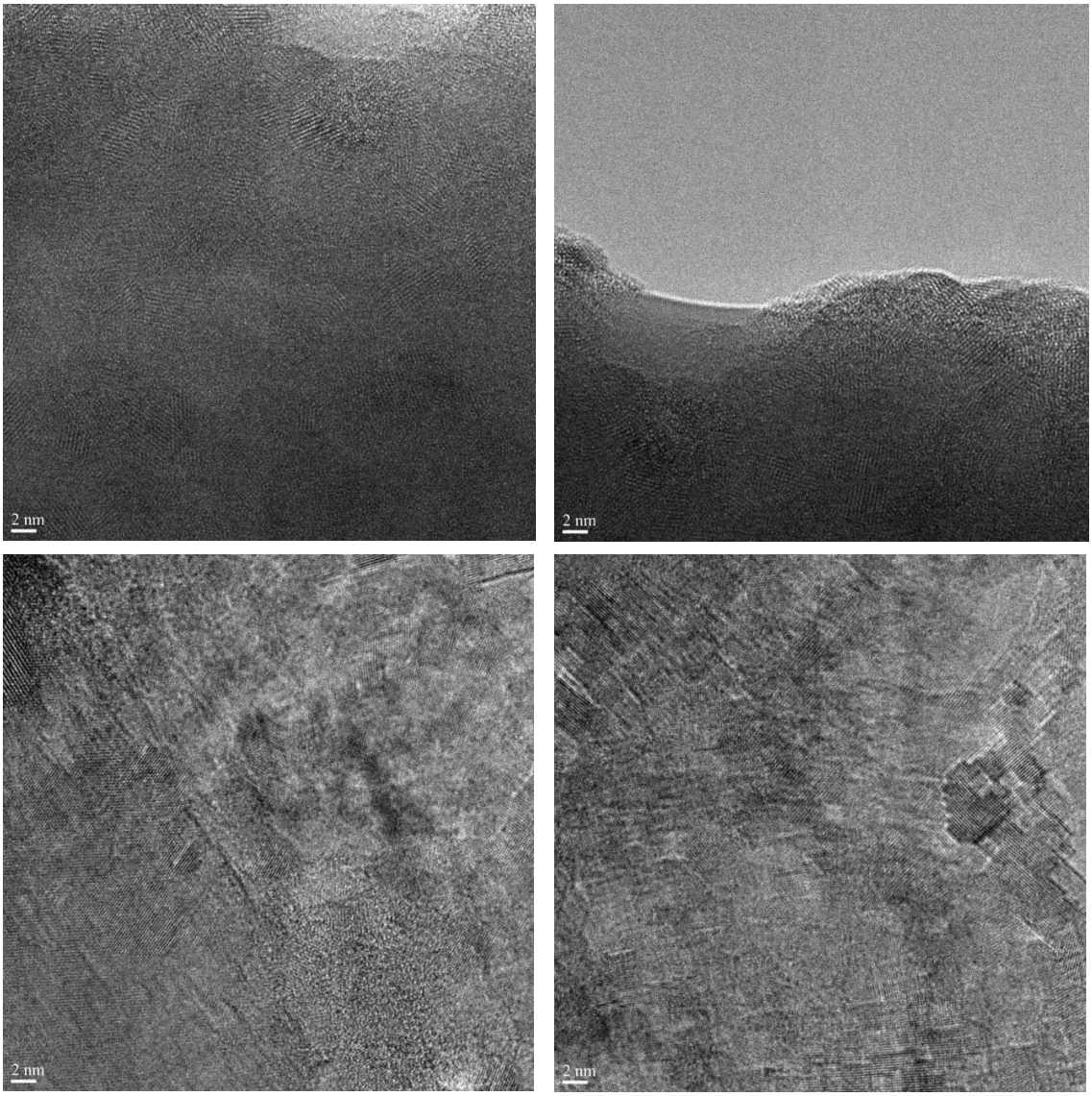

Figure 19. High resolution transmission electron microscope (TEM) images used to determine distribution of nanograin sizes. The scale bar indicates 2 nm (continued to the next page). (reprinted from [18])

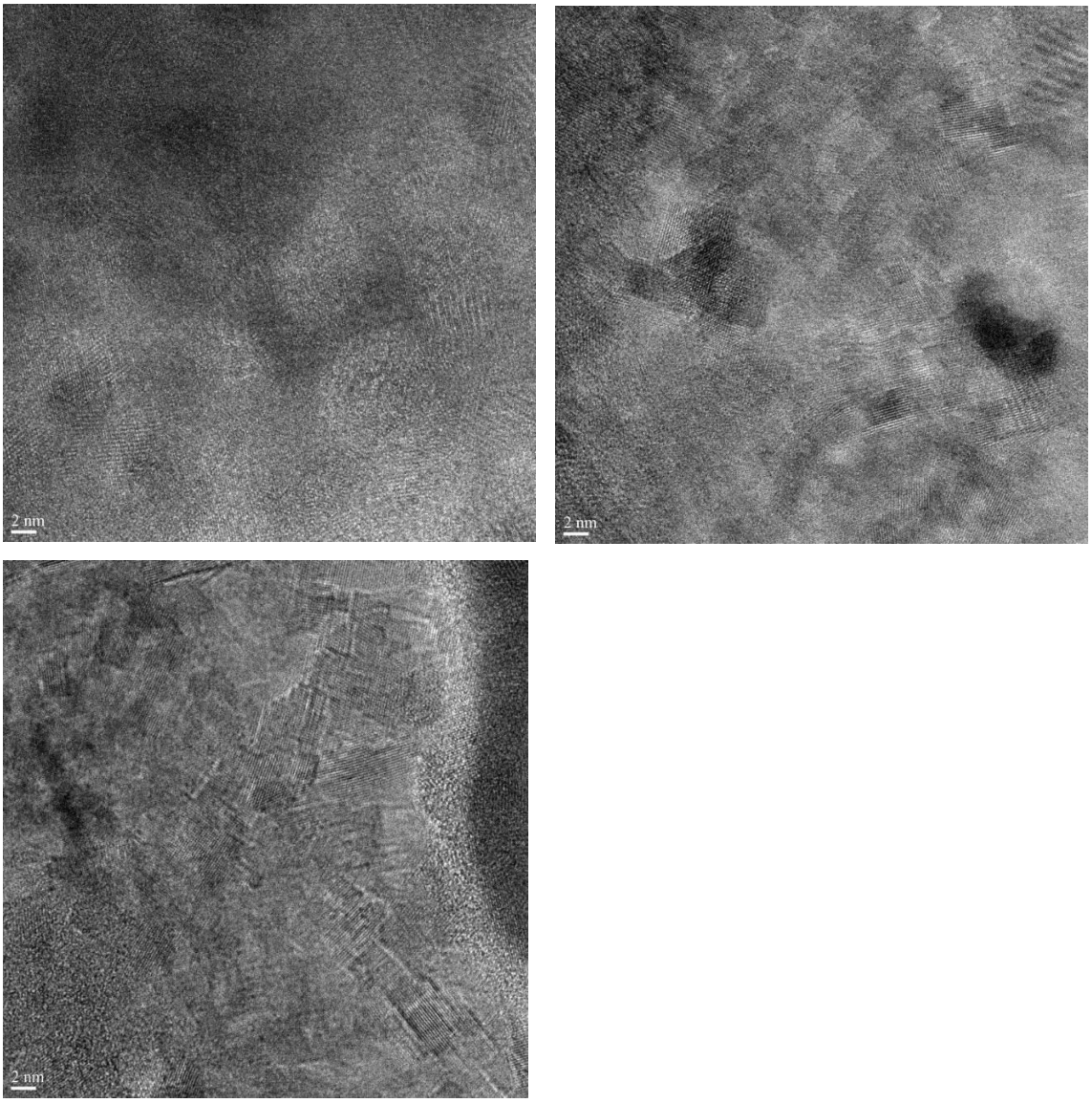

Figure 19. (continued from the previous page) (reprinted from [18])

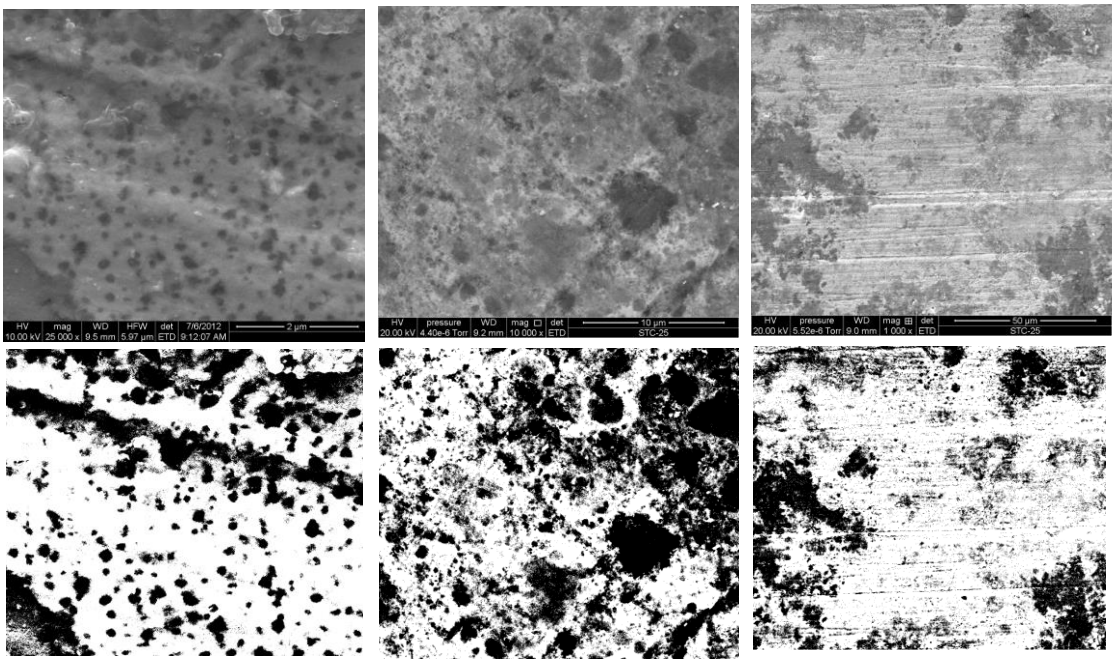

Figure 20. SEM images (upper row) used to estimate the ratio of phase segregation percentage and binary masks (lower row) created from those figures in the first row by using ImageJ. (reprinted from [18])

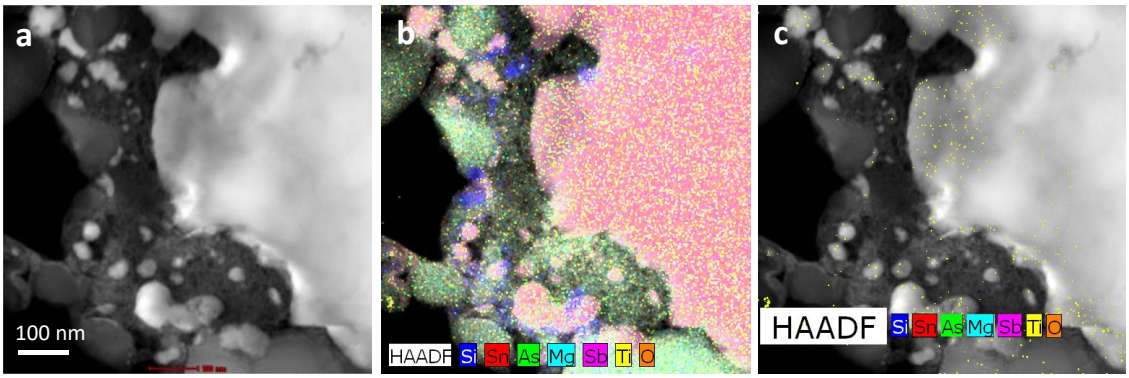

Figure 21. (a) TEM-EDS elemental mapping of Sample 6 (2% TiO_2). (b) Colored mapping results of Si, Sn, As, Mg, Sb, Ti, and O. (c) Only yellow spots were included to show Ti distribution. (reprinted from [18])

3.4.2 Thermoelectric Property Measurements and Theoretical Calculations

The experimentally measured electrical conductivity (Figure 22a) and thermopower (Figure 22b) of Sample 5~12 (1.5% Sb doping) show that the incorporation of TiO_2 nanoparticles reduces the electrical conductivity and enhances thermopower. When the concentration of TiO_2 was increased to 10 vol%, the percentage suppression of electrical conductivity was larger than the percentage increase of thermopower. On the other hand, a small fraction of TiO_2 (0.1, 0.2, and 0.5 vol%) made only marginal differences compared to those of the TiO_2-free sample. Overall, the samples with 1.5% Sb doping have higher electrical conductivity and lower thermopower, compared to those in literature.[31,33,38,44,56] To increase thermopower by decreasing the carrier concentration, we reduced Sb doping to 0.75% (Sample 1~4) since the thermoelectric power factor is proportional to a square of thermopower. We observed enlarged thermopower for Sample 1, 2, 3, and 4, whose TiO_2 concentrations were respectively 0, 1, 2, and 5 vol% (Figure 23a,b), but resulted in only slight improvement in the power factor (Figure 24a,b) due to the reduced electrical conductivity. The addition of TiO_2 displayed similar trends (reducing the electrical conductivity while increasing the thermopower) in the electrical properties for both 1.5% and 0.75% Sb doped samples. Thermal conductivity of the samples with 1.5% (Figure22c) and 0.75% (Figure 23c) Sb doping was suppressed in proportion to the amount of TiO_2. When the TiO_2 concentration of the samples with 1.5% Sb doping was raised from 5% to 10%, thermal conductivity reduction was not significant (Figure 22c). Hence we limited the TiO_2 concentration to 5% for the samples with 0.75% Sb doping (Figure 23c).

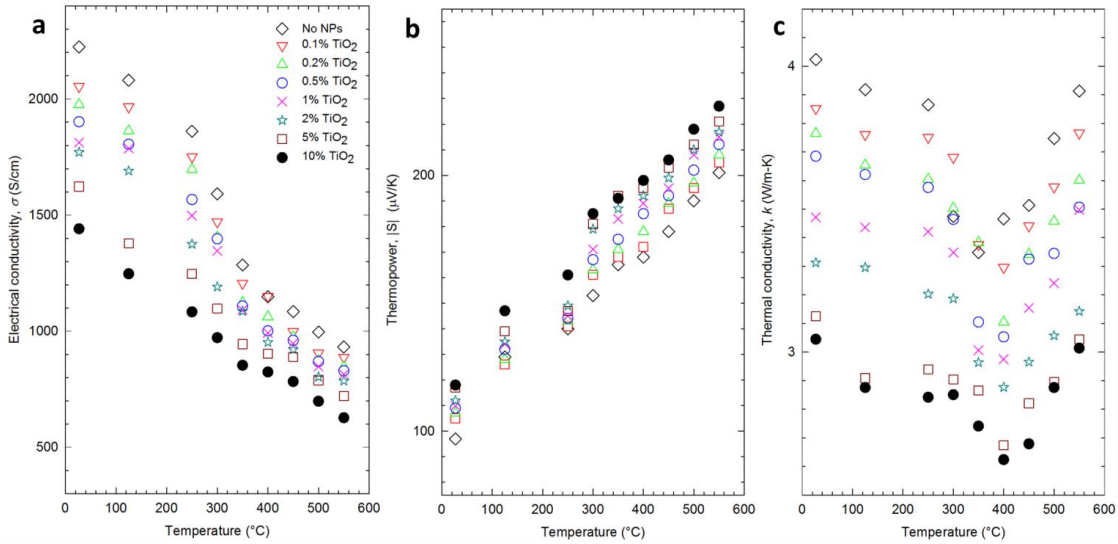

Figure 22. Electrical conductivity (a), thermopower (b), and thermal conductivity (c) of Sample 5~12 containing TiO_2 nanoparticles (0~10 vol%) and 1.5% Sb dopants. (reprinted from [18])

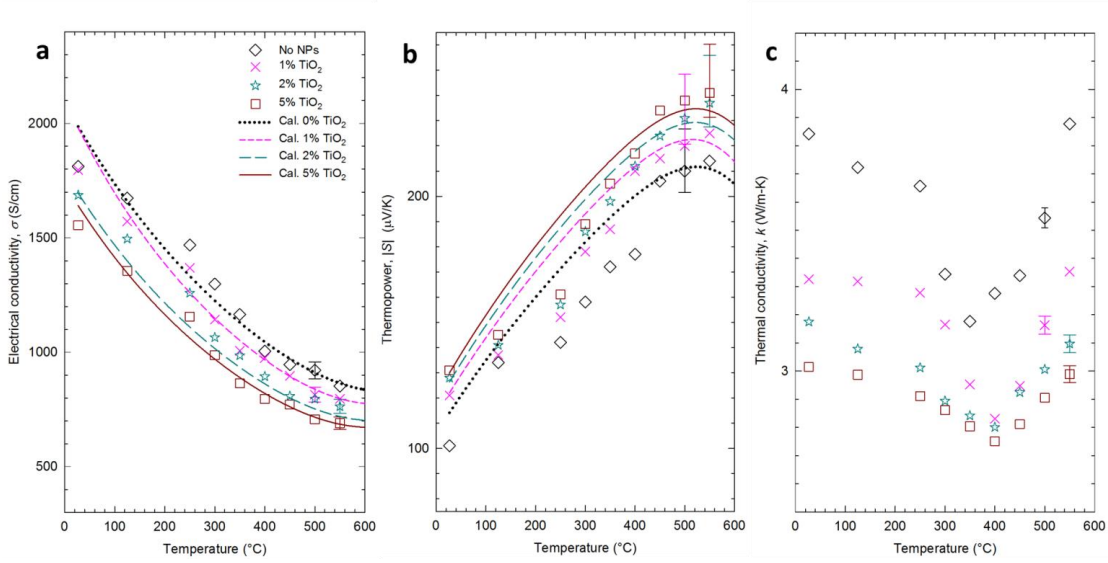

Figure 23. Electrical conductivity (a), thermopower (b), and thermal conductivity (c) of Sample 1~4 containing TiO_2 nanoparticles (0, 1, 2, and 5 vol%) and 0.75% Sb dopants. The symbols are experimental results, and the lines are calculation results. (reprinted from [18])

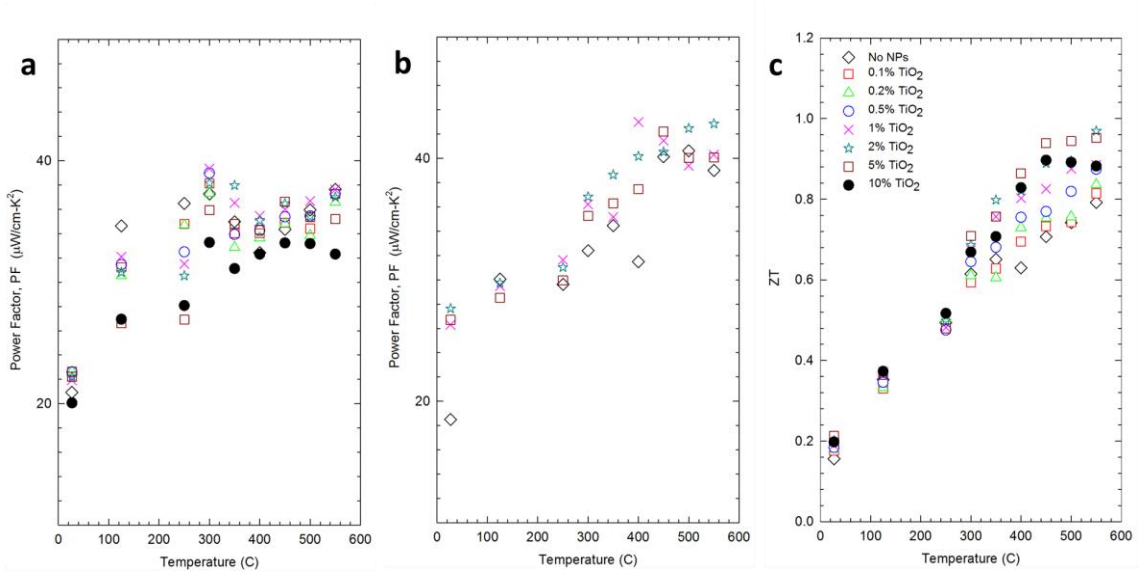

Figure 24. (a) Thermoelectric power factor of Sample 5~12 (a) and Sample 1~4 (b). Thermoelectric figure of merit (*ZT*) of Sample 5~12. (reprinted from [18])

We theoretically calculated thermoelectric properties based on the transport modeling used in Bahk *et al.*,[50] and Yi and Yu,[12] and identified the optimal conditions that maximize *ZT*. We first estimated the Fermi level, which provides electron (or majority) carrier concentration (N_e) (Eq. 3.2) and hole (or minority) carrier concentration (N_h) (Eq. 3.3). Then, we found ionized impurity concentration ($N_{II} = N_e - N_h$) from the charge neutrality (assuming the acceptor concentration is negligible). It should be noted that, when dopants are incorporated into host materials, only a portion of dopants are ionized and the rest becomes non-active or/and non-ionized.[12,57] These impurities alter the electronic relaxation time, which may significantly affect electrical conductivity but negligibly influence thermopower. This can be qualitatively understood from the thermopower relations (Eq. 3.9 and 3.10) where the relaxation time appears in both numerator and denominator.

On the other hand, thermopower is strongly dependent on ionized impurity concentration due to its direct correlation with the Fermi level (Eq. 3.9). Therefore we first sought N_{II} by fitting a series of thermopower data as a function of temperature with Eq. 3.8~3.16 (the electronic relaxation time is described in detail below), and then non-ionized carrier concentration (N_{NI}) was determined by fitting the electrical conductivity. With iteration, we found unique sets of N_{II} and N_{NI} that fitted both temperature-dependent thermopower and electrical conductivity.

Our models considered the electronic relaxation time due to acoustic phonon scattering (τ_{AC}), polar optical phonon scattering (τ_{POP}), ionized impurity scattering (τ_{II}), and non-ionized impurity scattering (τ_{NI}), which were combined by using the Matthiessen's rule to obtain the total scattering relaxation time (Eq. 3.13). The relaxation time due to the acoustic phonon scattering is expressed as:[12]

$$\tau_{AC,j} = \frac{\pi \hbar^4 C_l}{k_B T D_{e\,or\,h}^2 \sqrt{2E} \left(m_j^*\right)^{1.5}} \tag{3.47}$$

where C_l, k_B, T, $D_{e\,or\,h}$, E, and m^*_j are elastic constant, the Boltzmann constant, absolute temperature, electron (subscript e) or hole (subscript h) deformation potential, energy, and effective mass of j valley (X1, X3, HH, and LH), respectively. The deformation potentials for electron and hole were found to be slightly different from those used in Bahk *et al.*,[50] which resulted in a better fitting results for the bipolar thermal conductivity of Sample 1 (0% TiO_2) (see Table 2).

Polar optical phonons also affect the electronic relaxation time:[50]

$$\tau_{POP,j}(E)=\frac{4\pi\varepsilon\hbar\sqrt{2\left(E/m_j^*\right)}}{q^2\omega_o\left(\varepsilon/\varepsilon_\infty-1\right)}\left[N_o\sqrt{1+\frac{\hbar\omega_0}{E}}+\left(N_o+1\right)\sqrt{1-\frac{\hbar\omega_0}{E}}-\frac{\hbar\omega_o N_o}{E}\sinh^{-1}\left(\frac{E}{\hbar\omega_o}\right)^{1/2}+\frac{\hbar\omega_o\left(N_o+1\right)}{E}\sinh^{-1}\left(\frac{E}{\hbar\omega_o}-1\right)^{1/2}\right]^{-1}$$

(3.48)

where N_0=[exp[($\hbar\omega_0$)/(k_BT)]−1]$^{-1}$, and q, ω_o, ε, ε_∞, and N_o are electron charge, optical phonon frequency, permittivity, high frequency permittivity, and the number of optical phonons, respectively. It should be noted that the second and fourth terms in the bracket are related to optical phonon emission by scattering of electronic carriers, which occurs only when the energy of electronic carriers is higher than optical phonon energy, $\hbar\omega_0$. Therefore, the two terms should be disregarded for electronic carriers whose energy is lower than optical phonon energy. Considering the narrow range of optical phonon frequencies, a constant optical phonon energy, $\hbar\omega_0$ =33.3 meV was used.[50] Our heavily doped sample has a carrier energy distribution much wider than $\hbar\omega_0$ (distribution can be obtained from Eq. 3.10), so elastic scattering exists throughout the most of the energy range.

The relaxation time due to non-ionized and ionized impurity scattering can be expressed as:[12]

$$\tau_{NI,j}=\frac{(m_j^*q)^2}{80\pi\hbar^3\varepsilon N_{NI}} \tag{3.49}$$

and

$$\tau_{II,j}(E)=\frac{16\pi\sqrt{2m_j^*}\varepsilon^2E^{3/2}}{q^4N_{II}g};\ g=\ln\left(1+b\right)-\frac{b}{1+b},\ b=\frac{8m_j^*E}{\hbar^2}R_0^2 \tag{3.50}$$

where R_0 indicate the screening length of Coulombic potential, calculated from Thomas-Fermi approximation.[58]

Our models for the electrical properties did not separately consider electronic carrier scattering by nanoparticles and grain boundaries due to lack of knowledge for the specularity parameter for electrons and holes at the grain boundary surface. It has also been shown that the mean free path of electrons (Figure 14) is much shorter than that of phonons (up to microns[59]), so the influence of grain boundaries on electron transport is much weaker compared to phonons, as demonstrated in various nanostructured bulk systems experimentally and theoretically.[58]

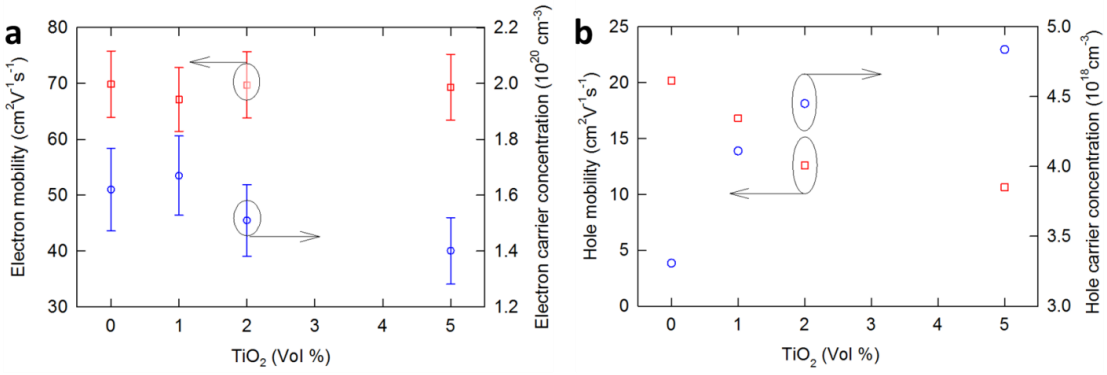

Figure 25. (a) Electron mobility and carrier concentration of Sample 1, 2, 3, and 4 from Hall measurements. (b) Calculated hole mobility and carrier concentration for of Sample 1, 2, 3, and 4. (reprinted from [18])

Thermal conductivity (k) was obtained by summating electronic thermal conductivity (k_e), lattice thermal conductivity (k_l), and bipolar thermal conductivity (k_{bi}):

$$k = k_e + k_l + k_{bi} \tag{3.51}$$

k_e was calculated by using the Wiedemann-Franz law (Eq. 3.20). Note that the Lorenz number for this work was calculated based on Eq. 3.21 since the Lorenz number for

semiconductors is typically smaller than the commonly used value (2.44×10^{-8} V^2K^{-2}) for metals. k_{bi} was obtained from Eq. 3.22 with electrical conductivity and thermopower of electrons and holes (Eq. 3.23 and 3.24).

The lattice thermal conductivity was calculated by using a modified Callaway model (Eq. 3.25~3.30) with separately considered longitudinal and transverse modes of phonons whose relaxation time ($\tau_{p,i}$) can be expressed as:

$$\frac{1}{\tau_{p,i}} = \frac{1}{\tau_{pN,i}} + \frac{1}{\tau_{pR,i}} = \frac{1}{\tau_{pN,i}} + \frac{1}{\tau_{pU,i}} + \frac{1}{\tau_{pA,i}} + \frac{1}{\tau_{pB,i}} + \frac{1}{\tau_{pE,i}} + \frac{1}{\tau_{pNP,i}} \tag{3.52}$$

where $\tau_{pN,i}$, $\tau_{pU,i}$, $\tau_{pA,i}$, $\tau_{pB,i}$, $\tau_{pE,i}$, and $\tau_{pNP,i}$ are the phonon relaxation times corresponding to normal scattering, Umklapp scattering, alloy scattering, grain boundary scattering, electron-phonon scattering, and scattering by nanoparticles, respectively (Eq. 3.31~3.42). The subscript i denotes the phonon mode, which is either longitudinal or transverse mode.

We first fit the experimental thermal conductivities of undoped single crystalline Mg_2Si and Mg_2Sn,[52,53] which requires only two types of relaxation time terms corresponding to normal scattering (Eq. 3.31 and 3.32) and Umklapp scattering (Eq. 3.33). We obtained the speed of sound and the Debye temperature in the longitudinal and transverse mode (see Table 3) from literature,[51] and the Grüneisen parameters were used as fitting parameters for Mg_2Si and Mg_2Sn. Note that the different vibration modes for Grüneisen parameters were not considered in order to avoid arbitrary fitting. Grüneisen parameters of 2.5 and 1.7 for Mg_2Si and Mg_2Sn resulted in good agreement with the experimental data (Figure 15).

Then, the linear average value of the Grüneisen parameters was employed for solid solutions of Mg_2Si and Mg_2Sn (4:6 atomic ratio; $Mg_2Si_{0.4}Sn_{0.6}$), where alloy scattering needs to be additionally considered. When alloy scattering was introduced in our model to fit the experimental "lattice" thermal conductivity of Sample 1 (0% TiO_2), both with and without the grain boundary scattering, the calculation results (Figure 26a,b; 0% segregation) significantly underestimated the experimental results (symbols in Figure 26a,b). Note that the experimental values were obtained by subtracting (k_e + k_{bi}) from measurement data. This discrepancy can be attributed to the model omitting the effect of segregated Mg_2Si and Mg_2Sn phases that were observed from our EDS mapping results in Figure 17e~h and Figure 21. Similar segregations were also observed from literature.[33,38,42,48]

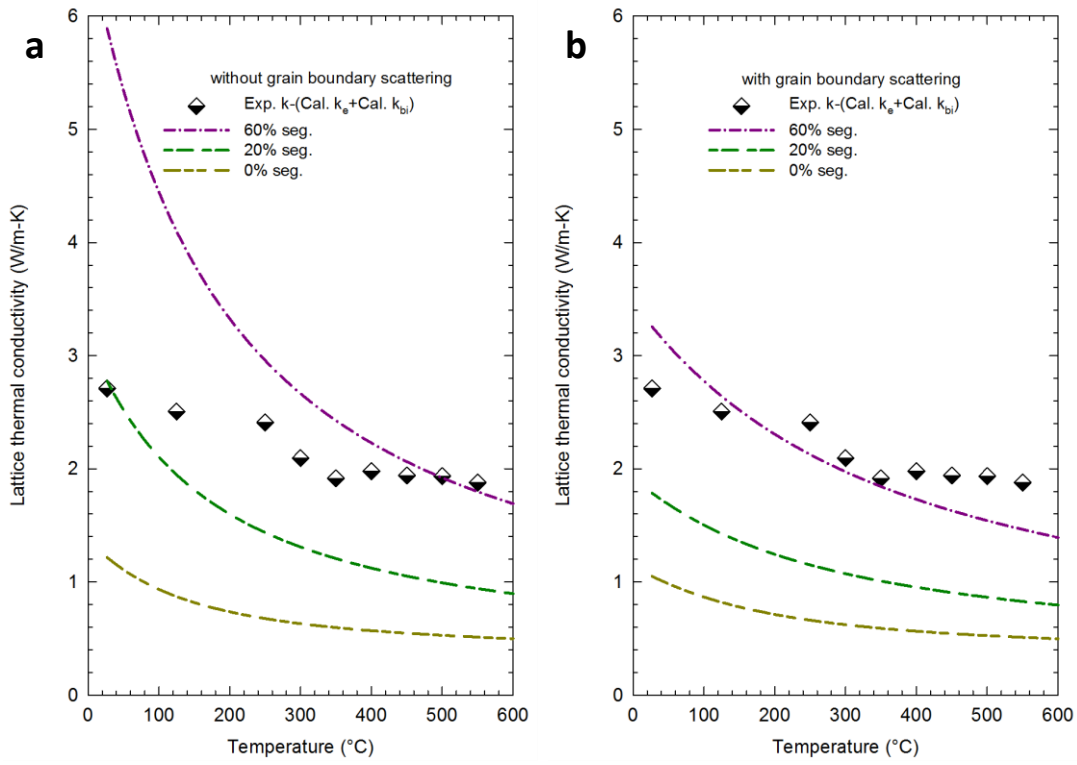

Figure 26. (a) Lattice thermal conductivity of Sample 1 (symbols; 0% TiO_2) by subtracting electronic and bipolar thermal conductivity from experimentally obtained thermal conductivity. The lines are calculated results "without" considering phonon scattering at the grain boundary when segregated volume is 0, 20, and 60%. (b) The symbols are the same as those in 'a'. When the phonon scattering at the grain boundary was included in the calculation, lattice thermal conductivity (lines) were suppressed mainly at low temperatures. (reprinted from [18])

To take the segregation into account, a parallel thermal resistor model composed of three parts, a homogenous solid solution of $Mg_2Si_{0.4}Sn_{0.6}$ and segregated Mg_2Si and Mg_2Sn, was employed to obtain lattice thermal conductivity.

$$k_l = (1-f)k_{l,Mg_2Si_{0.4}Sn_{0.6}} + f\left[\frac{(1-y)a^3}{(1-y)a^3 + yb^3}k_{l,Mg_2Si} + \frac{yb^3}{(1-y)a^3 + yb^3}k_{l,Mg_2Sn}\right] \quad (3.53)$$

where a and b are respectively lattice constants[51] of Mg_2Si (0.639 nm) and Mg_2Sn (0.677 nm) in order to consider the volume difference per given number of atoms. According to the phase diagram in literature,[47] it is suggested that pure Mg_2Si and pure Mg_2Sn are present, but we cannot completely exclude presence of their mixtures. Nevertheless, we used a simple model (Eq. 3.53) because of difficulties in taking all various compositions into account. The atomic ratio of Sn is y (=0.6), and the volume fraction of the segregated portion is f. We estimated f with SEM images (Figure 20a~c) of multiple samples (0% TiO2) whose cross-sections were polished to clearly observe different phases. Since the dark area is Sn-rich according to EDS results (Figure 18), we considered that the dark regions in the SEM images are segregated Mg_2Sn. The small Si EDS peak from the dark spot may come from Si-rich or homogeneous mixture nearby or/and underneath the dark spot. The area percentage of the dark region was acquired with ImageJ program,[54] as shown in Figure 20d~f. Based on the area of Mg_2Sn, vol% of Mg_2Si was calculated from the atomic ratio of Si to Sn (4:6) and the ratio of lattice constant of Mg_2Si to that of Mg_2Sn due to the difficulties in identifying Si-rich regions from EDS data. The total segregation was calculated to be 60% (average) 12% (standard deviation) according to Eq. (3.43) and (3.44). With f = 0.6, calculated lattice thermal conductivity (Figure 26a; 60% segregation) better fitted the experimental data but it overestimated low-temperature experimental values.

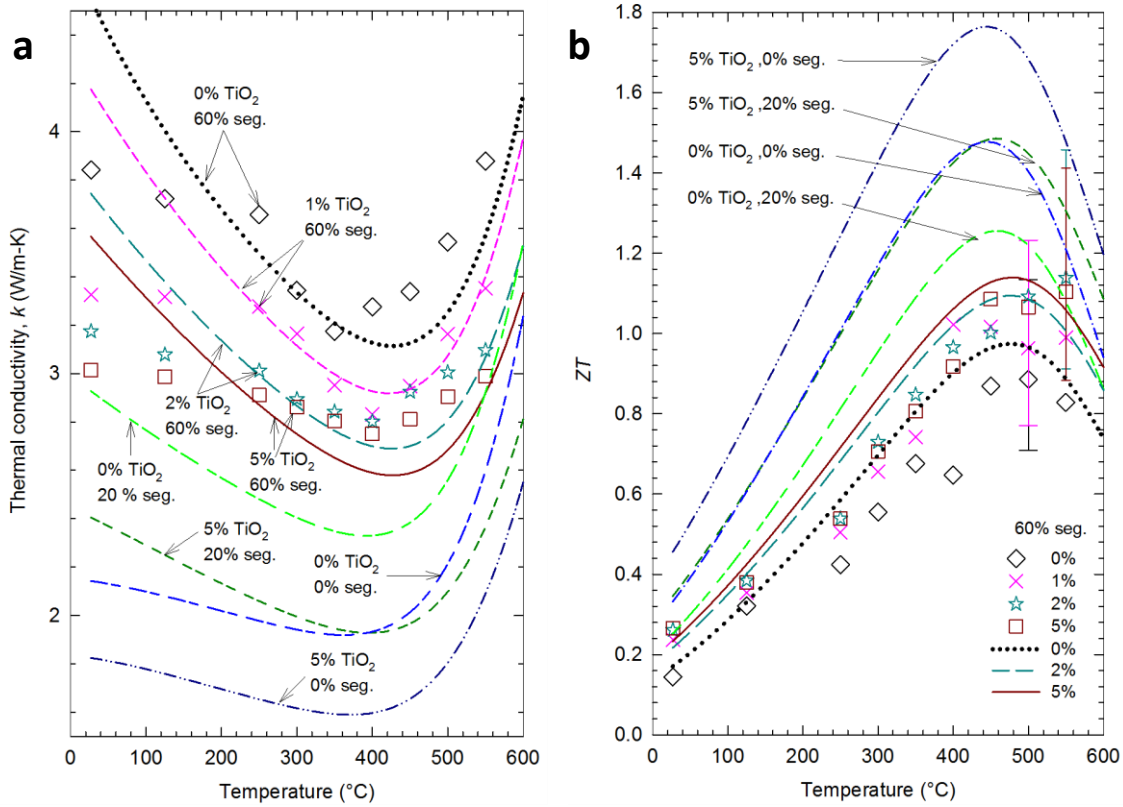

Figure 27. (a) Thermal conductivity of Sample 1, 2, 3, and 4 (symbols), and fitting results (lines) with 60% segregation. When segregation is lowered to 20% and 0% with addition of 5 vol% TiO_2 nanoparticles, significantly suppressed thermal conductivity was predicted by theoretical calculations (see lower four lines). (b) *ZT* values of Sample 1, 2, 3, and 4 (symbols), and fitting results (lines) with 60% segregation. Upper four lines are predicted *ZT* values for ideal cases of 0% and 20% segregation. (reprinted from [18])

This discrepancy at low temperatures is likely to be due to phonon scattering at nanograin boundary surfaces, which becomes intense when phonon mean free paths are longer than the grain size. The phonon mean free paths at low temperatures are longer than those at high temperatures, so the nanograins suppress lattice thermal conductivity

mainly at low temperatures. Here we acquired the average grain size (d) of 11 nm (distance along the diagonal direction of the nanograins) from multiple TEM images (Figure 19), and fitted our experimental data with a specularity parameter (α) of 0.65 (Figure 26b: 60% segregation) in $\tau_{pB,i}$:

$$(\tau_{pB,i})^{-1} = \frac{v_i}{d}\left(\frac{1-\alpha}{1+\alpha}\right) \tag{3.54}$$

This grain boundary scattering also made the lattice thermal conductivity for the case of 0% segregation slightly lower (Figure 26b). The relatively large specularity parameter may imply that the grain boundary is less diffusive compared to the boundary surface (hard limit that phonons cannot cross over) of nanowires.[12] This term may also include the effects related to strain and dislocation near the grain boundary. We were not able to clearly see wide strain fields propagated from the grain boundaries from the TEM images. Therefore we did not consider additional scattering terms here although we cannot completely exclude the possibility of having strain on the whole entire grains. We also considered electron-phonon scattering with $\tau_{pE,i}$ term (Eq. 3.37~3.39), whose influence on the lattice thermal conductivity is relatively small.

When TiO_2 nanoparticles were added to the host materials, the thermal conductivity was suppressed, as experimentally shown in Figure 22c and 23c. In the calculations, this was considered by introducing $\tau_{pNP,i}$ with the diameter (D_{NP}) of nanoparticles and their concentration (N_{NP}):

$$(\tau_{pNP,i})^{-1} = \varsigma \frac{\pi v_i N_{NP} D_{NP}^6 k_B^4 x^4 T^4}{2k_B^4 D_{NP}^4 x^4 T^4 + 32\hbar^4 v_i^4} \tag{3.55}$$

where N_{NP} and D_{NP} are the concentration and diameter of nanoparticles assuming the nanoparticles are in a sphere shape. ς accounts for the density difference between the host material and TiO_2 nanoparticle so that it approaches to 1 when the density difference is infinity (Eq. 3.41). For 1 and 2 vol% TiO_2, D_{NP} was set to 5 nm, which is the nominal diameter of individual nanoparticles according to the manufacturer's specification as well as our observation from TEM images. For 5 vol% TiO_2, D_{NP} was chosen to be 15 nm since nanoparticles tend to aggregate with higher concentrations. Presumably, this is the main reason for the relatively small reduction in thermal conductivity when TiO_2 was increased from 2% to 5% (3% increment), compared to those from 0% to 1% and 1% to 2% (1% increment). N_{NP} was found from Eq. 3.42 with the volume percent of TiO_2 nanoparticles.

In order to better fit the experimental thermal conductivity with all aforementioned relaxation times, we additionally considered a multiplying factor for the relaxation time corresponding to bipolar thermal conductivity. We noticed that the bipolar thermal conductivity was suppressed when TiO_2 nanoparticles were added, which is indicated by the lower slopes of thermal conductivity as a function of temperature (> ~450 °C) with higher nanoparticle concentrations (Figure 23c). The bipolar thermal conductivity becomes prominent at high temperatures where the power factor is maximized, so it should be kept small to achieve a high ZT. In highly n-doped semiconductors, electrical conductivity (σ_e) by electrons is generally much larger than that (σ_h) by holes mainly due to the large difference in the electronic carrier concentration, and thermopower (S_h) by holes is much larger than that (S_e) by electrons

mainly due to the larger energy gap between the Fermi level and the mean energy of holes. ($S_h - S_e$) negligibly changes with TiO_2 contents (866, 859, 857, and 855 μV/K for 0, 1, 2, and 5 vol% TiO_2 samples, respectively). Then, the bipolar thermal conductivity expression can be written as:

$$k_{bi} = \frac{\sigma_e \sigma_h}{\sigma_e + \sigma_h}(S_e - S_h)^2 T \approx (\text{Constant} \times T)\sigma_h \tag{3.56}$$

Therefore σ_h mainly determines the bipolar thermal conductivity. σ_h is dependent on both hole concentration (N_h) and hole mobility (μ_h). N_h was increased with TiO_2 addition according to our calculations (Eq. 3.3), as shown in Figure 25b. Therefore we believe that the suppression of hole mobility can be attributed to the reduction of bipolar thermal conductivity. TiO_2 nanoparticles by themselves could be effective scattering centers or/and they may induce effective charge traps for the minority carrier presumably due to relatively low energy of minority carriers compared to majority carriers. This may also be related to the minority carrier blocking effect by TiO_2 heterostructure barriers.[60-62]

In our calculations, we adopted an adjustable parameter (β), and then multiplied the hole relaxation time by β (Eq. 3.45 and 3.46) since the mobility has a direct correlation with the relaxation time ($\mu_h = q\tau_h / m_{h*}$). Then, with the adjusted hole relaxation time, electrical conductivity and thermopower were re-calculated. Note that the influence of this mobility change on electrical conductivity and thermopower was negligible. The mobility of hole carriers was found to steadily decrease with TiO_2 content, from 20 cm^2/V-s for the case of 0% TiO2 (β=1) to 16.8 (β=0.8), 12.6 (β=0.6), and 10.6 cm^2/V-s (β=0.5) respectively for 1, 2, and 5 vol% TiO_2 samples, by fitting the

experimental data, as shown in Figure 27a (upper four fitting lines). To better fit the thermal conductivity at low temperatures where the bipolar term is negligible, we adjusted the specularity parameter to 0.60, 0.55, and 0.50, respectively for 1, 2, and 5 vol% nanoparticles. Additional nanoparticles are likely to disrupt the material structures, which may increase phonon scattering at the grain boundary.

We further estimated thermal conductivity when the segregation (60%) becomes smaller (20% and 0%) as well as TiO2 nanoparticles are 0 and 5 vol%, as shown in the lower four lines in Figure 27a. The lowest thermal conductivity was obtained with 0% segregation and 5 vol% nanoparticles. Thermal conductivity was smaller with lower segregations and higher nanoparticle concentrations. It is very interesting to see the strong influence of the segregation on thermal conductivity, but 0% segregation may not be practically feasible due to the miscibility gap. Therefore, addition of TiO_2 nanoparticles could be an alternative to reduce the thermal conductivity. For example, one can have segregation above zero (e.g., 20%), and then 5 vol% TiO_2 can be used to have thermal conductivity close to that of a 0%-segregated sample (without TiO_2). In this case, when segregation changes from 0% to 20%, the increase of lattice thermal conductivity can be compensated by the addition of the nanoparticles. The difference in lattice thermal conductivity is shown in Figure 26b.

Figure 27b shows experimentally obtained ZT (symbols) of samples with 2 and 5 vol% TiO_2 nanoparticles, which were fitted with 60% segregation. The highest experimental ZT value was ~1.1 at ~550 ^oC with 2 and 5 vol% TiO_2, which was greatly improved from the sample without TiO2 nanoparticles (ZT ~ 0.9). This ZT increase

mainly comes from the reduction of lattice and bipolar thermal conductivity as a result of incorporation of TiO_2 nanoparticles. Compared to the best ZT values in literature, our ZT values are lower due to higher thermal conductivity. The origin of the high thermal conductivity is thought to be the inevitable phase segregation, suggesting that the significantly low thermal conductivity reported in literature could be due to high porosity during thermal conductivity measurements or/and a small fraction of segregated phases that is likely to be subject to further segregation at high temperatures. We also estimated the upper bound ZT (~1.8) with 0% segregation and 5 vol% nanoparticles, which is lowered to ~1.5 for a practically feasible case of 20% segregation and 5 vol% nanoparticles. To visualize the influence the nanoparticle addition, ZT without nanoparticles were also plotted together in Figure 27b.

3.5 Conclusions

We synthesized solid solutions of magnesium silicide and magnesium stannide with arsenic and antimony as dopants by using a current assisted sintering method. TiO_2 nanoparticles (0~10 vol%) were used as additives to suppress lattice thermal conductivity. Electrical conductivity, thermopower, and thermal conductivity were all experimentally measured, and the experimental data was fitted to predict the optimum conditions to maximize ZT. Our samples contain nanograins and segregated Mg_2Si and Mg_2Sn phases according to SEM, TEM, and EDS results. The maximum ZT from our experiments was 1.1 with 2 and 5 vol% TiO_2 nanoparticles, which was improved from 0.9 without the nanoparticles. This increase in ZT mainly comes from suppressed lattice

thermal conductivity in addition to lower bipolar thermal conductivity at high temperatures. We found that the segregation increases lattice thermal conductivity, and 0% segregation resulted in the lowest lattice thermal conductivity. Considering the phase segregation is difficult to avoid due to the miscibility gap, addition of extraneous TiO_2 nanoparticles was found to be effective to further suppress lattice thermal conductivity. The upper bound of ZT was predicted to be 1.8 for the ideal case of no phase segregation and addition of 5 vol% TiO_2 nanoparticles. We believe further study to suppress the phase segregation may provide key knowledge in synthesizing practically viable $Mg_2(Si,Sn)$.

CHAPTER IV

STABLE SOLID SOLUTION OF $Mg_2(Si,Sn)$ SYNTHESIZED BY HIGH ENERGY BALL MILLING ELEMENTAL POWDER

4.1 Introduction

As investigated in Chapter 3, it is desired to have homogeneously well-mixed solid solution rather than the composite system with separated phases. Proposed work is to change the material preparation and process method so as to achieve the more favorable condition toward the better solid solution kinetically and thermodynamically as literature[63,64] showed the possibility of modified miscibility gap depending on the microstructure of material system due to several factors such as interface coherency, dopant, *etc.*

Also the systematic study on how the degree of mixing between two types of atoms affects the entire thermoelectric performance, as shown in Figure 28, including thermopower and electrical conductivity in addition to the lattice thermal conductivity in the previous chapter will be informative inasmuch as most of the efficient thermoelectric materials have alloyed system composed of two types of atoms with the identical crystal structure.[11,23]

In the work of this chapter I utilized the high energy ball milling, which involves the more dynamic motion of mixing, rather than solid state reaction of Chapter 3, to prepare the alloyed powder such as Mg_2Si, Mg_2Sn, and $Mg_2Si_{1-x}Sn_x$ out of Mg, Si, Sn elemental powders.

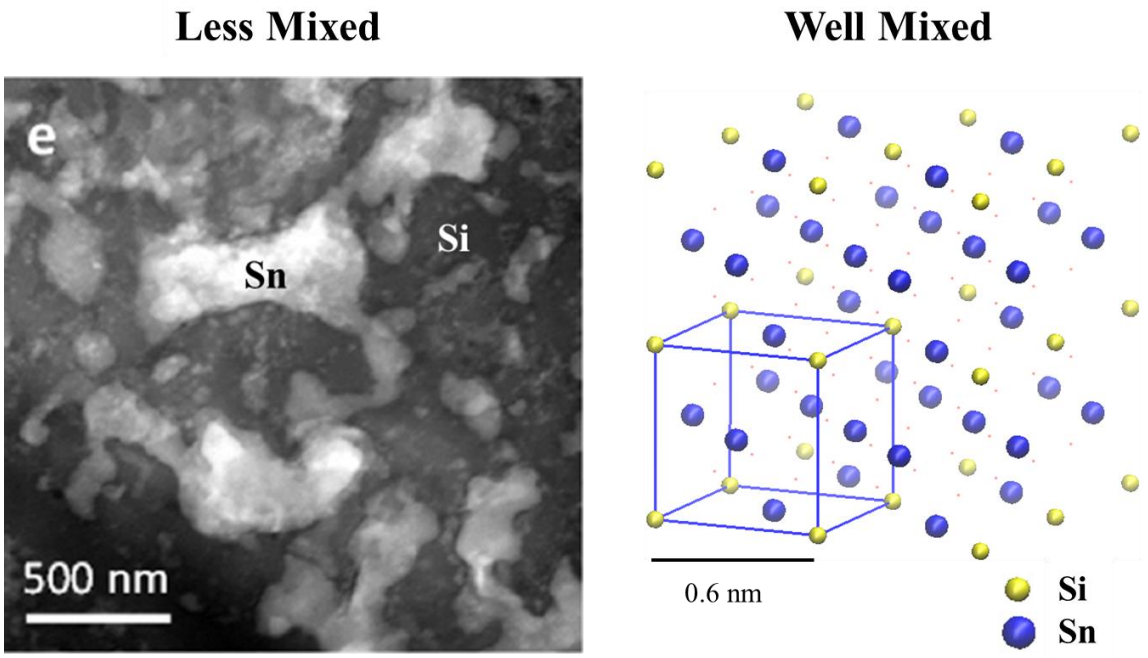

Figure 28. TEM image of $Mg_2Si_{0.4}Sn_{0.6}$ pellet sample which consists of Sn-rich and Si-rich phases (left) and the schematic for idealized solid solution of $Mg_2Si_{0.25}Sn_{0.75}$ as an example (right). (reprinted from [18])

4.2 Experimental

Figure 29a shows the procedure of current-assisted sintering to perform the experiments. The sintered pellets can be observed in Figure 29b together with 1 cent coin for reference. Hall effect measurement was performed to ensure that the sintered pellets are in the desired doping range whose chemical potential is 0 ~ 0.5 k_BT above the conduction band edge so as to have the optimized thermoelectric properties.

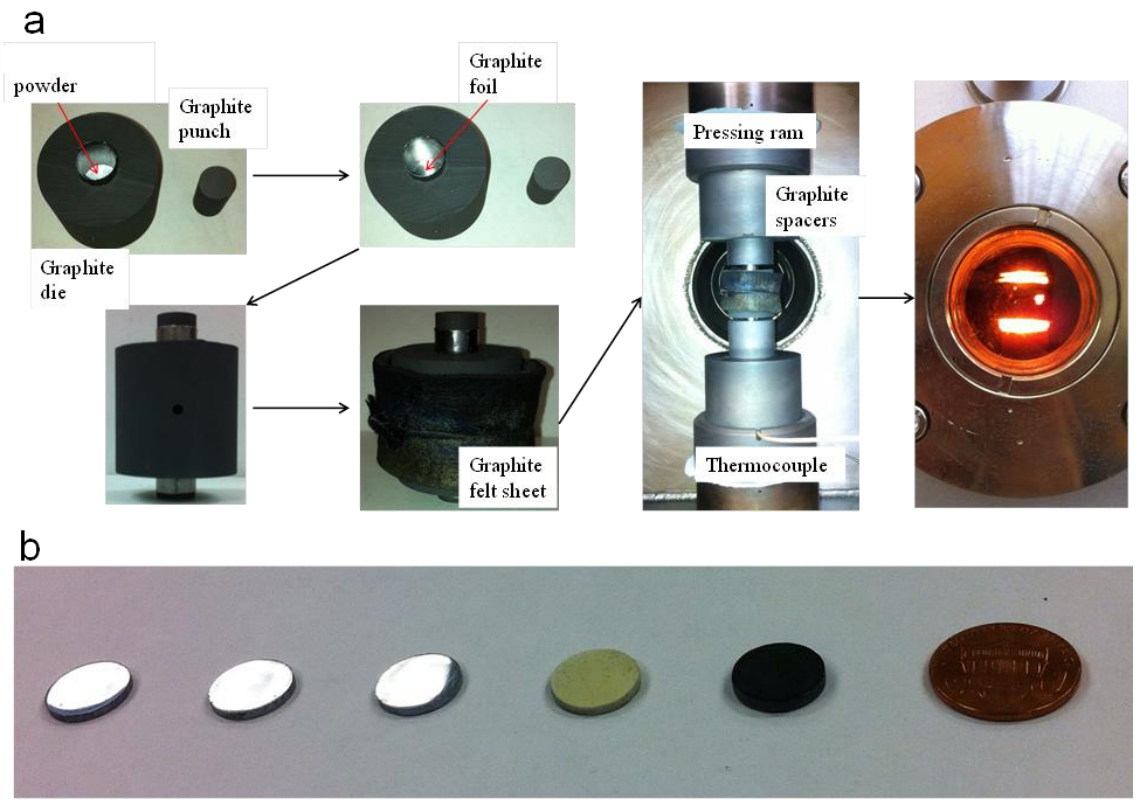

Figure 29. (a) Procedure of synthesizing bulk pellet samples using current assisted sintering method, (b) synthesized samples (Mg_2Si, Mg_2Sn, $Mg_2Si_{0.3}Sn_{0.7}$, ZnO, and $SrTiO_3$ from left to right) with 1-cent coin for comparison.

4.3 Results and discussion

4.3.1 Post annealed $Mg_2Si_{0.3}Sn_{0.7}$

Figure 30 shows the XRD and thermal conductivity results of $Mg_2Si_{0.3}Sn_{0.7}$ samples with different post annealing time at the same temperature employed for the current-assisted sintering. Although some literature for $Mg_2Si_{1-x}Sn_x$ claims the miscibility gap, hence the phase segregation into Sn-rich and Si-rich happens in the material system, the sample in this work showed no direct evidence of segregated phases within the scope of XRD and thermal conductivity measurement results. As post

annealing time increased from 0 hours to 18 hours, the XRD peak becomes rather sharper without any separation, which implies no significant phase segregation. Figure 30b shows the thermal conductivity measurement results together with two plots from literature, one for segregated $Mg_2Si_{0.4}Sn_{0.6}$ sample[18] and the other for the desired solid solution of $Mg_2Si_{0.3}Sn_{0.7}$.[56] It should be noted that the little difference in the ratio of Sn and Si are marginal so that the difference is mainly from the existence of separated phases. As witnessed already in Figure 30a, the thermal conductivity change was also marginal, but just retaining its low thermal conductivity similar to literature value for solid solution (solid line) up to the post annealing time of 12 hours. When post annealing time increased up to 18 hours the thermal conductivity even decreased a lot due to the loss of its carrier concentration leaving only its lattice thermal conductivity portion with little contribution of electronic thermal conductivity. The increasing trend with temperature after 500 K is the nature of bipolar thermal conductivity, which well explains the dropped carrier concentration consistently. In short, the thermal conductivity of the samples prepared by high energy ball milling never approached to the reported value for segregated sample in literature, implying the well maintained solid solution.

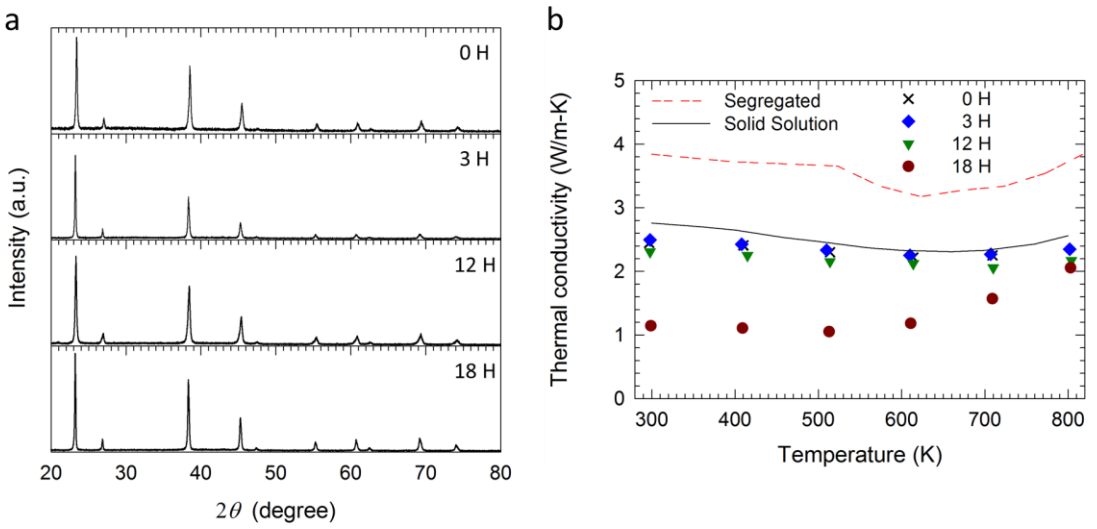

Figure 30. (a) XRD results and (b) thermal conductivity of $Mg_2Si_{0.3}Sn_{0.7}$ samples with various post annealing time.

4.3.2 Separate preparation of Mg_2Sn and Mg_2Si

In order to perform an experiment to check whether the maintained solid solution with post annealing is favorable thermodynamically, separate powder of Mg_2Sn and Mg_2Si were prepared so as to track the change with post annealing of Mg_2Sn – Mg_2Si composite system.

Figure 31a shows the XRD results of Mg_2Sn and Mg_2Si pellets implying the good crystallinity based on the proper peak locations and sharpness. It should be noted that the peaks of Mg_2Sn are shifted toward left compared to those of Mg_2Si because of lattice constant difference while the crystal structure is the same which is consistent to the observation in Chapter 3. Figure 31b shows the ZT of two pellets determined from the measured thermal conductivity, electrical conductivity, thermopower, and temperature. Two solid lines from literature[65,66] are present for the purpose of

comparison and assurance of the quality of each sample as building blocks to form the solid solution of $Mg_2Si_{0.3}Sn_{0.7}$. Slight difference between my samples and literature is owing to the nature of ZT, a strong function of carrier concentration, so that perfect matching is challenging unless the doping level is precisely controlled.

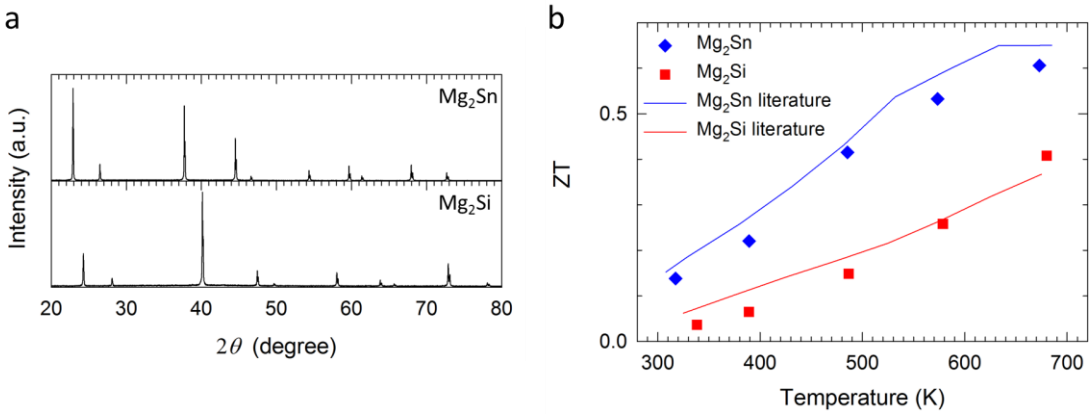

Figure 31. (a) XRD results of Mg_2Sn and Mg_2Si and (b) ZT results of Mg_2Sn and Mg_2Si.

4.3.3 Post annealed Mg_2Sn : Mg_2Si = 7:3 composite

Figure 32 and Figure 33 show experimental results by preparing pellet samples out of individually prepared Mg_2Sn and Mg_2Si powders with various conditions of mixing and post annealing time. Table 5 shows the list of pellets made from 6.5 g of the mixture Mg_2Si : Mg_2Sn = 3:7. XRD results are in Figure 32 and thermal conductivity results are in Figure 33a and Figure 33b, followed by power factor and ZT of two selected samples in Figure 33c and Figure 33d. XRD results of sample A and B demonstrates the separate sets of peaks for Mg_2Sn at lower angles and Mg_2Si at higher angles owing to the difference in lattice constant as mentioned earlier: 6.77 Å for Mg_2Sn and 6.39 Å for Mg_2Si. It is noted that the peaks of Mg_2Si are less pronounced because of

less number of atoms as well as higher melting temperature, which should result in smaller grain size compared to that of Mg_2Sn after sintering at the identical temperature. By looking at XRD results of C and E compared with B it is possible to confirm that, by either ball milling or post annealing, Si and Sn atoms are mixed well in the scale detectable through XRD so as to shows the single set of peaks. Other samples also exhibit a single set of peaks of which locations are in between that of Mg_2Sn and Mg_2Si, similar to the reference sample H made by using high energy ball milling of Si and Sn altogether from the beginning as samples in Figure 30. Although the converging trends of separate peaks with post treatment seems contradictory to Mg_2Sn-Mg_2Si system's immiscible nature[33,36,38,39,67,] , which prevents binary material system to form a solid solution, it cannot be assured that this observation by itself means the absence of thermodynamic miscibility gap because the two phases might not be detected through XRD in case the pattern is too fine to make the noticeable lattice constant difference. Also coherently formed interface between two phases is also able to induce the continuous change in lattice constant spatially so that separate peaks might not be observable, but just broadened peaks with larger full width half maximum. This aspect of material kinetics and thermodynamics is out of the main focus of this work and warrants further investigation.

Label	Ball milling (min)	Post annealing (hours)	Electrical conductivity at RT (S/cm)	Density (%)
A	2.5	0	2590	99
B	5	0	2690	100
C	5	10	2210	91
D	30	3	2190	96
E	50	0	2030	97
F	50	0.05	2710	95
G	50	3	2220	96
H	N/A, $Mg_2(Si_{0.3}Sn_{0.7})_{0.98}Bi_{0.02}$		1890	101

Table 5. List of samples for Mg_2Sn: Mg_2Si = 7:3 doped with 2% of Bi

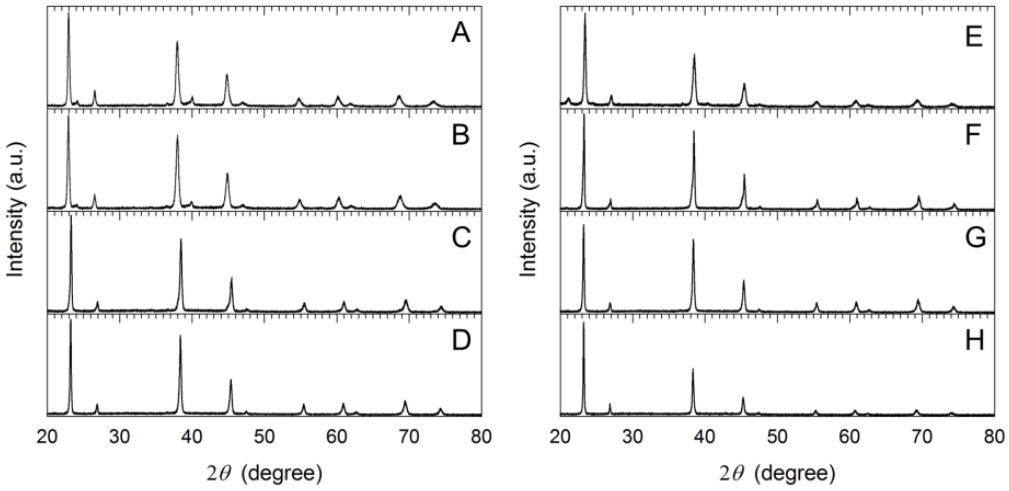

Figure 32. XRD results of samples A ~ H

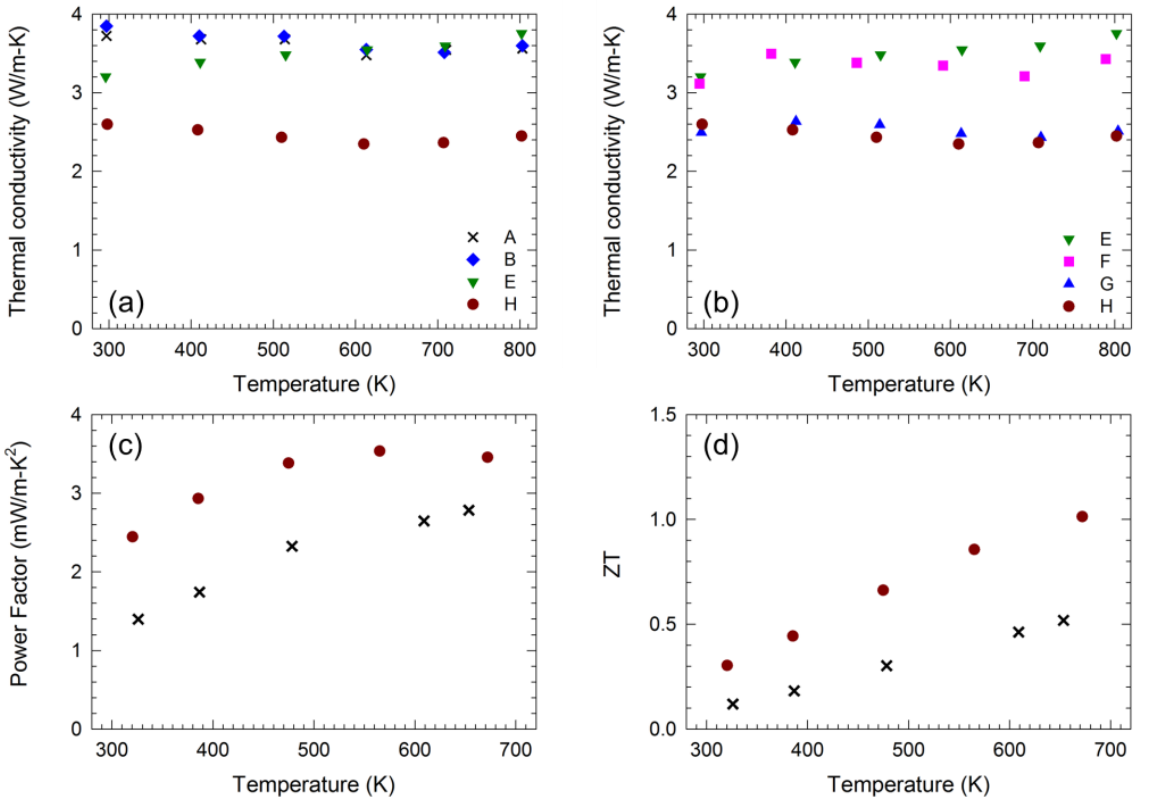

Figure 33. Thermal conductivity of samples. (a) ball milling time effect A, B, and E, (b) post annealing time effect E, F, and G, (c) PF of A and H, and (d) ZT of A and H.

Figure 33a and Figure 33b show the measured thermal conductivities of the sample A, B, E, F, G, and H. As shown in Figure 33a the mixing of two types of powder by ball milling from 2.5 min to 50 min doesn't make noticeable difference except for around 300 K as much as 0.5 W/m-K. Considering the electrical conductivity reduction from 2590 to 2030 S/cm caused by carrier's alloy scattering it can be concluded that the ball milling time doesn't help much for lowering lattice thermal conductivity by phonon's alloy scattering, although XRD data of E exhibits the single set of peaks, which is a clear difference from that of A (or B). Meanwhile Figure 33b, samples with varying post annealing time from 0 to 3 hours, demonstrates the protruding contrast. The thermal

conductivity is dropped by about 1 W/m-K from sample E to sample G through the entire temperature range from 300 K to 800 K, of which difference can be interpreted as lattice thermal conductivities' difference inasmuch as electrical conductivity difference of 190 S/cm can produce the electronic thermal conductivity of 0.15 W/m-K at most with Wiedemann-Franz law. The thermal conductivity of G is almost approaching that of H, which was prepared by mixing Si and Sn with the same ratio of 3:7 from the beginning of powder preparation so that phonon is fully under the influence of scattering by randomly placed Si and Sn atoms, and comparable to values reported by literature[68]. In short, Figure 33a and Figure 33b shows the obvious picture of reducing lattice thermal conductivity as Si and Sn atoms' degree of mixing increases so as to maximize the phonon scattering by alloys. Now Figure 33c reveals the influence toward electrical property, more specifically PF for thermoelectric application. The enhancement in PF from less mixed sample A to well mixed sample H is as much as 30% so that the difference in ZT, which has PF in numerator and k in denominator, in Figure 33d takes the effect from both aspects: thermal and electrical and shows the huge difference as much as 60%.

4.4 Conclusions

In order to investigate this phenomenon more especially in PF, possibly due to valley convergence and has not drawn much attention before by researchers, systematically with the optimized doping level so as to produce the highest ZT, another set of samples with proper doping level needs to be prepared. Through the systematic

study on thermoelectric ZT as a function of the degree of mixing in $Mg_2Si_{0.3}Sn_{0.7}$, concrete conclusion can be made. Also pellet samples need to be prepared with different ratio of Sn and Si so as to obtain more concrete conclusion whether miscibility gap is truly terminated in the samples prepare by high energy ball milling, hence achieving the desired solid solution favorable for stable and reliable thermoelectric power generation.

CHAPTER V

IMPROVEMENT IN THERMOELECTRIC ZT BY THERMODYNAMIC EVOLUTION BEYOND THE MISCIBILITY GAP IN Mg_2Sn : Mg_2Si COMPOSITE

5.1 Introduction

Thermoelectric power generation is one of the promising techniques as the global demand for renewable energy is growing recently. Also the nature of thermoelectrics that utilizes the redundant heat into useful electricity enables the energy harvesting in various circumstances accompanying continuous heat dissipation such as wearable electronics, Internet of Things (IoT), *etc.* Among several rare-earth heavy atom material systems, such as bismuth telluride, lead telluride, *etc.*, the thermoelectric figure of merit (ZT), which is the key factor determining thermoelectric power conversion efficiency, has been found to be significant. Due to the recent state-of-the-art nano technologies there has been remarkable progress toward the improvement of material's ZT in recent 10 years[5,10,11,23-25,69-75] so as to focus more on other aspects such as module level integration[76-79], environmental friendliness[20,22,80], material cost[81-83] and so forth.

Magnesium silicide[35,52,65,84-91] is an emerging thermoelectric material owing to its light weight, non-toxicity and affordable cost since magnesium and silicon are abundant on earth. Moreover when another atom substituting the silicon in the same group such as tin or germanium replaces the silicon atom at a certain amount it forms the alloy system whose chemical formula is $Mg_2Si_{1-x-y}Sn_xGe_y$. This alloyed structure induces, in addition to the phonon scattering in shorter wave length range[12,14,19,92], the modification in

electronic structure of the material system such that the energy level difference between valleys is rearranged and converged[68,93,94] to the level of several k_BT so as to maximizing the power factor (PF = $\sigma \times S^2$), one of the building blocks determining ZT = (PF × T) / k, where σ, S, k, and T are electrical conductivity, thermopower, thermal conductivity, and the absolute temperature. This enhancement in PF as well as the depression in thermal conductivity at a certain combination of aforementioned x and y is clearly the phenomena beyond the well-known explanation for composite materials[95], which is simply explained by the averaged material property by individual's volume percent. It should be noted that this phenomenon can happen only from the portion that is homogeneous microscopically and sometimes in atomic level such that each type of carrier, *e.g.*, phonon as heat carrier and electron as charge carrier, can sense the mixing ratio among each type of atoms within the range of its wavelength[3].

In this regard it is important to have a thermoelectric material sample with fully alloyed elements, which is the ideal situation and hard to achieve because typical material preparation is from the individual raw material powders so that the variation of the atoms' composition in the microscopic level is inevitable unless the extreme amount of time and cost for the process is invested. Moreover some of the thermoelectric material systems such as $Mg_2Sn_xSi_{1-x}$ is known to have a thermodynamic issue of miscibility gap between Si and Sn atoms so that it is more prone to have non-fully alloyed phases of Si-rich or Sn-rich[33,36,38,67]. The deviation in the reported peak ZT of $Mg_2Sn_xSi_{1-x}$, where $0.55 < x < 0.7$, among researchers ranging from 1.0 to 1.5[31,56,96] might be attributed to this issue, although no one has performed a systematic study to

investigate the interrelation. Therefore the investigation on the correlation of the homogeneity to the thermoelectric performance and the accurate phase diagram of Mg_2Sn-Mg_2Si system, with the emphasis on the miscibility gap, would enlighten the future direction toward the practical aspects including the tolerance in degree of mixing for acceptable material property, corresponding process condition, and the optimum window in view of the trade-off between the thermoelectric performance and the required process cost.

In this work using Mg_2Sn[66,97-99] and Mg_2Si[65] powder prepared separately as a source we investigated the existence of miscibility gap, electrical conductivity, thermopower, thermal conductivity, and ZT with bulk pellet samples made by various ratios of Sn:Si and process conditions for controlling the degree of mixing between Sn and Si atoms.

5.2 Experimental

We prepared Mg_2Si and Mg_2Sn powder heavily doped with 1.5 at. % bismuth for the optimum thermoelectric performance[56] by high energy ball milling (Spex SamplePrep 8000M)[65] Mg turning (99.9%, Across organics), Si powder (99.999%, -100+325 mesh, Alfa aesar), Sn powder (99.8%, -325 Mesh, Alfa aesar), and Bi powder (99.9%, Strem chemicals) with stainless steel balls and vial for 10 hours. As shown in the upper two plots in Figure 34, the resultant powder shows the majority of the powder to be Mg_2Si or Mg_2Sn with some impurities of residual Mg, Si, and Sn. Nevertheless after current-assisted sintering of the proper amount of powder (0.38 or 0.6 g) at 750 or

600 ºC for 200 seconds the pellets with the density higher than 98% of the theoretical density (2.0 g/cm^3 or 3.59 g/cm^3, respectively) and proper mobility[65,66] at room temperature ranging from 80 to 100 cm^{2}V^{-1}s^{-1} from Hall effect measurements were obtained. The lower two plots in Figure 34 also show the clear and sharp peaks of Mg_2Si and Mg_2Sn implying the purity of samples made from high energy ball milling elemental powders[100-103] followed by current-assisted sintering. Both samples' ZT values are also in good agreement with literature as can be found in Figure 35.

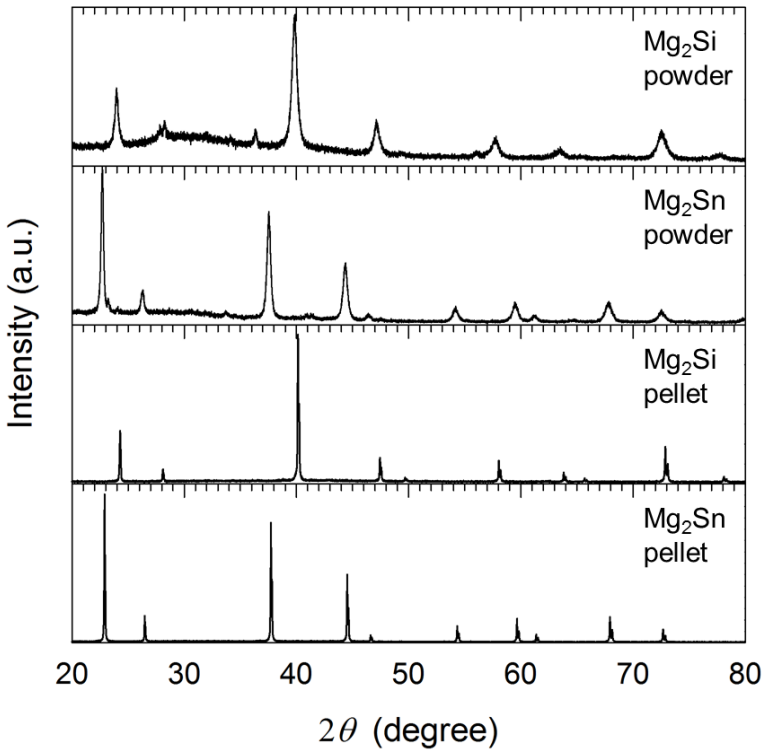

Figure 34. XRD results of synthesized Mg_2Sn and Mg_2Si powders and pellets after current-assisted sintering.

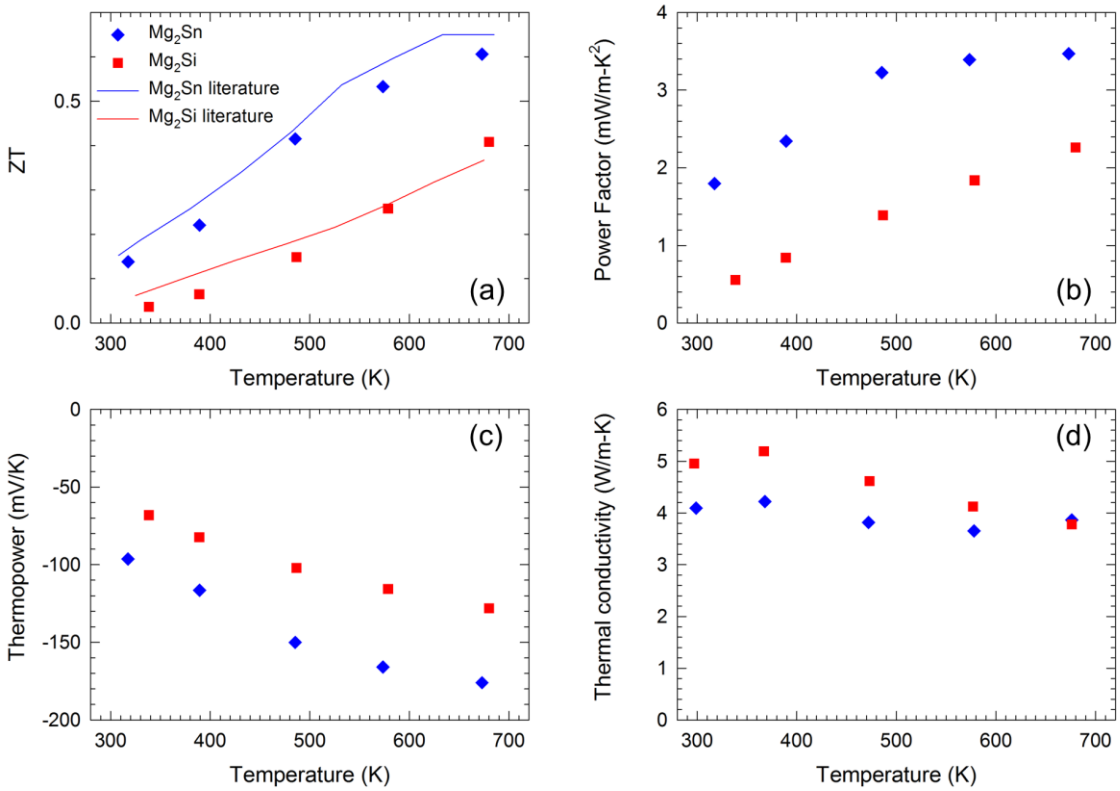

Figure 35. Thermoelectric properties of $Mg_2Sn_{0.985}Bi_{0.015}$ and $Mg_2Si_{0.985}Bi_{0.015}$; (a) ZT, (b) PF, (c) thermopower, and (d) thermal conductivity.

Afterwards each powder with the weight ratio of w_{Si} : w_{Sn} = 1: (0.9~5.0) so as to achieve the desired stoichiometry of from $Mg_2Sn_{0.3}Si_{0.7}$, which is at the center of miscibility gap in Mg_2Sn-Mg_2Si binary system's phase diagram[67], to $Mg_2Sn_{0.7}Si_{0.3}$, well known to have the best ZT among $Mg_2Sn_xSi_{1-x}$ solid solutions[56], was put together into a stainless-steel vial and high energy ball milled for up to 50 minutes as shown schematically in Figure 36. Then the mixed powder of 0.46 ~ 0.55 g was loaded into a half-inch diameter graphite die and current-assisted sintering was performed at 720 ~ 650 ^oC for 200 seconds. Finally the graphite die and punch set including the pellet inside

was transferred to a 2 inch diameter tube furnace for post annealing at the temperature same as that of sintering process up to 12 hours in vacuum. Through this strategy the sublimation and/or oxidation of Mg was prevented while exposing the pellet for a long period of time.

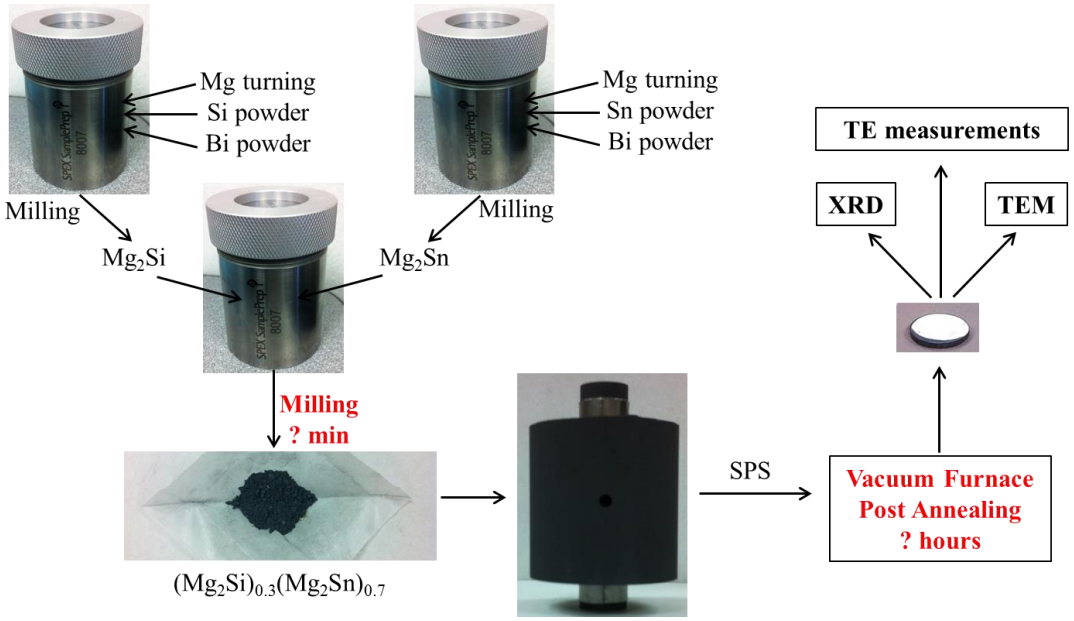

Figure 36. Schematic of sample preparation from the elemental raw powder to macroscopic bulk pellet.

The synthesized pellet was polished with sand papers in order to have both faces flat and shiny followed by electrical conductivity and Hall effect measurement at the room temperature with the circular shape. Thermal conductivity was obtained as k=DρC, where D is the thermal diffusivity measured by Xe-flash setup (TA instrument FL3000), ρ is the density measured using Archimedes method, and C is the specific heat adopted from literature[33,66,104]. For the measurement of thermopower and electrical conductivity as a function of temperature the pellet was cut into a bar whose dimension is 1.3 × 5 ×

11 mm^3 using diamond saw and mounted to our custom-made setup, capable of measurements at temperatures ranging from 30 to 400 ^oC.

5.3 Results and discussion

5.3.1 Phase evolution in Mg_2Sn : Mg_2Si = 3:7 inside miscibility gap

Table 6 shows the list of samples prepared by mixing Mg_2Sn and Mg_2Si powder with the ratio of 3:7 so that the composition is placed at the exact center of miscibility gap in Mg_2Sn-Mg_2Si binary material system and the clearly separated phases of $Mg_2Sn_{0.55}Si_{0.45}$ and $Mg_2Sn_{0.1}Si_{0.9}$ can be obtained[67] as they go through mixing and thermal processing at around 700 ^oC. XRD results in Figure 37 show the trend of phase evolution as it goes through more mixing and heat treatment by post annealing.

Label	Ball milling (min)	Post annealing (hours)	Electrical conductivity at RT (S/cm)	Density (%)	Carrier concentration (10^{20} cm^{-3})
P169	0.1	0	1790	102	2.35
P172	2	0	1510	102	2.28
P174	4	0	1420	102	2.11
P170	2	3	1620	96	1.90
P173	4	7	1870	97	2.78

Table 6. List of samples for Mg_2Sn: Mg_2Si = 3:7 doped with 1.5% of Bi

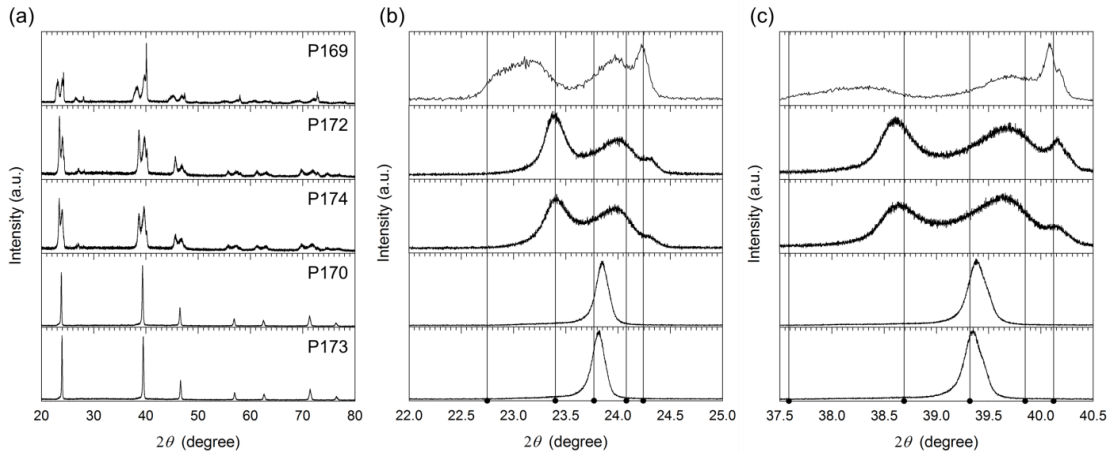

Figure 37. XRD results of (a) samples in Table 1, (b) detailed analysis using the peak from (111)-plane, and (c) detailed analysis using the peak from (220)-plane. Five vertical lines correspond to the peak locations for various Si:Sn ratio: Mg_2Sn, $Mg_2Sn_{0.55}Si_{0.45}$, $Mg_2Sn_{0.3}Si_{0.7}$, $Mg_2Sn_{0.1}Si_{0.9}$, and Mg_2Si.

Surprisingly, as shown in Figure 37a, pairs of peaks are unified into a single set of peaks as more mixing and post annealing were done, entirely opposite to what the phase diagram in literature claims[33,36,38,67]. Detailed analysis is possible using the narrow angle-scanned diffraction data for major two angle locations: (111) at 22.747 ~ 24.241 as shown in Figure 37b and (220) at 37.587 ~ 40.121 as shown in Figure 37c. The first sample, P169, with little mixing just for 0.1 min shows the well-expected outcome with distinct two peaks from Sn-rich phase and Si-rich phases. In Figure 37b it should be noted that the peak for (111) of Mg_2Si at 24.241 still remains as the strongest peak among others due to insufficient time of mixing and high melting point of Mg_2Si (~1085 ^oC) compare to process temperature (720 ^oC). However it can be found that Mg_2Sn doesn't remain as it is in view of the shifted XRD peak to ~ 23.1. Due to lower melting point of Mg_2Sn (778 ^oC) as well as less amount in volume compared to Mg_2Si, it is highly probable that all Mg_2Sn was softened and wrapping the outer surface of Mg_2Si

particles with coherent lattice matching so that the corresponding peaks for two distinct phases around the coherent interface are in strain making the peak shifts. As a result, the peak of Mg_2Sn at ~23.1 implies the compressive strain and the peak of Mg_2Si at ~24.0 is from tensile-strained portion. By observing the next two samples, P172 and P174, it is notable that the pristine peak of Mg_2Si at 24.241 weakened a lot while the corresponding peaks for Sn-rich phase and Si-rich phase are protruding. It is interesting that the two peaks at ~23.4 and ~24.1 match the precipitating phases ($Mg_2Sn_{0.55}Si_{0.45}$ and $Mg_2Sn_{0.1}Si_{0.9}$) according to the phase diagram in literature. Nevertheless the samples P170 and P173, which are after post annealing for 3 and 7 hours, show the unified single peak in a good agreement with the theoretically calculated peak position at 23.75 for $Mg_2Sn_{0.3}Si_{0.7}$, which might indicate the absence of miscibility gap due to some reasons such as the suppression of miscibility gap by the coherent interfaces stemming from the nature of the powder prepared by high energy ball milling. Figure 37c from (220) planes also demonstrates the similar phenomena consistent with that of (111) planes in Figure 37b.

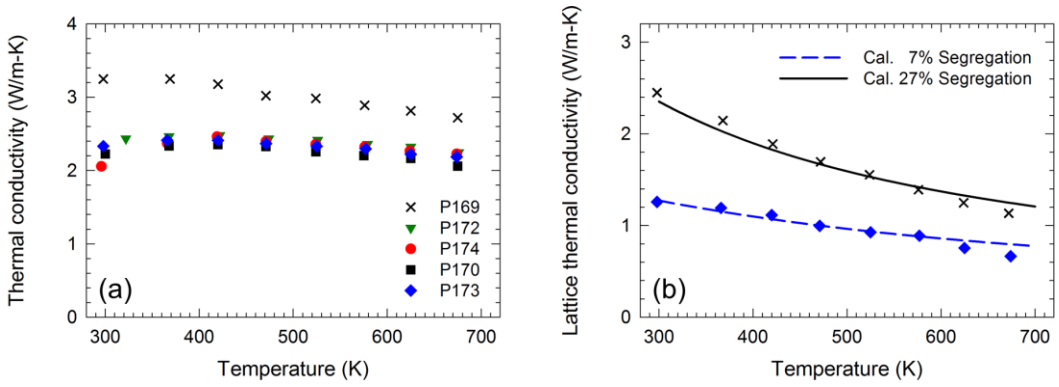

Figure 38. (a) Thermal conductivity of samples and (b) lattice thermal conductivity with calculation results.

Measured thermal conductivity results are shown in Figure 38a from room temperature to 400 ^{o}C. P169 with the least effort of mixing shows the highest thermal conductivity, which is the well expected result in view of the alloy scattering in phonon[14,92]. The extracted lattice thermal conductivity results after subtracting the electronic thermal conductivity portion using Wiedemann Franz law[27,56] are available in Figure 38b. Due to the large band gap of $Mg_2Sn_{0.3}Si_{0.7}$ and heavy doping level bipolar thermal conductivity can be assumed negligible. The lattice thermal conductivity results nicely demonstrate the reduction with more mixing and longer post annealing time. The samples with 2 min and 4 min mixing without post annealing show the medium level of thermal conductivity, which is in between that of least mixed sample (P169) and that of post annealed samples (P170 and P173). The fact that the lattice thermal conductivity values of P170 and P173 show marginal difference, although P173 has slightly smaller thermal conductivities, implies that the material system evolution with post annealing is almost saturated just after 3 hours of post annealing. The highest (P169) and lowest (P173) data points were fitted using a modified Callaway model for phase segregated material system, developed in Chapter 3[18]. According to the fitting the sample with the most distinct two phases (P169) has 27% of non-mixed portion out of the entire volume. Although the sample was prepared by crude mixing just for 6 seconds and the appearance of the clearly polished face shows distinct phases in bare eyes (not shown here), just 27% of its entire volume remains as unmixed phases. However it can be regarded as consistent in view of XRD results (shifted peak of Mg_2Sn) and the lattice thermal conductivity at 400 ^{o}C, which is smaller than 2 W/m-K, impossible to achieve

using a simple rule-of-mixture of Mg_2Sn and Mg_2Si's value from Figure 35d. During 200 seconds of current-assisted sintering, not only the densification of the pellet, but also 73% of the entire volume might have formed the solid solution. The sample with the best mixing / lowest thermal conductivity (P173) was fitted by 7% segregation curve. Although the thermal conductivity results are similar to reported values in literature[68] and single sharp peaks are observed in XRD, it might imply that 7% of the entire volume still remains as unmixed phases with good coherency between phases so that no distinct XRD peaks are detectable.

5.3.2 Similarity in Mg_2Sn : Mg_2Si = 4:6 and 5:5

Similar experiments with different Sn:Si ratios (4:6 and 5:5) which are still in miscibility gap of phase diagram were performed and identical trend was observed as shown in Figure 39 for XRD results and Figure 40d for thermal conductivities. Although it is less likely that the entire Sn and Si atoms are homogeneously mixed with short period of mixing and post annealing, it can be clearly concluded that the major direction of thermodynamic evolution in our samples is toward the better mixing. And it seems that the degree of mixing is the level in which possible separate phases cannot be detected in the scope of XRD, approaching the solid solution rather than the macroscopically separated two phases, which appears to be beyond the conclusion of literature[67].

Label	Ball milling (min)	Post annealing (hours)	Electrical conductivity at RT (S/cm)	Density (%)
$Mg_2Sn_{0.4}Si_{0.6}$ Segregated	0.1	0	1530	102
$Mg_2Sn_{0.4}Si_{0.6}$ Less segregated	7	10	1530	96
$Mg_2Sn_{0.5}Si_{0.5}$ Segregated	0.1	0	1590	101
$Mg_2Sn_{0.5}Si_{0.5}$ Less segregated	2	3	1510	96

Table 7. List of samples for Mg_2Sn : Mg_2Si = 4:6 and 5:5

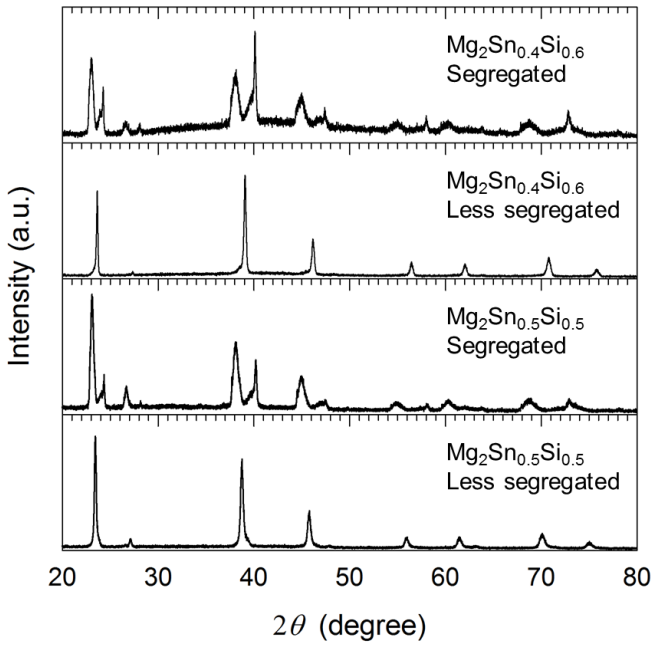

Figure 39. XRD results of Segregated $Mg_2Sn_{0.4}Si_{0.6}$, Less segregated $Mg_2Sn_{0.4}Si_{0.6}$, Segregated $Mg_2Sn_{0.5}Si_{0.5}$, and Less segregated $Mg_2Sn_{0.5}Si_{0.5}$.

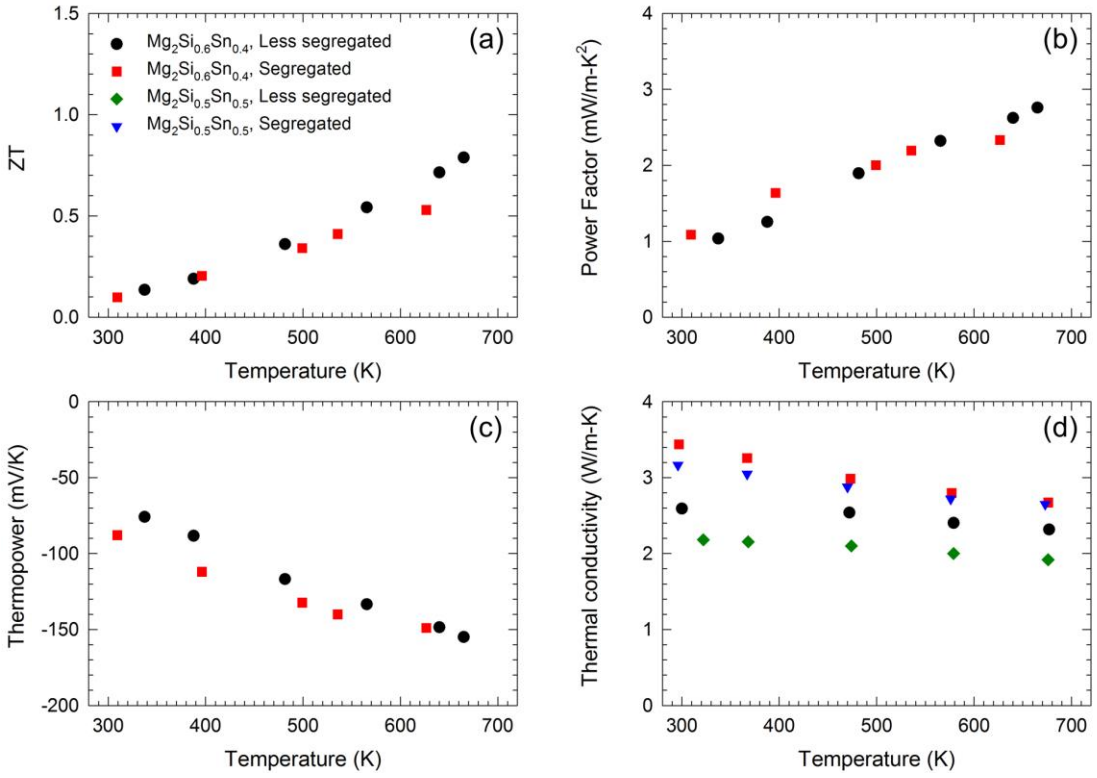

Figure 40. Thermoelectric properties of segregated / less segregated $Mg_2Si_{0.6}Sn_{0.4}$ and $Mg_2Si_{0.5}Sn_{0.5}$ samples. (a) ZT, (b) power factor, (c) thermopower, and (d) thermal conductivity.

5.3.3 Unveiled miscibility gap after 50 hours of annealing

To verify the presence or absence of miscibility gap, a longer time of annealing up to 50 hours was tried and the separated pairs of peaks in XRD were able to be detected (Figure 41) possibly due to the grain growth of each phase, which enhances the diffraction intensity out of noise level. Nevertheless the lattice thermal conductivity (Figure 42) doesn't increase, but rather decreased further, which is the beneficial feature for thermoelectric application. It is likely that the decomposed phases form fine lamella

structures so as to efficiently scatter phonons fully compensating the loss of alloy scattering by decomposed phases, which requires further exploration in the future.

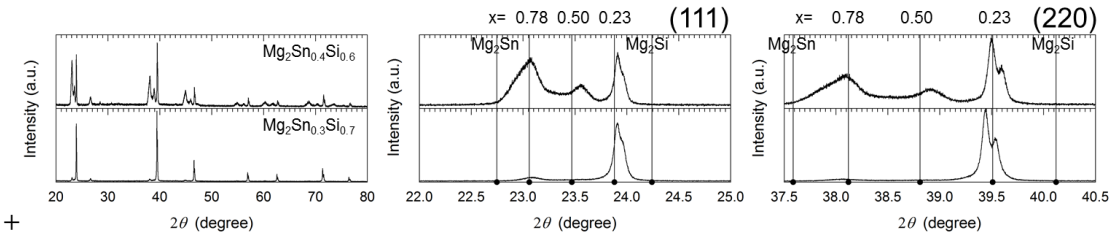

Figure 41. XRD results of $Mg_2Sn_{0.4}Si_{0.6}$ and $Mg_2Sn_{0.3}Si_{0.7}$ samples after 50 hours of annealing. Vertical guidelines correspond to the theoretical lattice constant depending on Sn contents (1, 0.78, 0.5, 0.23, and 0).

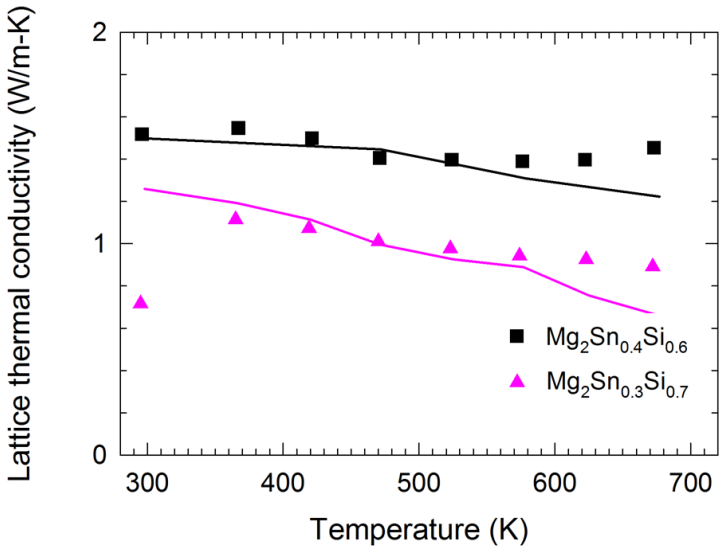

Figure 42. Thermal conductivity of samples after 50 hours of post annealing. Solid lines represent the lattice thermal conductivity of samples "$Mg_2Sn_{0.4}Si_{0.6}$ Less segregated" and P173 for comparison.

5.3.4 Valley convergence in Mg_2Sn : Mg_2Si = 7:3

In order to further investigate whether this observation beyond the miscibility gap is favorable toward real application in thermoelectrics, the samples with the ratio of Sn:Sn = 7:3 for the best ZT was prepared as shown in Table 8.

Label	Ball milling (min)	Post annealing (hours)	Electrical conductivity at RT (S/cm)	Density (%)	Carrier concentration (10^{20} cm^{-3})
P155	0.1	0	2160	101	2.3
P151	10	0	1900	100	2.2
P153		0.25	2020	98	2.1
P156		7	2150	97	2.3

Table 8. List of samples for Mg_2Sn: Mg_2Si = 7:3 doped with 1.65 % of Bi.

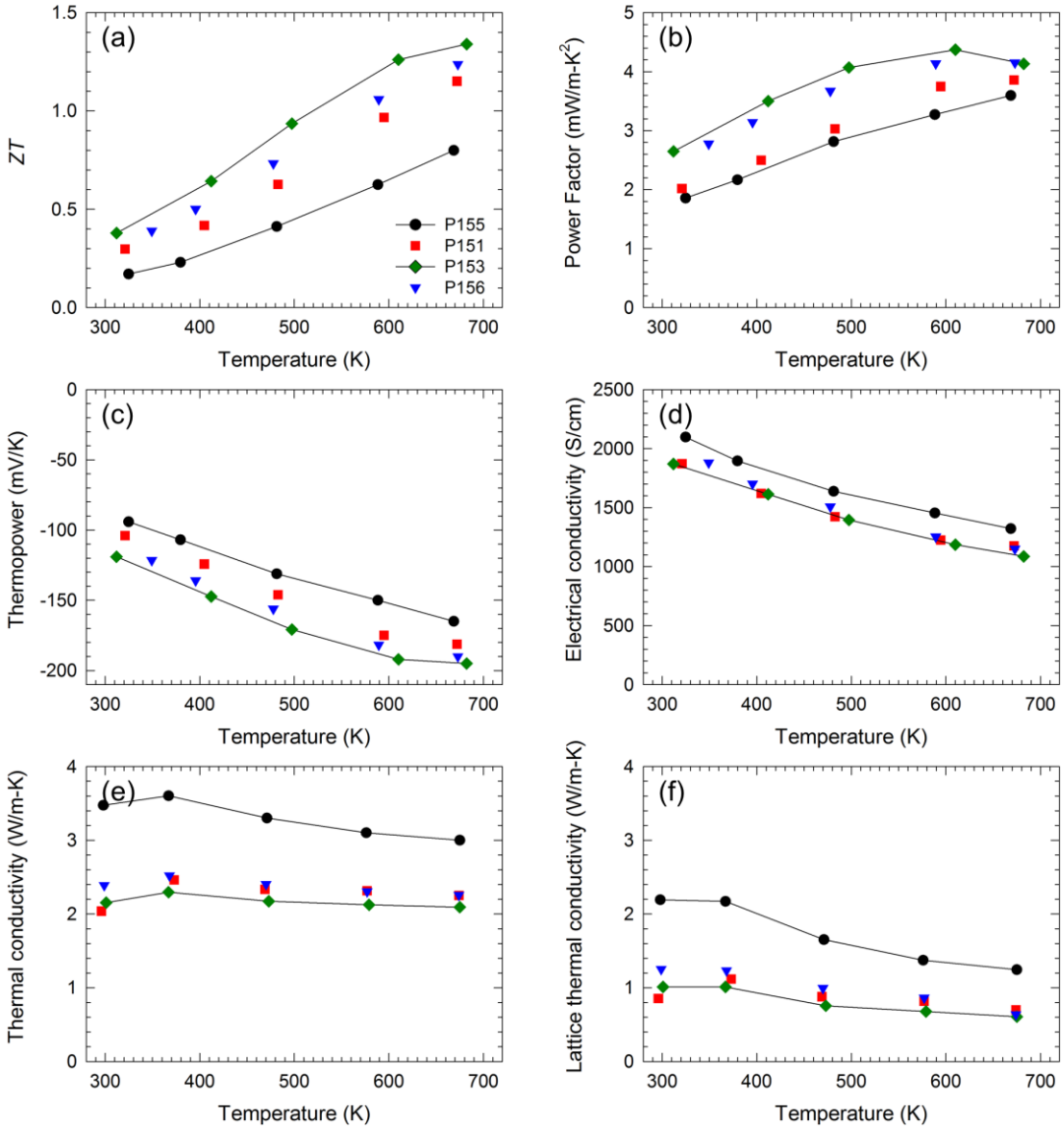

Figure 43. Thermoelectric properties of Bi 1.65% samples. (a) ZT, (b) PF, (c) thermopower, (d) electrical conductivity, (e) thermal conductivity, and (f) lattice thermal conductivity. Solid lines for Sample P155 and P153 are for guiding eyes.

Figure 43 shows ZT of sample P155, P151, P153, and P156 in (a), followed by the ingredient composing the ZT such as PF, thermopower, electrical conductivity, thermal conductivity, and estimated lattice thermal conductivity from (b) to (f)

accordingly. Here P155 was made from the powder slightly mixed together to obtaine the similar trend as P169 in Table 6. whereas the other 3 samples were prepared to achieve a better degree of mixing by high energy ball milling for 10 min. The surface of well-polished P155 has also noticeable difference, as in P169, in bare eyes such as less shiny appearance with segregated portions, some of which has the scale of larger than 100 um (not shown here). Similar to what we observed in P169, the minimally mixed P155 seems to have some portion with solid solution in view of its lattice thermal conductivity, power factor, and ZT. For example, considering the ZT ~ 0.6 and 0.4 of our Mg_2Sn and Mg_2Si samples (Figure 35), the ZT of P155 already exceeds the average ZT from Mg_2Sn and Mg_2Si. Although the pellet was prepared from the powder by crude mixing, it is likely that Sn and Si atoms are mixed during current-assisted sintering and cannot preserve 100% separation of each phase. Nevertheless the trend of enhancement in ZT is clear as more effort is put for better mixing from P155 to P156 so that the ZT is increased as much as 40% from 0.9 of P155 to 1.3 to P153. This huge enhancement in ZT from “pseudo composite” to “pseudo solid solution” is attributed to two factors: enhancement in PF and reduction in lattice thermal conductivity as shown in Figure 43b and Figure 43f. The reduction in lattice thermal conductivity is due to the enhanced alloy scattering, which is consistent to the results in literature[68].

Meanwhile the enhancement in PF can be investigated by disassemble the component into thermopower and electrical conductivity as shown in Figures 43c and 43d. The main contribution is from thermopower in Figure 43c showing the gradual enhancement from P155 to P156 due to growing portion of solid solution, which elevate

the total density of states in conduction band[23,68,94], out of separate two phases. However the reduction in electrical conductivity was marginal and less significant compared to our initial hypothesis. For example, sample P155 has much more deviation from the linear trend of electrical conductivity as a function of $T^{1.5}$ especially near room temperature compared to other samples, implying the additional scattering mechanism to commonly dominant acoustic phonon scattering[18,50]. Since this additional scattering in charge carrier is unfavorable direction for thermoelectric application, this would not worth investigating or modeling more in detail. The energy barrier in conduction band between two phases owing to the difference in DOS might be one possibility. P156 has slightly lower ZT compared to 2C, which might be not meaningful as the difference is marginal and within the error range.

Figure 44 shows the thermopowers of P153, P155, Mg_2Sn and Mg_2Si fitted with the calculated thermopower with the assumption of acoustic phonon as the dominant scattering mechanism to catch the idea that samples' density of states (DOS) effective mass increases from individual component (Mg_2Sn or Mg_2Si) to well-mixed $Mg_2Sn_{0.7}Si_{0.3}$ solid solution (P153). Fitted thermopower as a function of temperature well matches the experiment results, implying that the electronic structure of $Mg_2Sn_xSi_{1-x}$ can be well modeled using the assumption of parabolic band with constant effective mass over temperatures. The corresponding effective masses of a single valley from the best fitting are denoted in the legend for 4 different samples. $m^*/m_0 = 0.63$ and 0.5 for Mg_2Sn and Mg_2Si are in good agreement with literature[66,88,89]. As the material system undergoes mixing m^*/m_0 increases to 0.8 (P155) and eventually 1.1 (P153).

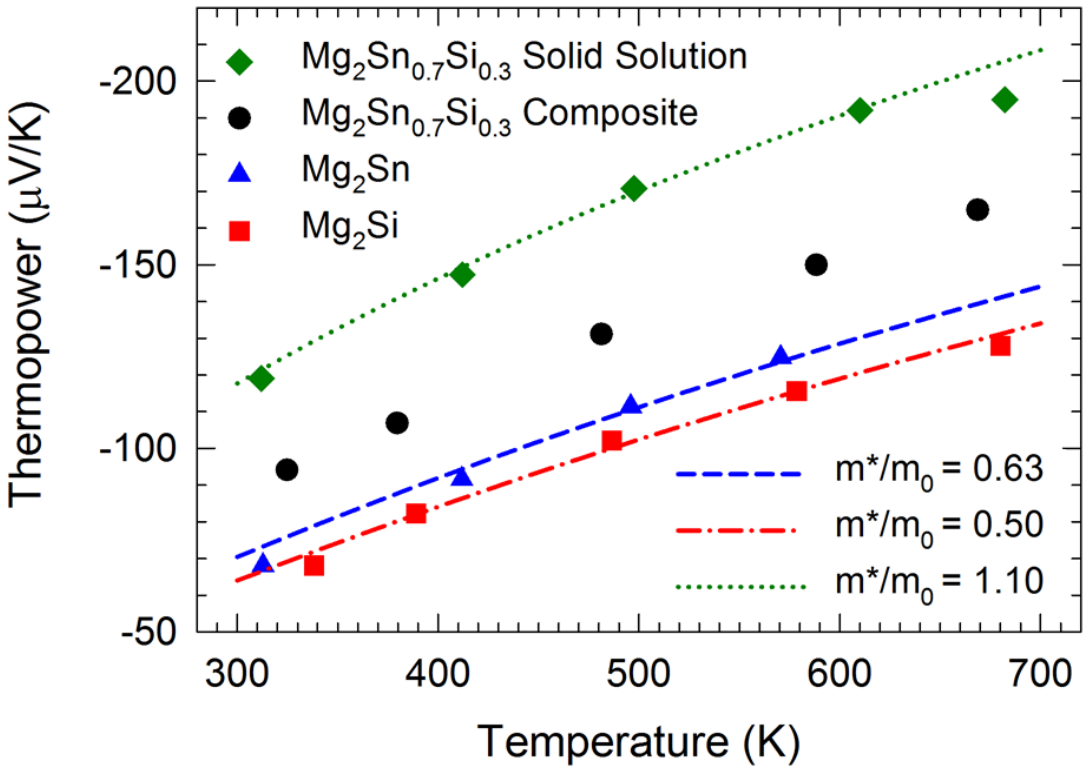

Figure 44. Thermopower of $Mg_2Si_{0.3}Sn_{0.7}$ (P153 and P155), Mg_2Sn, and Mg_2Si fitted by calculated thermopower with variable effective mass.

The enhancement beyond the typical rule-of-mixtures of Mg_2Sn-Mg_2Si composite system is clearly demonstrated in Figure 45 after additional thermoelectric measurements were performed for different ratio of Sn:Si such as $Mg_2Sn_{0.5}Si_{0.5}$ and $Mg_2Sn_{0.4}Si_{0.6}$ from which the consistent trend of increasing PF and decreasing k with a single set of peaks in XRD was observed. One major feature is that the best solid solution and ZT can be obtained after thorough mixing and post annealing as shown in Figure 45c. The reduction in thermal conductivity is demonstrated in Figure 45a with a clear distinction between less mixed and well mixed samples, which eventually depicts the well-known trend from alloy systems[67,92]. Meanwhile Figure 45b shows a somewhat

different trend that the improvement occurs in a narrower range of Mg_2Sn volumetric percent.

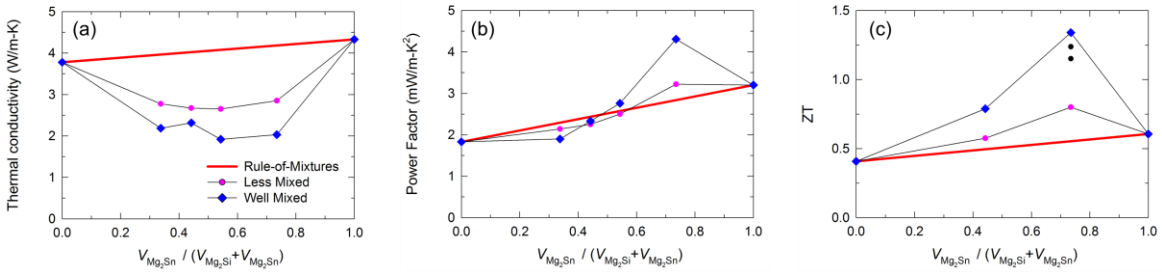

Figure 45. Overview for the change in (a) thermal conductivity, (b) power factor, and (c) ZT beyond the typical composite mixing rule.

This can be explained using the full width of half maximum (FWHM) of carrier's energy distribution in parabolic band with the variation of two corresponding edges' energy level for X3 and X1 valleys[68]. Because the energy distribution of carrier's energy which has the direct correlation to the energy distribution and Lorenz number is about 2 k_BT, the valley convergence effect can be activated only when the energy difference between two edges is less than 2 k_BT. According to the reported values in literature[50,68] for the energy difference between two edges, there is a very narrow window in terms of Sn content condition for having the energy difference within 2 k_BT. In order to validate the hypothesis a simple calculation with two parabolic valleys (X3 and X1) with the experimentally obtained effective mass (0.5 and 0.63 for m^*/m_0) and energy difference from literature[66], were performed to calculated the thermopower under the assumption of acoustic phonon dominant scattering.

The calculation results (dashed line with triangles) in Figure 46 as well as the experimental data (diamonds and circles) efficiently visualizes the enhancement of the DOS effective mass only in a narrow range of Sn ratio, $0.625 < x < 0.75$ in $Mg_2Sn_xSi_{1-x}$. Also the discrepancy in the maximum effective mass between experiment (1.1 m_0) and the calculation (0.9 m_0) implies that the enhancement in DOS effective mass doesn't come solely from the valley convergence between X3 and X1, but also from the valley broadening possibly due to orbital interaction as they get closer each other. This observation together with the peak power factor in Figure 45b constitutes an example showing the detrimental effect of broadened effective mass toward the electrical conductivity, hence power factor as shown in Eq. (5.1).

$$PF \propto \frac{N_V}{m^*} \tag{5.1}$$

The enhancement in N_V by a factor of 2, from 3 to 6, by converging X3 and X1 is partially offset by the enhancement in effective mass by a factor of 1.22 so as to the enhancement in PF ends up being 1.64 times, which has a good agreement with the maximum PF of 4.31 $mWm^{-1}K^{-2}$ in Figure 45b with respect to 2.84 $mWm^{-1}K^{-2}$ from the value from rule-of-mixtures.

In view of the scarcity of literature focusing on the effective mass[26,27] and that power factor enhancement in literature is always not as much as the enhancement in N_V exactly following the proportionality in Eq. (5.1), it should be noted that the enlargement in m^* is inevitable while valleys are being converged, which is the enhancement in N_V. And the careful attention, such as whether the valley undergoes the broadening, needs to be paid when implementing the valley convergence for higher PF.

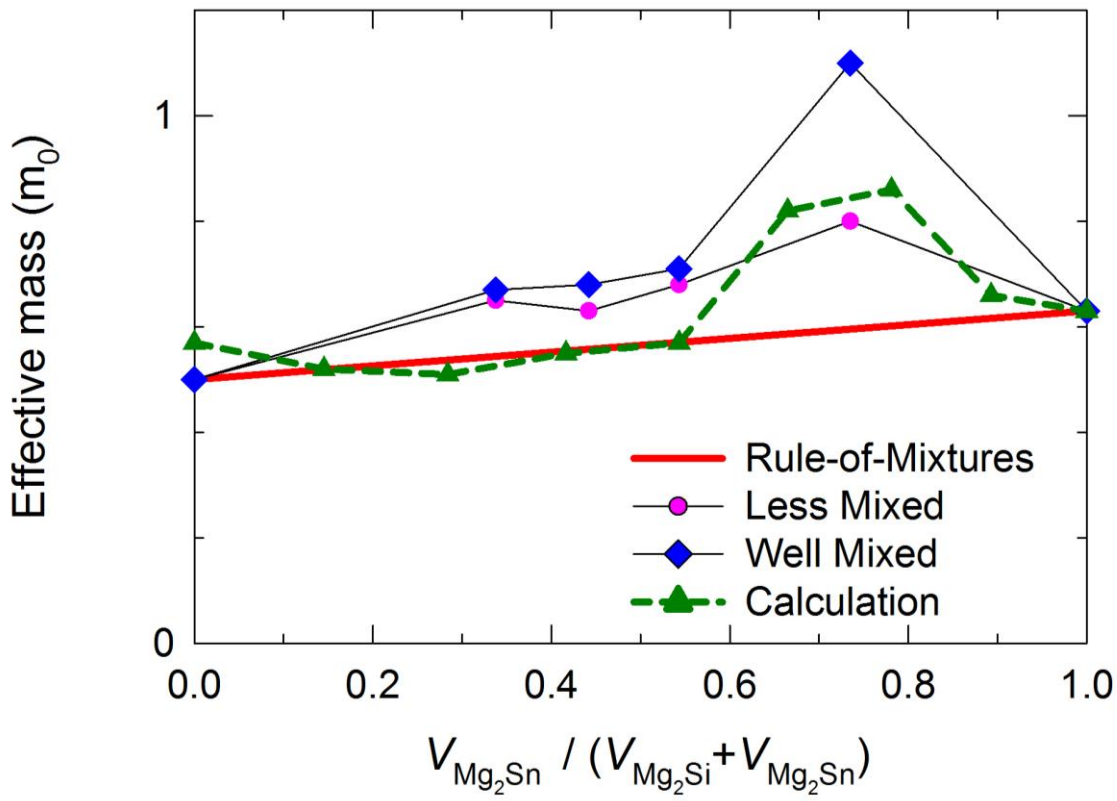

Figure 46. Overview for the change in effective mass beyond the composite mixing rule together with calculation results.

5.4 Conclusions

A series of experiments with various Sn:Si ratio from 3:7 to 7:3 post annealed for up to 50 hours was performed. Influence of probable phase segregations due to the miscibility gap turned out to be not as detrimental as the initial expectation. The lattice thermal conductivity stayed at the level of homogeneous solid solution even with the clearly separated pairs of peaks after 50 hours of post annealing, implying the introduced phonon scattering mechanism to compensate the loss of scattering from alloy. Therefore, together with the observation of single peaks in XRD results for samples annealed up to

10 hours, it is likely that the phase segregation in this work has much finer pattern comparable to the scale of phonon wave length. Meanwhile the sample in Chapter 3 prepared from the non-fully optimized solid state reaction might have much coarser segregations, which are not from the thermodynamic evolution but is attributed to the powder preparation process, so that the samples show much higher lattice thermal conductivities.

More interestingly it was found that the window of Sn:Si ratio is very narrow for having the valley degeneracy and power factor enhancement so that the phase homogeneity needs to be carefully maintained. Also the broadened effective mass plays a role of adversely affecting the power factor enhancement. This is an important message that the fine tuning and control of microstructure to maintain the optimum Sn:Si composition and track the change in single valley's effective mass is an essential step for pursuing the best ZT in thermoelectric material development not limited only for $Mg_2Si_{0.3}Sn_{0.7}$ but also other materials especially employing the alloy system.

CHAPTER VI

SUMMARY

The thermoelectric properties of magnesium silicide (Mg_2Si) - magnesium stannide (Mg_2Sn) solid solution with varying phase structure were investigated owing to its thermodynamically immiscible nature at a certain range of composition as well as the process dependency of the material structure. Boltzmann transport equation was used to derive the thermoelectric properties such as thermopower, electrical conductivity, and thermal conductivity so as to fit the experimentally measured properties. Especially, through the modeling of lattice thermal conductivity poor degree of mixing between Sn and Si with segregated phases as much as 60 % of the entire volume was deduced for the samples from non-fully optimized solid state reaction followed by 2 hours of post annealing at 700 ^{o}C, which brings about the reduced phonon scattering by randomly placed alloy atoms and enhanced lattice thermal conductivity from 0.5 W/m-K to 2.0 W/m-K followed by reduced thermoelectric figure of merit ZT from 1.4 to 0.9 at 500 ^{o}C compared to idealized material structure with 0 % of phase segregation.

As per the proposed direction from the modeling, samples with better phase homogeneity were pursued by high energy ball milling as an alternative process for sample preparation. The prepared sample with the new process showed the reduction in thermal conductivity as much as 1.4 W/m-K, almost approaching the suggested contrast from the model. The sample with the high energy ball milling also demonstrated its

excellent thermal stability maintaining its lattice thermal conductivity even after 18 hours of post annealing at 700 ^{o}C.

With the aid of successful powder preparation by high energy ball milling for heavily doped Mg_2Sn and Mg_2Si whose carrier concentrations are over 10^{20} cm^{-3} systematic studies with various Sn:Si ratios ranging from 3:7 to 7:3 for exploring the thermodynamic evolution of the constituent phases by various duration of post annealing from 0 to 50 hours. Although the phase segregation into Sn-rich and Si-rich phases was observed by the results of X-ray diffraction in $Mg_2Sn_{0.4}Si_{0.6}$ and $Mg_2Sn_{0.3}Si_{0.7}$ samples after 50 hours of post annealing, the lattice thermal conductivity was maintained as low as that of the idealized solid solution structure, which is beneficial for thermoelectric application.

Lastly the existence of the convergence between two valleys in conduction band at the certain Sn:Si ratio (~7:3) was demonstrated by controlling the degree of mixing through various time of powder mixing from 5 seconds to 10 minutes and post annealing from 0 to 7 hours. The power factor was enhanced from 3.4 mW/m-K^2 to 4.3 mW/m-K^2 at 300 ^{o}C as the degree of mixing was improved so as to achieve the increase in thermoelectric figure of merit ZT from 0.8 to 1.35 at 400 ^{o}C together with the effect in thermal conductivity reduction as well. It was also found that the valley convergence accompanies the effective mass broadening from 0.9 m_0 to 1.1 m_0 partially offsetting the improvement in power factor coming from the doubled number of valleys. The simulated effective mass enhancement by two-parabolic valley model as a function of Sn:Si ratio demonstrated the strictly narrow range for Sn:Si ratio to obtain the effect of

valley convergence, suggesting the importance of best degree of mixing and phase homogeneity.

REFERENCES

1 Zebarjadi, M., Esfarjani, K., Dresselhaus, M., Ren, Z. & Chen, G. Perspectives on thermoelectrics: from fundamentals to device applications. *Energy & Environmental Science* **5**, 5147-5162 (2012).

2 Heremans, J. P., Wiendlocha, B. & Chamoire, A. M. Resonant levels in bulk thermoelectric semiconductors. *Energy & Environmental Science* **5**, 5510-5530 (2012).

3 Vineis, C. J., Shakouri, A., Majumdar, A. & Kanatzidis, M. G. Nanostructured thermoelectrics: big efficiency gains from small features. *Advanced Materials* **22**, 3970-3980 (2010).

4 Bell, L. E. Cooling, heating, generating power, and recovering waste heat with thermoelectric systems. *Science* **321**, 1457-1461 (2008).

5 Snyder, G. J. & Toberer, E. S. Complex thermoelectric materials. *Nature materials* **7**, 105-114 (2008).

6 Laird_Technologies. *# 71035-506*.

7 iPhone_5. *3.8 V, 1440 mAh*.

8 Apple_Watch. *3.8 V, 205 mAh*.

9 Hicks, L. & Dresselhaus, M. Effect of quantum-well structures on the thermoelectric figure of merit. *Physical Review B* **47**, 12727 (1993).

10 Hochbaum, A. I. *et al.* Enhanced thermoelectric performance of rough silicon nanowires. *Nature* **451**, 163-167 (2008).

11 Poudel, B. *et al.* High-thermoelectric performance of nanostructured bismuth antimony telluride bulk alloys. *Science* **320**, 634-638 (2008).

12 Yi, S.-i. & Yu, C. Modeling of thermoelectric properties of SiGe alloy nanowires and estimation of the best design parameters for high figure-of-merits. *Journal of Applied Physics* **117**, 035105 (2015).

13 Lee, E. K. *et al.* Large thermoelectric figure-of-merits from SiGe nanowires by simultaneously measuring electrical and thermal transport properties. *Nano letters* **12**, 2918-2923 (2012).

14 Lee, J. W. *et al.* Core–shell Si 1− x Ge x nanowires with controlled structural defects for phonon scattering enhancement. *Journal of Materials Chemistry A* **2**, 12153-12157 (2014).

15 Hsu, K. F. *et al.* Cubic AgPbmSbTe2+ m: bulk thermoelectric materials with high figure of merit. *Science* **303**, 818-821 (2004).

16 Morelli, D., Heremans, J. & Slack, G. Estimation of the isotope effect on the lattice thermal conductivity of group IV and group III-V semiconductors. *Physical Review B* **66**, 195304 (2002).

17 Callaway, J. Model for lattice thermal conductivity at low temperatures. *Physical Review* **113**, 1046 (1959).

18 Tazebay, A. S. *et al.* Thermal Transport Driven by Extraneous Nanoparticles and Phase Segregation in Nanostructured Mg2 (Si, Sn) and Estimation of Optimum Thermoelectric Performance. *ACS applied materials & interfaces* (2016).

19 Lee, E. K. *et al.* Large Thermoelectric Figure-of-Merits from Si-Ge Nanowires by Simultaneously Measuring Electrical and Thermal Transport Properties. *Nano Lett.* **12**, 2918-2923, doi:10.1021/nl300587u (2012).

20 Wang, H. *et al.* Thermally Driven Large N-Type Voltage Responses from Hybrids of Carbon Nanotubes and Poly (3, 4-ethylenedioxythiophene) with Tetrakis (dimethylamino) ethylene. *Advanced Materials* **27**, 6855-6861 (2015).

21 Choi, K. *et al. Creating High Electronic Mobility Conduits by Hybridizing Polymers and Carbon Nanotubes for Large Thermoelectric Figure-of-Merits, Unpublished* (2014).

22 Wang, H., Yi, S. & Yu, C. Engineering Electrical Transport at the Interface of Conjugated Carbon Structures to Improve Thermoelectric Properties of Their Composites. *Polymer **97**,* 487 (2016).

23 Pei, Y. *et al.* Convergence of electronic bands for high performance bulk thermoelectrics. *Nature* **473**, 66 (2011).

24 Tang, Y. *et al.* Convergence of multi-valley bands as the electronic origin of high thermoelectric performance in CoSb3 skutterudites. *Nature materials* (2015).

25 Zhao, L.-D. *et al.* Ultrahigh power factor and thermoelectric performance in hole-doped single-crystal SnSe. *Science* **351**, 141-144 (2016).

26 Pei, Y., LaLonde, A. D., Wang, H. & Snyder, G. J. Low effective mass leading to high thermoelectric performance. *Energy & Environmental Science* **5**, 7963-7969 (2012).

27 Zhang, Q. *et al.* Low effective mass and carrier concentration optimization for high performance p-type Mg 2 (1− x) Li 2x Si 0.3 Sn 0.7 solid solutions. *Physical Chemistry Chemical Physics* **16**, 23576-23583 (2014).

28 Martin-Gonzalez, M., Caballero-Calero, O. & Diaz-Chao, P. Nanoengineering Thermoelectrics for 21st Century: Energy Harvesting and Other Trends in the Field. *Renew Sust Energ Rev* **24**, 288-305, doi:DOI 10.1016/j.rser.2013.03.008 (2013).

29 Rowe, D. M. *Thermoelectrics and its Energy Harvesting*. 40-3-40-12 (CRC Press, 2012).

30 Fedorov, M. I., Zaitsev, V. K. & Isachenko, G. N. High Effective Thermoelectrics Based on the Mg_2Si-Mg_2Sn Solid Solution. *Solid Compounds of Transition Elements* **170**, 286-292 (2011).

31 Gao, P. *et al.* Reduced Lattice Thermal Conductivity in Bi-Doped $Mg_2Si_{0.4}Sn_{0.6}$. *Appl Phys Lett* **105**, 202104-202101-202104-202105, doi:Artn 202104 Doi 10.1063/1.4901178 (2014).

32 Khan, A. U. *et al.* Thermoelectric Properties of Highly Efficient Bi-Doped $Mg_2Si_{1-X-Y}Sn_xGe_y$ Materials. *Acta Materialia* **77**, 43-53, doi:http://dx.doi.org/10.1016/j.actamat.2014.04.060 (2014).

33 Liu, W. *et al.* Enhanced Thermoelectric Properties of n-Type $Mg_{2.16}(Si_{0.4}Sn_{0.6})_{(1-y)}Sb_y$ Due to Nano-Sized Sn-Rich Precipitates and an Optimized Electron Concentration. *J Mater Chem* **22**, 13653-13661, doi:Doi 10.1039/C2jm31919e (2012).

34 Liu, W. *et al.* Enhanced Hole Concentration Through Ga Doping and Excess of Mg and Thermoelectric Properties of P-Type $Mg_{2(1+z)}(Si_{0.3}Sn_{0.7})_{(1-y)}Ga_y$. *Intermetallics* **32**, 352-361, doi:DOI 10.1016/j.intermet.2012.07.027 (2013).

35 Nolas, G. S., Wang, D. & Beekman, M. Transport Properties of Polycrystalline $Mg_2Si_{1-y}Sb_y$ ($0 \leq y < 0.4$). *Phys Rev B* **76** (2007).

36 Polymeris, G. S. *et al.* Nanostructure and Doping Stimulated Phase Separation in High-ZT $Mg_2Si_{0.55}Sn_{0.4}Ge_{0.05}$ Compounds. *Acta Materialia* **83**, 285-293, doi:DOI 10.1016/j.actamat.2014.09.031 (2015).

37 Zaitsev, V. K. *et al.* Thermoelectrics of n-Type with ZT > 1 Based on Mg_2Si-Mg_2Sn Solid Solutions. *ICT: 2005 24th International Conference on Thermoelectrics*, 189-195, doi:Doi 10.1109/Ict.2005.1519920 (2005).

38 Zhang, Q. *et al.* In Situ Synthesis and Thermoelectric Properties of La-Doped Mg_2(Si,Sn) Composites. *Journal of Physics D: Applied Physics* **41** (2008).

39 Zhang, Q. *et al.* High Figures of Merit and Natural Nanostructures in $Mg_2Si_{0.4}Sn_{0.6}$ Based Thermoelectric Materials. *Applied Physics Letters* **93** (2008).

40 Zhang, Q. *et al.* Thermoelectric Properties of n-Type $Mg_2Si_{0.6-y}Sb_ySn_{0.4}$ Compounds. *Physica Status Solidi (A) Applications and Materials Science* **205**, 1657-1661 (2008).

41 Zhang, Q., Zhu, T. J., Zhou, A. J., Yin, H. & Zhao, X. B. Preparation and Thermoelectric Properties of $Mg_2Si_{1-x}Sn_x$. *Phys. Scr., T* **T129**, 123-126 (2007).

42 Chen, L. X. *et al.* Miscibility Gap and Thermoelectric Properties of Ecofriendly $Mg_2Si_{1-X}Sn_x$ (0.1 <= X <= 0.8) Solid Solutions by Flux Method. *J Mater Res* **26**, 3038-3043, doi:Doi 10.1557/Jmr.2011.385 (2011).

43 Lan, Y. C., Minnich, A. J., Chen, G. & Ren, Z. F. Enhancement of Thermoelectric Figure-of-Merit by a Bulk Nanostructuring Approach. *Adv Funct Mater* **20**, 357-376, doi:DOI 10.1002/adfm.200901512 (2010).

44 Liu, W. *et al.* High Figure of Merit And Thermoelectric Properties of Bi-Doped $Mg_2Si_{0.4}Sn_{0.6}$ Solid Solutions. *J Solid State Chem* **203**, 333-339, doi:DOI 10.1016/j.jssc.2013.04.041 (2013).

45 Hatzikraniotis, E. *et al.* in *AIP Conference Proceedings.*

46 Jung, I.-H., Kang, D.-H., Park, W.-J., Kim, N. J. & Ahn, S. Thermodynamic Modeling of the Mg–Si–Sn System. *Calphad* **31**, 192-200, doi:http://dx.doi.org/10.1016/j.calphad.2006.12.003 (2007).

47 Viennois, R., Colinet, C., Jund, P. & Tedenac, J. C. Phase Stability of Ternary Antifluorite Type Compounds in the Quasi-Binary Systems Mg_2X-Mg_2Y (X, Y = Si, Ge, Sn) via Ab-Initio Calculations. *Intermetallics* **31**, 145-151, doi:10.1016/j.intermet.2012.06.016 (2012).

48 Liu, W. *et al.* Optimized Thermoelectric Properties of Sb-Doped $Mg_{2(1+z)}Si_{0.5-y}Sn_{0.5}Sb_y$ Through Adjustment of the Mg Content. *Chem Mater* **23**, 5256-5263, doi:Doi 10.1021/Cm202445d (2011).

49 Kim, S. L., Choi, K., Tazebay, A. & Yu, C. Flexible Power Fabrics Made of Carbon Nanotubes for Harvesting Thermoelectricity. *ACS Nano* **8**, 2377-2386 (2014).

50 Bahk, J. H., Bian, Z. & Shakouri, A. Electron Transport Modeling and Energy Filtering for Efficient Thermoelectric $Mg_2Si_{1-X}Sn_x$ Solid Solutions. *Physical Review B - Condensed Matter and Materials Physics* **89** (2014).

51 Wang, S. & Mingo, N. Improved Thermoelectric Properties of $Mg_2Si_xGe_ySn_{1-x-y}$ Nanoparticle-In-Alloy Materials. *Appl Phys Lett* **94** (2009).

52 Akasaka, M. *et al.* The thermoelectric properties of bulk crystalline n-and p-type Mg2Si prepared by the vertical Bridgman method. *Journal of Applied Physics* **104**, 013703 (2008).

53 Martin, J. Thermal conductivity of Mg 2 Si, Mg 2 Ge and Mg 2 Sn. *Journal of Physics and Chemistry of Solids* **33**, 1139-1148 (1972).

54 Schneider, C. A., Rasband, W. S. & Eliceiri, K. W. NIH Image to ImageJ: 25 years of image analysis. *Nat Methods* **9**, 671-675, doi:Doi 10.1038/Nmeth.2089 (2012).

55 Luo, W. *et al.* Fabrication and Thermoelectric Properties of $Mg_2Si_{1-x}Sn_x$ ($0 <= x <= 1.0$) Solid Solutions by Solid State Reaction and Spark Plasma Sintering. *Mater Sci Eng B-Adv* **157**, 96-100, doi:DOI 10.1016/j.mseb.2008.12.029 (2009).

56 Liu, W. *et al.* Advanced Thermoelectrics Governed by a Single Parabolic Band: $Mg_2Si_{0.3}Sn_{0.7}$, a Canonical Example. *Physical Chemistry Chemical Physics* **16**, 6893-6897, doi:Doi 10.1039/C4cp00641k (2014).

57 Pearson, G. L. & Bardeen, J. Electrical Properties of Pure Silicon and Silicon Alloys Containing Boron and Phosphorus. *Physical Review* **75**, 865-883, doi:Doi 10.1103/Physrev.75.865 (1949).

58 Minnich, A. J. *et al.* Modeling Study of Thermoelectric SiGe Nanocomposites. *Phys Rev B* **80**, 155327 (2009).

59 Li, W., Lindsay, L., Broido, D. A., Stewart, D. A. & Mingo, N. Thermal Conductivity of Bulk And Nanowire $Mg_2Si_xSn_{1-x}$ Alloys from First Principles. *Phys Rev B* **86**, doi:ARTN 174307 10.1103/PhysRevB.86.174307 (2012).

60 Bahk, J.-H. & Shakouri, A. Enhancing the Thermoelectric Figure of Merit Through the Reduction of Bipolar Thermal Conductivity with Heterostructure Barriers. *Appl. Phys. Lett.* **105**, 052106, doi:doi:http://dx.doi.org/10.1063/1.4892653 (2014).

61 Bahk, J. H., Bian, Z. X. & Shakouri, A. Electron Energy Filtering by a Nonplanar Potential to Enhance the Thermoelectric Power Factor in Bulk Materials. *Phys Rev B* **87**, doi:ARTN 075204 10.1103/PhysRevB.87.075204 (2013).

62 Yang, H. R. *et al.* Enhanced Thermoelectric Properties in Bulk Nanowire Heterostructure-Based Nanocomposites Through Minority Carrier Blocking. *Nano Letters* **15**, 1349-1355, doi:10.1021/nl504624r (2015).

63 Yuan, T. C. & Virkar, A. V. Kinetics of Spinodal Decomposition in the TiO2-SnO2 System: The Effect of Aliovalent Dopants. *Journal of the American Ceramic Society* **71**, 12-21 (1988).

64 Livak, R. & Thomas, G. Loss of coherency in spinodally decomposed Cu Ni Fe alloys. *Acta Metallurgica* **22**, 589-599 (1974).

65 Bux, S. K. *et al.* Mechanochemical synthesis and thermoelectric properties of high quality magnesium silicide. *J Mater Chem* **21**, 12259-12266 (2011).

66 Liu, W. *et al.* n-type thermoelectric material Mg2Sn0. 75Ge0. 25 for high power generation. *Proceedings of the National Academy of Sciences* **112**, 3269-3274 (2015).

67 Vivès, S. *et al.* Combinatorial approach based on interdiffusion experiments for the design of thermoelectrics: Application to the Mg2 (Si, Sn) alloys. *Chem Mater* **26**, 4334-4337 (2014).

68 Liu, W. *et al.* Convergence of conduction bands as a means of enhancing thermoelectric performance of n-type Mg 2 Si 1− x Sn x solid solutions. *Physical review letters* **108**, 166601 (2012).

69 Zhao, L.-D., Chang, C., Tan, G. & Kanatzidis, M. G. SnSe: a remarkable new thermoelectric material. *Energy & Environmental Science* **9**, 3044-3060 (2016).

70 Zhao, L.-D. *et al.* Ultralow thermal conductivity and high thermoelectric figure of merit in SnSe crystals. *Nature* **508**, 373 (2014).

71 Kim, S. I. *et al.* Dense dislocation arrays embedded in grain boundaries for high-performance bulk thermoelectrics. *Science* **348**, 109-114 (2015).

72 Liu, H. *et al.* Copper ion liquid-like thermoelectrics. *Nature materials* **11**, 422 (2012).

73 Heremans, J. P. *et al.* Enhancement of thermoelectric efficiency in PbTe by distortion of the electronic density of states. *Science* **321**, 554-557 (2008).

74 Boukai, A. I. *et al.* Silicon nanowires as efficient thermoelectric materials. *nature* **451**, 168 (2008).

75 Bubnova, O. *et al.* Optimization of the thermoelectric figure of merit in the conducting polymer poly (3, 4-ethylenedioxythiophene). *Nature materials* **10**, 429 (2011).

76 Kim, H. S., Liu, W. & Ren, Z. The bridge between the materials and devices of thermoelectric power generators. *Energy & Environmental Science* **10**, 69-85 (2017).

77 Kim, H. S., Wang, T., Liu, W. & Ren, Z. Engineering Thermal Conductivity for Balancing Between Reliability and Performance of Bulk Thermoelectric Generators. *Adv Funct Mater* **26**, 3678-3686 (2016).

78 Liu, W., Jie, Q., Kim, H. S. & Ren, Z. Current progress and future challenges in thermoelectric power generation: From materials to devices. *Acta Materialia* **87**, 357-376 (2015).

79 Yu, C., Murali, A., Choi, K. & Ryu, Y. Air-stable fabric thermoelectric modules made of N-and P-type carbon nanotubes. *Energy & Environmental Science* **5**, 9481-9486 (2012).

80 Hsu, J.-H., Choi, W., Yang, G. & Yu, C. Origin of unusual thermoelectric transport behaviors in carbon nanotube filled polymer composites after solvent/acid treatments. *Organic Electronics* **45**, 182-189 (2017).

81 Yazawa, K. & Shakouri, A. Cost-efficiency trade-off and the design of thermoelectric power generators. *Environmental science & technology* **45**, 7548-7553 (2011).

82 Toberer, E. S., Zevalkink, A., Crisosto, N. & Snyder, G. J. The Zintl Compound Ca5Al2Sb6 for Low-Cost Thermoelectric Power Generation. *Adv Funct Mater* **20**, 4375-4380 (2010).

83 Liu, W., Tang, X. & Sharp, J. Low-temperature solid state reaction synthesis and thermoelectric properties of high-performance and low-cost Sb-doped Mg2Si0. 6Sn0. 4. *Journal of Physics D: Applied Physics* **43**, 085406 (2010).

84 Han, X. & Shao, G. Interplay between Ag and interstitial Mg on the p-type characteristics of Ag-doped Mg 2 Si: challenges for high hole conductivity. *Journal of Materials Chemistry C* **3**, 530-537 (2015).

85 Akasaka, M. *et al.* Non-wetting crystal growth of Mg 2 Si by vertical Bridgman method and thermoelectric characteristics. *Journal of Crystal Growth* **304**, 196-201 (2007).

86 Tani, J.-i. & Kido, H. First-principles and experimental studies of impurity doping into Mg 2 Si. *Intermetallics* **16**, 418-423 (2008).

87 Tani, J.-i. & Kido, H. Lattice dynamics of Mg 2 Si and Mg 2 Ge compounds from first-principles calculations. *Computational Materials Science* **42**, 531-536 (2008).

88 Tani, J.-i. & Kido, H. Thermoelectric properties of Sb-doped Mg 2 Si semiconductors. *Intermetallics* **15**, 1202-1207 (2007).

89 Tani, J.-i. & Kido, H. Thermoelectric properties of Bi-doped Mg 2 Si semiconductors. *Physica B: Condensed Matter* **364**, 218-224 (2005).

90 Satyala, N. & Vashaee, D. The effect of crystallite size on thermoelectric properties of bulk nanostructured magnesium silicide (Mg2Si) compounds. *Applied Physics Letters* **100**, 073107 (2012).

91 Satyala, N. & Vashaee, D. Modeling of thermoelectric properties of magnesium silicide (Mg 2 Si). *Journal of electronic materials* **41**, 1785-1791 (2012).

92 Yin, L. *et al.* The influence of phonon scatterings on the thermal conductivity of SiGe nanowires. *Applied Physics Letters* **101**, 043114 (2012).

93 Liu, W. *et al.* New insight into the material parameter B to understand the enhanced thermoelectric performance of Mg 2 Sn 1− x− y Ge x Sb y. *Energy & Environmental Science* **9**, 530-539 (2016).

94 Yin, K. *et al.* Optimization of the Electronic Band Structure and the Lattice Thermal Conductivity of Solid Solutions According to Simple Calculations: A

Canonical Example of the Mg2Si1–x–y Ge x Sn y Ternary Solid Solution. *Chem Mater* **28**, 5538-5548 (2016).

95 William D. Callister, D. G. R. *Materials science and engineering: an introduction*. 9th edn, (Wiley, 2013).

96 Liu, X. *et al.* Low electron scattering potentials in high performance Mg2Si0. 45Sn0. 55 based thermoelectric solid solutions with band convergence. *Advanced Energy Materials* **3**, 1238-1244 (2013).

97 Kim, S., Wiendlocha, B., Jin, H., Tobola, J. & Heremans, J. P. Electronic structure and thermoelectric properties of p-type Ag-doped Mg2Sn and Mg2Sn1-xSix (x= 0.05, 0.1). *Journal of Applied Physics* **116**, 153706 (2014).

98 Chen, H., Savvides, N., Dasgupta, T., Stiewe, C. & Mueller, E. Electronic and thermal transport properties of Mg2Sn crystals containing finely dispersed eutectic structures. *physica status solidi (a)* **207**, 2523-2531 (2010).

99 Tani, J.-i. & Kido, H. Impurity doping into Mg 2 Sn: a first-principles study. *Physica B: Condensed Matter* **407**, 3493-3498 (2012).

100 Joshi, G. *et al.* Enhanced thermoelectric figure-of-merit in nanostructured p-type silicon germanium bulk alloys. *Nano letters* **8**, 4670-4674 (2008).

101 Wang, X. *et al.* Enhanced thermoelectric figure of merit in nanostructured n-type silicon germanium bulk alloy. *Applied Physics Letters* **93**, 193121 (2008).

102 Ma, Y. *et al.* Enhanced thermoelectric figure-of-merit in p-type nanostructured bismuth antimony tellurium alloys made from elemental chunks. *Nano Letters* **8**, 2580-2584 (2008).

103 Yang, J. *et al.* Solubility study of Yb in n-type skutterudites Yb x Co 4 Sb 12 and their enhanced thermoelectric properties. *Physical Review B* **80**, 115329 (2009).

104 Riffel, M. & Schilz, J. in *Thermoelectrics, 1997. Proceedings ICT'97. XVI International Conference on.* 283-286 (IEEE).